

Elucidating the Physical Origins of the Animal Magnetic Sense by Cavity-enhanced Spectroscopy

Matthew Golesworthy

New College
University of Oxford

A thesis submitted in partial fulfilment of the requirements for the degree of Doctor of Philosophy

Department of Chemistry
Interdisciplinary Biosciences Doctoral Training Partnership
1 October 2021

"What're quantum mechanics?"
"I don't know. People who repair quantums, I suppose."

Terry Pratchett, *Eric*

Abstract

Many animal species have the ability to navigate using the Earth's magnetic field. This is particularly true of migratory birds, who are able to fly thousands of kilometres only to nest in exactly the same place year on year. The best current hypothesis as to the method by which this magnetoreception – the ability to sense magnetic fields – takes place is that of magnetically sensitive radical pairs in cryptochromes – blue light photoreceptors found in the retinae of birds and other animals. Chapter 1 explores the theory needed for understanding the phenomenon of magnetoreception, especially spin chemistry.

The study of magnetically sensitive processes requires the ability to detect tiny changes in the concentrations of the chemical species involved. This has driven the development of state-of-the-art and high-sensitivity techniques, with a particular focus on optical spectroscopy. One such method is the use of cavity-based absorption measurements which increase the optical path length by passing the probe light through the sample multiple times. In this work, a spectrometer that employs the use of an optical cavity – cavity ring-down spectroscopy (CRDS) – was entirely redesigned, rebuilt and recoded. The work to improve the spectrometer, along with an introduction to the optical technique, is described in Chapter 2.

In Chapter 3, the performance of the spectrometer is scrutinised using a model system – flavin mononucleotide (FMN) and hen egg-white lysozyme (HEWL) – allowing for exploration of the detection sensitivity and stability of the apparatus. Time-resolved and magnetically altered reaction yield (MARY) experiments yield results similar to those reported previously, particularly by Dr D. Sheppard. The sensitivity of the rebuilt spectrometer is highlighted, revealing the importance of storage conditions of this widely used "calibration sample" with a slight deviation in the time- and wavelength-resolved spectra obtained when compared to previously reported results. Once shown that the spectrometer is fully functional, the effect of pump laser power on ring-down time is also explored with the hope of improving the signal-to-noise ratio by compensating for fluctuations from the laser.

The core of the thesis describes the measurements performed on cryptochrome 4 from three avian species: the migratory European robin (*Erithacus rubecula*); the pigeon (*Columba livia*), which is non-migratory, but known to orient using magnetic cues; and the chicken (*Gallus gallus*), which is not known to use the geomagnetic field for any purpose. The cryptochromes from the three species share strongly conserved amino acid sequences, but should, to support the cryptochrome hypothesis of magnetoreception, show differences that are based on the function. A marked difference in the spectroscopic results is shown between the migratory robin and the other two species. Additional measurements are performed on a point-mutant of the three cryptochromes in which the final electron transfer partner – a tryptophan residue at position 369 – is replaced so that it cannot be involved in forming the radical pair. It is

shown that, while all cryptochrome proteins show some sensitivity of their radical concentrations to applied magnetic fields, that of the migratory robin is most remarkable – both in its magnitude and lifetime. The results of this thesis, presented in Chapter 4, hence provide further support of the radical pair hypothesis of magnetoreception and the data and conclusion formed a substantial part of a *Nature* publication in 2021.

Acknowledgements

Firstly, an enormous thank you to my two supervisors, **Chris** and **Stuart**. Thank you for supporting me through both my Part II, as well as my four years as a DPhil student, especially as the times got tough. Thank you too, Chris, for allowing me to interview with you at New College and for affording me the opportunity to take on teaching. Thank you also to the third member of the MacTimmel clan, **Fraser**, for the enjoyable chats about hockey and being a source of conversation in the group so often.

Talking of the group, thank you to team CRT for being such a wonderful environment and having me as part of the team. Thank you to **Victoire** for your support and friendship, even when we had to put up with crazy Russian accommodation! Thank you too to **Kevin** for his good humour and for his guidance throughout my time in the group. Thank you to **Gabriel** for the many wonderful teaching conversations and fun chats about everything under the sun (usually with a pint in hand...). Thank you to **Jamie** for his support and for being such an excellent desk neighbour (even if your stuff fell over the dividing line...). Thank you to **Marcin** for always being so willing to explain concepts, especially with coding, and the many other conversations. Thank you also to the many others over the years with whom many special memories were made:

- **Steve** and **Rebecca** for the constant support through the DPhil from afar – I will never forget the wonderful times and many coffee walks we had during our Part II! It's been a great pleasure visiting you in London!
- **Dan** and **Charles** (and, of course, **Mimi**) for the late-night antics when thesis submission was approaching rapidly, and for the continued friendship throughout the DPhil;
- **Jess**, **Beds**, and **Jonny** for the fun in the lab (and outside of it);
- **Ruby** for making me think even harder about the CRDS;
- **Andrew** for the many brilliant chats and for challenging me on a number of things;
- **Tommy** for the walks and chats about teaching (and for putting up with my lack of understanding of football); and
- **Ana** for the many teas – and Gs & T – and support through the last bits of the project.

Thank you to the **Clarendon Fund** for supporting me financially through the doctorate and the **Interdisciplinary Bioscience DTP** for showing and teaching me many new things.

A massive thank you also to my wonderful housemates, especially the *QuaranTeam* – **Niels**, **Clare**, and **Alex** – for being the best company while locked down, for showing me how to erg, for the copious baking, and for teaching me so much.

Thank you also to the best next-door neighbour one could ask for, **Jon** – our over-the-fence coffees were thoroughly enjoyable and it's been a pleasure getting to know you better.

Thank you to my **students at Trinity, St Peter's, and Somerville** over the past years – it's been a pleasure teaching you; thank you for challenging me to think ever harder about the content and for furthering my enjoyment of teaching. It's lovely to see so many of you doing so well and I look forward to the wonderful stories in years to come!

Thanks also to my tutors – **Susan**, **Jon**, **Geoff**, **Russ**, **Mike**, and **Mark**. Without your support – both academic and pastoral – there is no way I would be where I am now and it's such a pleasure now getting the opportunity to work alongside many of you.

Thank you to my chemistry college mates, both at Trinity and St Peter's: **Liam**, **Phil**, **Jack**, and **Marty** for your continued friendship and excellent humour – I'm so looking forward to reunions in the future and seeing your numerous successes!

Thank you to my two colleges over my time at Oxford – **Trinity** and **New College** have been wonderful places to learn and in which to meet such incredible people.

Thank you to **Keble College** and **Matthew Martin** for affording me the opportunity to sing such amazing music and learn so much musically in one of the most incredible spaces. To the amazing friends I've made, thank you for your support and for being such a large part of my musical journey. In particular: **Rory**, **Liz**, **Nat**, **Robert**, **Lucy**, **Larissa**, **Beth**, **Ben**, **Nevsky**, and **Darren**. Thanks also to the wider Keble community, especially the **porters**, for making me feel so incredibly welcome!

Thank you also to **OUHC** for making me feel so welcome at your events and on the field – even if there was the occasional disagreement...

Thank you to my old school, **Bishops**, for your continued support and interest in me. Thank you also for igniting the spark in me to go and explore life to the fullest. Thank you especially to **Mark** and the Music Department – **Sheila**, **Gloria**, **Joc**, **Andrea**, and **Stephen** – for your enduring support and guidance, and to **Marcus** for igniting the passion for maths and science. Thank you also to **Nicky** for your guidance while over in the UK and for your constant interest in my life.

Thank you to my many friends back home for being so supportive, even while so far away, and for keeping in touch when I go silent. Thank you especially to: **Pete**, **Steve**, **Dusty**, **Jason**,

Nick, **Rob** and **Anthea**, **John** and **Emily**, and many of my "**newboys**". It really is always a pleasure to hear how you are and catch up over a coffee!

Thank you to all my friends here in the UK and for your continued support and friendship. In particular I'd like to thank:

- **Ed** for your support and friendship, especially when the chips are down, and for the incredible times in London or Oxford (or even South Africa) – always a pleasure seeing you!
- **Connor** for the many enjoyable dinners and drinks in Oxford, along with your amazing friendship;
- **Dan** and **Alice** for the virtual coffee breaks and real-life coffee-walks;
- **Bruno** and **Thomas** for the support through the lock-down and the many wonderful walks around Kingston and Wimbledon;
- **James** for your out-of-the-box thinking and challenging me when needed;
- **Toby** for the wonderful times in London;
- **Karl** for being an amazing housemate and for the many wonderful times around Oxford;
- **Tom** for the many walks, pizza evenings, science chats and support through the tough times;
- **Jack** for the many musical and academic chats, and friendship;
- **Rory** for the many walks, especially during lock-down, and fun during choir;
- **Matt** and **Iona** for your support and good humour, especially the virtual chats (especially with the *Cracking the Cryptic* sessions); and
- **Tom** for your friendship, support (especially while writing up), advice, the "weirdo walks", fun and various chats.

And last, but certainly not least, to my family for your continued and unending support. Thank you for your constant love and guidance. Thank you for absolutely everything – there is no way I would be here without you.

Contents

1 Introduction **1**

1.1 Background and Motivation 1

1.2 Spin Chemistry 2

1.2.1 The Zeeman Effect 4

1.2.2 The Two-spin System 5

1.2.2.1 The Exchange Interaction 7

1.2.2.2 The Dipolar Interaction 8

1.2.2.3 The Hyperfine Interaction 9

1.2.3 Spin Relaxation 10

1.3 The Radical Pair Mechanism 10

1.4 Magnetic Field Effects 11

1.4.1 Anisotropic Magnetic Field Effects 14

1.5 Magnetoreception and Biology 15

1.5.1 The Magnetite Hypothesis 15

1.5.2 The Cryptochrome Hypothesis 16

1.6 Current Work 18

2 Introduction to Cavity Ring-down Spectroscopy **20**

2.1 Optical Spectroscopy 20

2.1.1 Optical Cavities 21

2.2 Cavity Ring-down Spectroscopy 23

2.2.1 Principle of Cavity Ring-down Spectroscopy 23

2.2.1.1 Analysing the Results 26

2.2.1.2 Magnetic Field Effects – The Spectroscopic Definition 28

2.3 Experimental Techniques 28

2.4 Apparatus 30

2.4.1 The Cavity Ring-down Spectrometer 30

2.4.2 The Code 32

2.4.2.1 The Graphical User Interface 32

2.4.2.2 Introduction to Pseudocode 37

2.4.2.3 Initialisation 37

2.4.2.4 Pre-experiment Front Panel Control 39

2.4.2.5 Starting an Experiment 41

2.4.2.6 Running the Experiments 42

2.5 Role of CRDS in Understanding Biological Phenomena 49

3 Testing the Improved Cavity Ring-down Spectrometer with a Model System 51

3.1 Introduction 51

3.2 Results 54

3.2.1 Time-resolved Measurement of FMN/HEWL 54

3.2.2 MARY Measurement of FMN/HEWL 55

3.2.3 Time- and Wavelength-resolved Measurement of FMN/HEWL 56

3.2.4 The Importance of Sample Freshness 57

3.3 Power-dependence of **ΔA** 60

3.4 Conclusions 62

4 CRDS Measurements on Cryptochromes **63**

4.1 Background 63

4.2 Cryptochrome Synthesis and Preparation 67

4.2.1 Cryptochrome Expression and Purification 67

4.2.2 Sample Preparation 68

4.3 Comparing the Avian Wild Type Cryptochromes 69

4.4 Comparing the Avian W369F Cryptochrome Mutants 78

4.4.1 Summary 88

4.5 Time-dependent B-half 92

4.5.1 Exploring the Time-evolution of the $B_{1/2}$ Value 97

4.6 Further Considerations 102

4.7 Conclusion 106

5 Conclusions and Outlook **107**

5.1 Conclusions 107

5.2 Future Work and Outlook 109

Bibliography **110**

Chapter 1

Introduction

1.1 Background and Motivation

The ability of many animals, in particular birds, to migrate over great distances has fascinated people for centuries. The true story of such migration was not particularly well understood until a stork was shot down in northern Germany with an additional appendage: an African spear in its neck – a so-called "Pfeilstorch", of which one example exists in the Zoological Collection of the University of Rostock [1]. Prior to this it was believed that the animals that disappeared over certain seasons would simply transform into a different species, most notably ascribed to Aristotle, who is falsely claimed to have stated that redstarts would transform (or "transmute") into European robins for the winter [2]. Since these humble beginnings, a great deal of research has taken place to understand better the mechanisms and facilities required to perform such migrations and the navigational tools used in these journeys [3–8].

In order to navigate, animals need both a map and a compass sense [6, 9]. The map sense has, in some cases, been shown to be inherited or could be developed during the first migratory season of an animal's life [7, 10–13]. The compass sensing can be achieved using a solar or stellar compass, or the ability to sense the Earth's magnetic field – "magnetoreception" [8, 14, 15]. This latter sense has two main hypotheses as to its underlying mechanism – a topic of hot debate. The first hypothesis is based on magnetic iron-based particles within the animal, while the second is light-dependent and based around blue-light photoreceptors in the retina called cryptochromes[1] [16–26]. The mechanism of magnetoreception in cryptochromes has at its origin the formation of a radical pair – two lone electrons separated by some distance – that can then be impacted by both the direction and magnitude of the applied magnetic field. Behavioural studies suggest that both of these hypothesised mechanisms may play a part in

[1] This thesis will focus on cryptochromes, although there is an introduction and brief discussion of the "magnetite hypothesis" in Section 1.5.1.

magnetoreception, although, as discussed later, there is growing evidence for the involvement of the radical pair mechanism in magnetoreception [27–36].

The fact that a photochemical process might be influenced by a magnetic field as small as that of the Earth's (approx. 50 μT) seems rather unfeasible, especially when comparing the magnetic energy,[2] $\mu_B B$, with the thermal energy, $k_B T$, for which the latter is some six orders of magnitude larger than the former (at room temperature). The effect could, however, be felt if the system was already in some sort of non-equilibrium state that could be affected by a slight perturbation towards a particular product [27].

While the effects of magnetic fields in various systems have been measured at fields comparable to that of the Earth's, only specifically designed and synthesised molecules have, to date, shown a directionally dependent (or anisotropic) effect as a result of application of weak magnetic fields [36, 37]. A carotenoid-porphyrin-fullerene (CPF) triad system studied by Kerpal *et al.* showed an anisotropic response at field strengths as low as that of the Earth's, but the system benefits from several properties that have been custom-designed into its molecular make-up, most notably: slow spin relaxation and radical pair kinetics; axiality of the hyperfine couplings (see Section 1.2.2.3) in the carotenoid; and no hyperfine interactions in the fullerene [37]. Proteins are, by their very nature, far more complicated in their composition and would not be expected to have these properties, especially not with the significant number of spin-active nuclei present. Despite this increased complexity, the effect of weak magnetic fields plays a role in navigation and a variety of processes. Better understanding of this natural phenomenon and its underlying mechanism will not only give us great insight into the navigational ability of many animals, but may also allow us to produce new molecules that can function as chemical compasses.

A short introduction to the key areas required for understanding of this field is presented below, concentrating on the underlying theory of spin chemistry.

1.2 Spin Chemistry

Spin was first proposed in 1925 by Dutch physicists Uhlenbeck and Goudsmit to facilitate the analysis of atomic spectra – an assumption that the electron possessed an intrinsic angular momentum of magnitude $\frac{1}{2}\hbar$ with two states: $m_s = +\frac{1}{2}$ (denoted $|\alpha\rangle$ or $|\uparrow\rangle$) and $m_s = -\frac{1}{2}$ (denoted $|\beta\rangle$ or $|\downarrow\rangle$) [38]. This was later used to explain the results of the famous Stern-Gerlach experiment,[3] where a beam of silver atoms was split into two distinct bands [39]. This

[2] See Section 1.2.1.

[3] The result was previously ascribed to space quantisation and the magnetic moment of an electron.

quantity called "spin" is a purely quantum mechanical phenomenon and has no classical analogue and was formalised in Dirac's development of relativistic quantum mechanics [40, 41].

Spin comes in two flavours: fermions (particles with half-integer spin) and bosons (particles with integer spin) [42–45]. This is important in the general form of the Pauli Principle: "*The total wavefunction must be antisymmetric under the interchange of any pair of identical fermions and symmetric under the interchange of any pair of identical bosons.*"

Spin follows the general angular momentum relations with the total and projection spin operators, respectively, defined by:

$$\hat{s}^2|\psi\rangle = \hbar^2 s(s+1)|\psi\rangle, \text{ and} \tag{1.1a}$$

$$\hat{s}_z|\psi\rangle = \hbar m_s|\psi\rangle, \tag{1.1b}$$

where s and m_s are the spin magnitude and the spin projection quantum numbers, respectively. The magnitude of the spin vector is given by:

$$|\mathbf{s}| = \hbar\sqrt{s(s+1)}, \tag{1.2}$$

and the spin projection number, m_s, can take on $2s+1$ values given by the Clebsch-Gordan series:

$$m_s = s, s-1, \cdots, -s+1, -s. \tag{1.3}$$

Analogous to the classical magnetic moment derived from an angular momentum of a charged particle, the spin of a charged entity also gives rise to a magnetic moment, μ_s, that depends on the magnitude of the spin:

$$\boldsymbol{\mu}_s = -\frac{g_e \mu_B \mathbf{s}}{\hbar}, \tag{1.4}$$

where $g_e \approx 2.00232$ is the g-factor for a free electron and μ_B is the Bohr magneton, often used as the "quantum" of magnetic moments:

$$\mu_B = -\gamma_e \hbar = \frac{e\hbar}{2m_e}. \tag{1.5}$$

Here γ_e is the gyromagnetic ratio of the electron, e is the charge of an electron, and m_e is the mass of an electron. Similar to the projection of spin onto the z-axis, the projection of the magnetic moment is quantised as:

$$\mu_z = -g_e \mu_B m_s. \tag{1.6}$$

The g-factor is, in fact, an anisotropic tensor that depends on the local environment, but this can, however, be considered as negligible for the cases discussed in this thesis as a result of the samples always being in the liquid phase. As such, an effective g-value of g_e is assumed because of the very minute changes (below sensitivity) in this value from spin-orbit coupling.

1.2.1 The Zeeman Effect

The quantum mechanical magnetic moment (like its classical analogue) can interact with an externally applied field. Much like the classical case,[4] the energy of interaction between the magnetic moment and the magnetic field, **B**, is given by the Hamiltonian:

$$\hat{H} = -\hat{\boldsymbol{\mu}} \cdot \mathbf{B} = \frac{g\mu_\mathrm{B}}{\hbar} \hat{\mathbf{s}} \cdot \mathbf{B}, \tag{1.7}$$

where $\hat{\boldsymbol{\mu}}$ is the quantum mechanical magnetic moment operator and $\hat{\mathbf{s}}$ is the spin angular momentum operator, both of which are vectors.

If there is sufficiently strong an external magnetic field, the system aligns with this field axis (conventionally labelled the z-axis) and the energy is, therefore, quantised along this axis. As such, the magnetic moment operator can be replaced by the z-component operator of the same:

$$\hat{H} = -\hat{\mu}_z B = +g_e \gamma_e \hat{s}_z B. \tag{1.8}$$

The quantised values of $\hat{s}_z$ are known, so one can write the energies of the system as:

$$E_{m_s} = +g_e \gamma_e m_s \hbar B = -g_e \mu_\mathrm{B} m_s B. \tag{1.9}$$

In the case of an electron, the energies of the $|\alpha\rangle$ and $|\beta\rangle$ states are, therefore, given by:

$$E_\alpha = +\frac{1}{2} g_e \mu_\mathrm{B} B, \text{ and} \tag{1.10a}$$

$$E_\beta = -\frac{1}{2} g_e \mu_\mathrm{B} B. \tag{1.10b}$$

It follows, then, that the energy difference between these two states is:

$$\Delta E_\mathrm{Z} = g_e \mu_\mathrm{B} B. \tag{1.11}$$

It is worth noting that the above formulation applies to a free electron in a vacuum under the influence of a magnetic field. In an atomic or molecular environment there are likely to be additional contributions arising from the spin-orbit coupling and the Zeeman interaction between the orbital magnetic moment and the external field. The expression can, therefore, be corrected by simply replacing the magnetic field, **B**, with an effective field, $\mathbf{B}_\mathrm{eff}$, that encompasses these additional components.

[4] In the classical case, the energy interaction is given by the dot product of the magnetic dipole moment, $\boldsymbol{\mu}$, and the field, **B**, *viz.* $E = -\boldsymbol{\mu} \cdot \mathbf{B}$.

1.2.2 The Two-spin System

In the above discussion there has only been a single spin in a vacuum interacting with an external magnetic field which is, understandably, not representative of the real world. Of particular relevance to this work is the combination of two spins forming a so-called "spin-correlated radical pair" (SCRP) [46, 47]. The meaning of the word "correlation" is just that there is a relative mutual orientation of the two spins; if the spins are randomly oriented with respect to one another, they are said to be "uncorrelated". A spin-correlated radical pair is formed when the radicals are created at the same time and in the same process, such as an electron transfer reaction where the orientation of the spin of the transferred electron is fixed.

Considering now a system of two spin-$\frac{1}{2}$ particles (e.g. electrons in a radical pair), the total spin of the system, $\mathbf{S}$, is simply the vector sum of the constituent spins, *viz.* $\mathbf{S} = \mathbf{s}_1 + \mathbf{s}_2$. From this, as before, one can obtain the overall spin quantum number, S, which follows the Clebsch-Gordan series:

$$S = s_1 + s_2, s_1 + s_2 - 1, \cdots, |s_1 - s_2|, \tag{1.12}$$

with projections along the quantisation axis given by:

$$M_S = +S, +S - 1, \cdots, -S + 1, -S. \tag{1.13}$$

Considering the two-spin-$\frac{1}{2}$ case, $S = 0, 1$ yielding three possible projections: $M_S = -1, 0, +1$. For the $S = 1$ case, there are three possible projections, while there is only a single projection for the $S = 0$ case, hence these are known as the "triplet" and "singlet" states, respectively.

These spin states can also be considered under the commonly used vector model, shown in Fig. 1.1, in which the spins precess about the quantisation axis (shown as the z-axis in the figure, but only applicable if the field is sufficiently strong), thus forming a cone of possible positions. The frequency of the spins' precession is given by the Larmor frequency:

$$\omega_{\mathrm{L}} = \frac{g\mu_{\mathrm{B}}B}{\hbar}, \tag{1.14}$$

where all symbols take their usual meaning. The Larmor frequency can also be converted to an energy (using $\Delta E = \hbar\omega$), which is the same energy required to match the Zeeman splitting.

The vector model also demonstrates the uncoupled basis, in which the spin and projection onto the quantisation axis of each entity is known (in this case, $m_{s,1}$ and $m_{s,2}$ and notated $|m_{s,1}, m_{s,2}\rangle$), but their relative phase is not. The two spins are indistinguishable and thus the two $M_S = 0$ states are thus made of linear combinations of the two possibilities (i.e. $|\alpha, \beta\rangle$ and $|\beta, \alpha\rangle$). The singlet state, $|S\rangle$, is antisymmetric with respect to interchange of the spins while the triplet state, $|T_0\rangle$, is symmetric in order to satisfy the Pauli Principle (the singlet state spatial wavefunction is symmetric and the triplet wavefunction is antisymmetric).

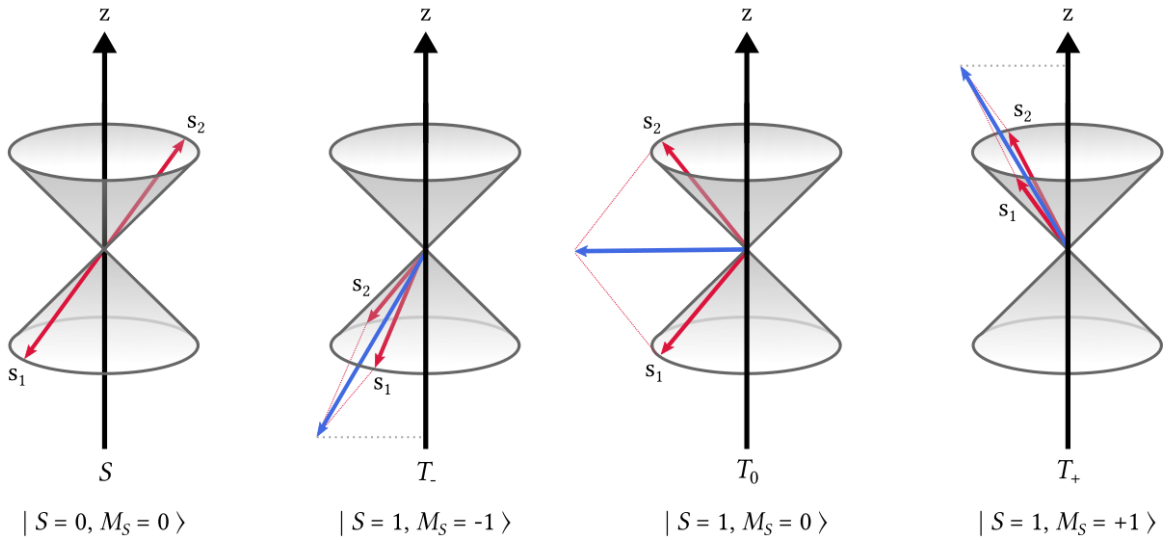


Figure 1.1: Cones showing the relative positions of the spin vectors (red) for each of the coupled spins, $\mathbf{s}_1$ and $\mathbf{s}_2$, in the two-spin vector model. The total spin vector in each case is shown in blue.

It is, however, often more useful to know about the relative phases of the two spins. This is called "the coupled basis" in which the total spin and its projection are known. The states in the coupled basis are often described by the overall spin multiplicity (S for singlet and T for triplet) or by the kets showing the spin and its projection ($|S, M_S\rangle$). These representations are shown in Table 1.1.

Uncoupled Basis	**Coupled Basis**	$\|S, M_S\rangle$
$\frac{1}{\sqrt{2}}(\|\alpha,\beta\rangle - \|\beta,\alpha\rangle)$	$\|S\rangle$	$\|0,0\rangle$
$\|\alpha,\alpha\rangle$	$\|T_+\rangle$	$\|1,+1\rangle$
$\frac{1}{\sqrt{2}}(\|\alpha,\beta\rangle + \|\beta,\alpha\rangle)$	$\|T_0\rangle$	$\|1,0\rangle$
$\|\beta,\beta\rangle$	$\|T_-\rangle$	$\|1,-1\rangle$

Table 1.1: The singlet (S) and triplet (T) states for a two spin-$\frac{1}{2}$ system in coupled and uncoupled bases. The spin quantum number and the spin projections are shown in the final column. The vector model representations of these states are shown in Fig. 1.1.

In the singlet (S) state, $\mathbf{s}_1$ and $\mathbf{s}_2$ are antiparallel, yielding an overall spin and projection of zero. In the T_0 state, $\mathbf{s}_1$ and $\mathbf{s}_2$ have equal and opposite projections onto the z-axis (or field axis) giving an overall projection of $M_S = 0$, while the T_+ and T_- states have $\mathbf{s}_1$ and $\mathbf{s}_2$ with identical z-axis projection, but different directions (to give the correct overall magnitude of $\sqrt{2}\hbar$, as given by Eqn 1.2, modified to use S rather than s).

While an oversimplification of the reality of spin, the vector model does provide an idea as to how how singlet-triplet (S-T) interconversion can occur. Considering first the S and T_0 states, in which the only difference is the relative phase of the two spins (a phase difference of π radians in the singlet case), one can see that any change to the precession rate of either spin would permit an interconversion between the two. Since the rate of precession is given by Eqn 1.14, the difference in their frequencies is given by:

$$\Delta\omega_{\mathrm{L}} = \frac{\Delta g \mu_{\mathrm{B}} B}{\hbar}, \tag{1.15}$$

and this alters their relative phase, allowing the transition from S to T_0 and vice versa. It is also evident that an increase in the magnetic field strength also increases this difference in frequencies, allowing singlet-triplet interconversion to take place on a timescale that competes with the rate of singlet or triplet product formation, thus making these processes magnetically dependent. This is called the "Δg mechanism" and can be considered negligible for the work described in this thesis due to the minute differences in g values and small magnetic field strengths used [48, 49].

Alternatively, processes that result not in a change of precession frequency, but rather a spin-flip ($m_s = +\frac{1}{2} \leftrightarrow m_s = -\frac{1}{2}$), convert from the S/T_0 manifold to that of T_+ and T_-. This is usually accompanied by a nuclear spin-flip in order to maintain the overall spin, but may also be induced by energetic activation through, for example, application of a radiofrequency field.

Much like the single-spin-$\frac{1}{2}$ case, the Zeeman energy is given by:

$$E_{M_S} = g\mu_{\mathrm{B}} M_S B, \tag{1.16}$$

where M_S is the overall magnetic quantum number. It is evident that the S and T_0 states, for which $M_S = 0$, are, therefore, not impacted energetically by an external magnetic field, in contrast to the T_+ and T_- states, which split energetically for a coupled pair (much like the spin-$\frac{1}{2}$ case, shown in Fig. 1.2 a); this is shown in Fig. 1.2 b). Note too that the S and T_0 states might not always be degenerate as a result of additional inter-spin interactions that will be discussed hereafter.

1.2.2.1 The Exchange Interaction

As a result of the exchange symmetry of the Pauli Exclusion Principle, the degeneracy of the singlet and triplet states is lifted by the exchange interaction, even in the absence of an external field.

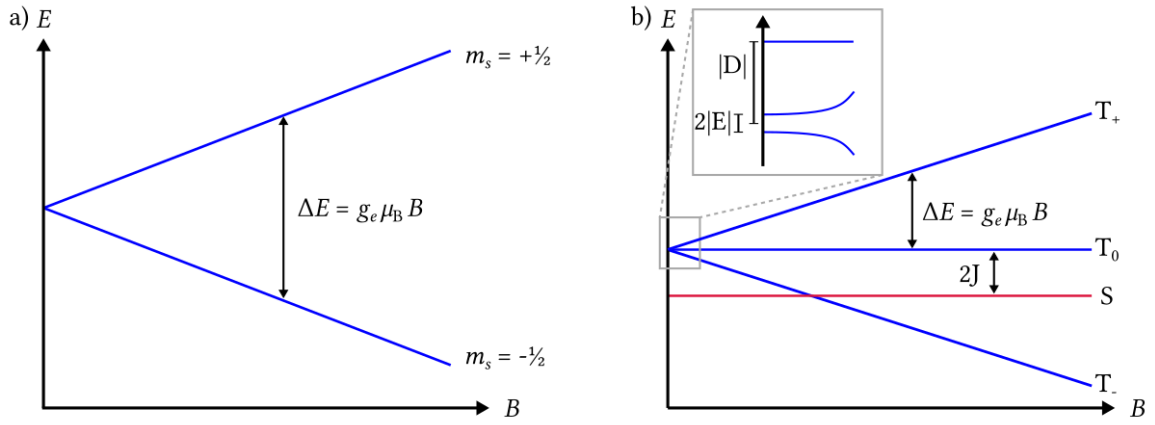


Figure 1.2: a) The splitting in energy of the two states of a spin-$\frac{1}{2}$ particle under the influence of a magnetic field. b) The energy of the four states in a coupled two-spin-$\frac{1}{2}$ system. The energy gap between the T_0 and S states is a result of the exchange interaction and can be inverted (i.e. J can be either positive or negative – here negative).

The Hamiltonian representing the exchange interaction may be written [50, 51]:

$$\hat{H} = -2J(r)\,\hat{\mathbf{s}}_1 \cdot \hat{\mathbf{s}}_2\,, \tag{1.17}$$

where $2J(r)$ is the exchange energy as a function of inter-radical separation, r, and $\hat{\mathbf{s}}_1$ and $\hat{\mathbf{s}}_2$ are the spin operators for electrons 1 and 2, respectively. This lifting of degeneracy can be seen in Fig. 1.2 b) for $J < 0$. It should be noted that J can be either positive or negative, placing either the singlet or triplet higher in energy, respectively.

The exchange energy decays exponentially with inter-radical distance and is, for all intents and purposes, negligible for distances beyond approximately 1 nm [52, 53]. For the work in this thesis, the radicals are separated beyond this 1 nm distance and, therefore, the exchange interaction is assumed negligible.

1.2.2.2 The Dipolar Interaction

In cases where there is more than one free electron, the overall spin is often one or greater, *viz.* $S \geq 1$, and it is found that the spin sub-levels are non-degenerate, even in the absence of a magnetic field. This is a result of the dipolar interaction, commonly referred to as the "zero-field splitting", where the magnetic dipoles associated with the electrons interact with one another. The energy of such an interaction is given by the Hamiltonian (in matrix mechanics):

$$\hat{H}_{\mathrm{ZFS}} = \hat{\mathbf{s}}_1^{\dagger} \cdot \mathbf{D} \cdot \hat{\mathbf{s}}_2\,, \tag{1.18}$$

where $\mathbf{D}$ is the traceless tensor describing the size and anisotropy of the interaction.

The dipolar interaction is inversely proportional to r^3 and is, therefore, expected to act over a much longer distance than the exchange interaction. Rapid molecular motion can result in the dipolar interaction averaging out which encompasses all cases in this thesis.

1.2.2.3 The Hyperfine Interaction

Some nuclei also possess a nuclear spin magnetic moment vector, **I**. Of particular relevance to biological systems are ^{1}H and ^{14}N, both of which have significant magnetic moments and make up the majority of the abundance of these elements (> 99 % in both cases). This magnetic moment is also subject to the quantum mechanical properties of other angular momenta, such as a magnitude of $\hbar\sqrt{I(I+1)}$ and the $2I+1$ sublevels, m_I, from the Clebsch-Gordan series. For non-zero values of m_I, there is a magnetic moment that generates a weak local field that can then influence electronic spins in the system. There are two means of interaction:

- The dipole-dipole interaction
  The magnetic dipolar moments of the nucleus and other spin interact as described in Section 1.2.2.2. Like the electronic dipolar interaction, this contribution averages out in solution and so is not relevant to those systems discussed in this thesis.

- The Fermi contact interaction
  This isotropic interaction depends on the electron spin density at the nucleus (or the amount of *s*-orbital character in the molecular orbital).[5] As it is isotropic, there is no cancellation in solution and it only depends on the relative orientations of the nuclear and electronic spin.

The effective magnetic field experienced by the electronic spin (as alluded to in Section 1.2.1) is given by:

$$B_{\text{eff}} = B + B_{\text{hf}} = B + m_I a, \tag{1.19}$$

where a is the hyperfine coupling constant. As discussed above, the presence of this additional field contributes to the Larmor frequency of each of the electrons. If this interaction is different for the two electrons, then they will precess at different frequencies, allowing for singlet-triplet interconversion (as described above). However, in contrast to the Δg mechanism, the difference in the precession frequencies as a result of the hyperfine mechanism is field independent.

[5] McConnell showed an approximate link between the *s*-character of *sp*-hybrid orbitals in aromatic molecules and the Fermi contact interaction between the carbon nuclei and electrons in the protons perpendicular to the π-system [54]. This is surprising given that spin density is expected to remain polarised entirely in the π-system, but is passed through the σ-bonding system with dampening of the original hyperfine interactions.

1.2.3 Spin Relaxation

Spin relaxation is the term used to describe incoherent spin-mixing mechanisms that return the system to the Boltzmann distribution of spin states in the system as a result of random fluctuations in local fields [42]. There are two main mechanisms by which spin relaxation occurs: spin-lattice and spin-spin relaxation.

Spin-lattice relaxation is a result of molecular motion and tumbling which occur at a wide range of frequencies. If these frequencies match the energy gap between any of the spin states (as a result of, for example, the Zeeman interaction), then this could induce a spin-flip and interconversion between states.

Spin-spin relaxation is more similar to the coherent mechanisms in that it alters the precession frequencies of the electronic spins, destroying their phase coherence and spin correlation. In contrast, though, this relaxation occurs due to low frequency oscillations in the local field, randomising the rate of singlet-triplet interconversion. Such fields can appear constant on the timescale of the lifetimes observed in the systems in this thesis and thus act as an additional contribution (along with the hyperfine interaction) to the effective magnetic field.

Challenges in the measurement of MFEs can be encountered for some of the systems in this thesis (such as cryptochromes), where the microsecond lifetimes of the radical pairs is of a similar order of magnitude to that of relaxation in organic radical systems (10^{-6}–10^{-4} s) [52].

1.3 The Radical Pair Mechanism

The radical pair mechanism is the most common reason for magnetosensitivity of radical-based reactions and was discovered independently by Closs and the duo Kaptein and Oosterhof in 1969 [46, 47, 49]. The mechanism typically occurs by the scheme shown in Fig. 1.3. The acceptor (A) is initially excited (here by photoexcitation, but alternative methods are also possible) to A^*. After this one of two fates is possible: there is either electron transfer from the donor (D) to form the correlated radical pair itself under conservation of spin angular momentum or, if intersystem crossing is faster than the electron transfer, there is conversion to the triplet followed by electron transfer. Thus the radical pair can be formed in either a singlet or a triplet state (it is said to be "singlet-" or "triplet-born", respectively); the former is usually true of intramolecular processes and the latter true for intermolecular processes. The radical pair, once formed, can then undergo singlet-triplet mixing. Due to spin conservation, the triplet radical pair cannot recombine directly back to the ground state, but it could, along with the singlet, form a secondary radical pair either by physical separation (e.g. diffusion

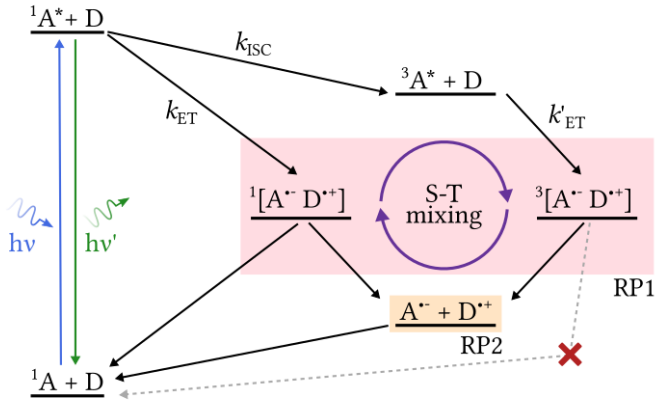


Figure 1.3: Photoscheme for the radical pair mechanism. Following photoexcitation of the acceptor (A ⟶ A*), the system will either undergo intersystem crossing (ISC) or electron transfer (ET) under conservation of spin angular momentum; if the former, then electron transfer occurs following ISC. The electron transfer leads to a spin-correlated radical pair (RP1, shown in pink) which is subject to coherent singlet-triplet (S-T) mixing. Both the singlet and triplet components of RP1 can undergo additional charge transfer or modification to yield a second radical pair (RP2, shown in orange), in which the two radicals have lost their correlation. The singlet component of RP1 can recombine to the ground state, but the triplet component cannot due to spin-conservation (represented by the red cross on the dashed grey line), while the components of RP2 independently return to the ground state. Further information is provided in the text.

out of the solvent cage) or by some other chemical process (e.g. (de)protonation). The formation of this secondary radical pair causes loss of its spin correlation, followed by return to the ground state (once it has returned to a singlet state). Alternately, the primary singlet radical pair (RP1) could react to return it to the ground state. There is one additional means of return to the ground state which is radiative emission before electron transfer can occur.

As stated above, the radicals must be separated by a short distance ($r \geq 1$ nm) to minimise the effects of the exchange and dipolar interactions and allow singlet-triplet mixing.

1.4 Magnetic Field Effects

The effects of magnetic fields on chemical processes were first discussed in the 1960s following experiments by Johnson looking at triplet exciton annihilation in anthracene crystals [55]. The theoretical underpinning of these results, work performed by Merrifield, was based on the use of a spin Hamiltonian [56]. The fact that animals might be able to use the Earth's magnetic field, which is three orders of magnitude smaller than the fields used by Merrifield (50 μT and 10 mT, respectively), is surprising as the magnetic energy, $\mu_B B$, is much smaller than thermal energy (at room temperature), $k_B T$, which is known to have effects on chemical reactions and processes.

Magnetic field effects (MFEs) measured by optical spectroscopy typically rely on determining the concentrations of the transient species or, indeed, that of the ground state. MFEs can be approximately described by three general regimes: the low field effect (LFE), the hyperfine-driven effect ("normal MFE"), and the Δg-dominated regime, which will be described below. Typically these occur in the sub-millitesla, millitesla, and tesla field strengths, respectively.[6] Consider here a singlet-born radical pair, as shown by the simplified photoscheme inset in Fig. 1.4, with a measurement of the concentrations of the radical species (shaded pink and orange) as a function of magnetic field. This can be summarised in a magnetically altered reaction yield (MARY) plot, a schematic version of which is presented in Fig. 1.4, which shows the radical concentrations at a magnetic field strength B ($[R_B]$) relative to that at zero field (*viz.* $[R]_B - [R]_{B=0}$).

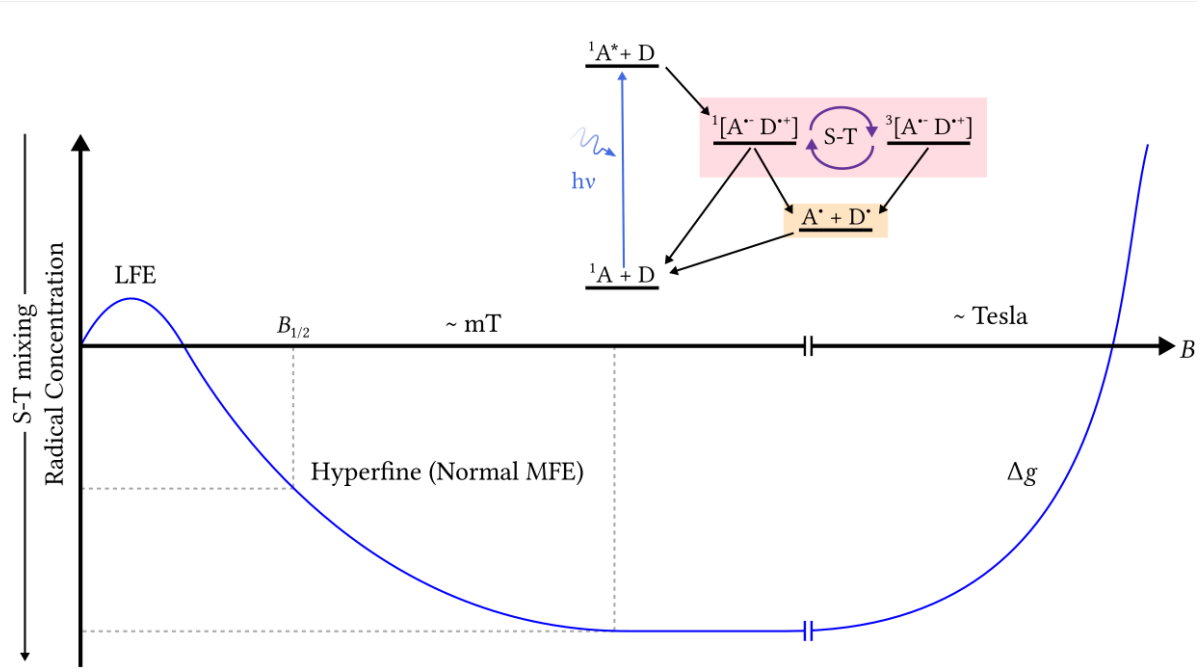


Figure 1.4: A schematic absorption-detected MARY curve showing the radical concentration relative to its zero-field value as a function of applied magnetic field (i.e. $[R]_B - [R]_{B=0}$) for a singlet-born radical pair; the radicals whose concentrations are being measured are highlighted in pink and orange in the photoscheme. The three main regions – low field (LFE), hyperfine (normal MFE) and Δg – are shown and are described in the text. The characteristic $B_{1/2}$, the value at which the MFE reaches half of its saturation value in the "normal MFE" region, is also indicated. A schematic singlet-born radical pair photoscheme is also included for reference.

[6] This applies particularly to the carbon-centred radical pair systems considered in this thesis. There are deviations, such as for the singlet fission–triplet-triplet annihilation process, that alter the driving factors affecting the shape of the magnetically altered reaction yield plots for these systems.

At low fields there is a relaxation of the spin selection rules, allowing increased interconversion between S and T_0, as a result of symmetry breaking introduced by the magnetic field [57]. This, in turn, generates a greater concentration of triplet state, which cannot directly recombine to the ground state as a result of the spin selection rules, resulting in an increase in the concentration of the radicals, $[\mathrm{R}]_B$ relative to the zero-field case ($[\mathrm{R}]_{B=0}$), and, therefore, an increase in the MARY curve (i.e. $[\mathrm{R}]_B > [\mathrm{R}]_{B=0}$). This is known as the low field effect (LFE).

Beyond this low-field region, as the field strength begins to exceed the hyperfine coupling experienced by the electrons forming the radical pair, the Zeeman interaction becomes more important and reduces the ability to mix into the T_+ and T_- states because of the energetic separation of the S/T_0 and T_+/T_- manifolds. This increases the singlet fraction with fewer radicals reaching the triplet state, from which the radicals cannot recombine, which reduces $[\mathrm{R}]_B$. The sign of $[\mathrm{R}]_B - [\mathrm{R}]_{B=0}$ changes, determined by the relative influences of both the low field effect and the Zeeman interaction, with the Zeeman interaction taking greater effect as the field increases [58]. There comes a point where only the interconversion from S to T_0 is possible due to the large energetic separation between the S/T_0 and T_+/T_- manifolds, leading to a saturation of the radical concentration as this interconversion reaches an equilibrium.

At particularly large fields, the difference in g-value between the two radicals – which are usually very small in carbon-centred radicals – makes more of an effect (see Eqn 1.15), allowing for greater interconversion between the S and T_0 states. This is known as the Δg mechanism and, once again, starts to change the sign of $[\mathrm{R}]_B - [\mathrm{R}]_{B=0}$ due to an increasing concentration of the radical species [48, 49].

The width of the MARY plot is characteristic of MFEs and is measured using the $B_{1/2}$ parameter, which is the value at which the MFE reaches half of its saturation value (within the "normal MFE" regime). This parameter is obtained by fitting the experimentally obtained MARY plot to a Lorentzian curve and determining the half-width at half-maximum. In the idealised case where only the hyperfine mechanism is involved, the value of $B_{1/2}$ can be predicted using the Weller equation [59]:

$$B_{1/2} = \frac{\sqrt{3}\left(\langle a_\mathrm{A}\rangle^2 + \langle a_\mathrm{D}\rangle^2\right)}{\langle a_\mathrm{A}\rangle + \langle a_\mathrm{D}\rangle}, \tag{1.20}$$

where A and D are the "acceptor" and "donor" radical components in the radical pair, respectively, and $\langle a_X \rangle$ is the effective hyperfine coupling for each radical X:

$$\langle a_X \rangle = \sqrt{\frac{4}{3}\sum_i a_{iX}^2 I_X \left(I_X + 1\right)}, \tag{1.21}$$

where the sum is over all magnetically active nuclei, I_X is the nuclear spin quantum number, and a_{iX} is the hyperfine coupling constant for the interaction between nucleus i and

radical component X. As a point of reference for this work, the relevant value for the flavin-tryptophan species considered in this work is $B_{1/2} \approx 3\,\mathrm{mT}$ [59, 60].

The $B_{1/2}$ value predicted by Eqn 1.20 is purely hyperfine-driven and, therefore, discounts additional processes, particularly spin relaxation, that are known to broaden the MARY curve and thus increase the $B_{1/2}$ value [61].

1.4.1 Anisotropic Magnetic Field Effects

In the study of magnetic field effects, especially in understanding their use in the compass sense, the directional dependence is important. Just as a compass points towards the magnetic pole, being able to alter a magnetically sensitive material's orientation with respect to the magnetic field may show such directional dependence – a so-called "anisotropic magnetic field effect".

The work performed by Johnson in the 1960s showed that there was an anisotropic magnetic response in the photoluminescence from triplet-triplet annihilation in anthracene crystals in relation to the crystal structure [62]; this has also been reproduced on several other polyacenes and their derivatives [63, 64]. These experiments on the organic semiconductors were, however, performed at fields orders of magnitude stronger than that of the Earth's.

Work performed by Kerpal *et al.* has, however, shown it all the more feasible that such magnetic anisotropy can be achieved at fields close to that of the geomagnetic field, demonstrating this on a molecular triad system at 100 μT – approximately twice that of the geomagnetic field strength [37].

Due to the challenges of performing such measurements on biological systems, there are, as yet, no measurements of magnetic anisotropy on systems believed to be involved in magnetoreception – the ability for animals to sense the Earth's (or other) magnetic fields – despite the wealth of literature describing such biological effects from behavioural measurements [3, 6, 11, 17, 30, 32, 65–67].

One successful approach, employed by Déjean *et al.*, that has shown both MFEs on cryptochromes and anisotropic MFEs on other crystalline systems is confocal microscopy [68]. In their work, Déjean *et al.* show MFEs on plant cryptochrome 1 from *Arabidopsis thaliana* (thale cress) and flavin mononucleotide/hen egg-white lysozyme (FMN/HEWL) in solution, along with anisotropic measurements on both FMN/HEWL and tetracene crystals. This suggests that, with the potential to grow cryptochrome crystals, anisotropic MFEs may be seen on biological samples in the near future.

1.5 Magnetoreception and Biology

The long-distance migratory behaviour of some avian species was only verified in the 1820s following a hunter in northern Germany shooting down a stork with an African spear through its neck [1]. The means by which these species were able to navigate over such distances was, however, a mystery. Behavioural studies suggest that there are most likely several mechanisms at play in birds (and other migratory species) including: celestial compasses, geographic cues, olfactory cues, local sound cues, and magnetoreception [9]. This latter-most mechanism has, however, been a highly debated issue since its reporting by Wiltschko and Wiltschko in 1972 [69]. There are currently two main hypotheses as to how avian species sense the Earth's magnetic field: iron-based deposits in the beak (the "magnetite hypothesis"), and cryptochromes.

1.5.1 The Magnetite Hypothesis

The magnetite hypothesis is based on the suggested presence of crystalline magnetite (Fe_3O_4), which can exist in single domains with permanent magnetic moments. These magnetic moments are of sufficient a magnitude to be influenced by a 50 μT field (of similar strength to that of the geomagnetic field) [19, 70–73]. Smaller single-domain particles (approx. 20 nm) are superparamagnetic and could induce magnetic fields because of the external field environment. With these particles, the movement induced by application of an external field could be used to trigger a biological cascade that would then inform the nervous system of the magnetic environment.

While possibly far-fetched, evidence for such an hypothesis can be seen in the ability of magnetotactic bacteria, which contain chains of magnetic crystals (or magnetosomes) to orient with a magnetic field [65, 74, 75]. Despite this ability, however, it has been suggested that, in this example, this alignment is simply a case of passive alignment [3, 76].

Some iron-mineral structures (consisting of magnetite, maghemite (Fe_2O_3), and a vesicle) have been proposed as the magnetoreceptor in the upper beaks of birds [22, 77]. These structures were believed to be at nerve endings, but this was later disputed in two studies that showed that they are "almost certainly" macrophages [78, 79].

There is also an ever-increasing wealth of evidence that suggests that the ophthalmic branch of the trigeminal nerve is involved in magnetoreception [80–82]. In particular, surgical severance of the nerve showed a significant effect on the magnetoreception ability of the birds concerned and reduced the neural responses in the part of the brain responsible for processing the signals from the trigeminal nerve. So too, there is a clear deflection of the orientation of the birds following strong magnetic pulses which would realign the magnetic moments of the magnetic

particles [66, 83]. Overall, the trigeminal nerve is neither sufficient nor necessary for magnetic-compass orientation, meaning that it unlikely carries all of the required magnetic information to the brain.

Another controversial study showing human magnetoreception attributes the "strong, specific and repeatable effects on human brainwave activity" to a "ferromagnetic transduction element" and claims to dispute the quantum (cryptochrome) hypothesis [84]. It cites the sensitivity to only movement of the magnetic field as a clear marker that such an effect could not be quantum mechanically derived (such as in the cryptochrome hypothesis), as well as the differences in neuronal activity as a result of the declination of the field in the experimental procedure. The study, however, is only performed on humans and can, therefore, not be immediately extended to other species – especially those with known migrations.

1.5.2 The Cryptochrome Hypothesis

The other main hypothesis in avian magnetoreception is based on the use of cryptochromes – 60 kDa blue-light photoreceptor proteins located in the retinae of birds [85].[7] Cryptochromes are usually grouped with photolyases (both cyclobutane pyrimidine dimers and pyrimidine-pyrimidone (6–4) adducts) as a family with similar structure, but a wide range of functions including: DNA repair, circadian entrainment, and regulation of transcriptional activity [86, 87]. This family of proteins also has a flavin cofactor (flavin adenine dinucleotide, FAD), which is vitamin-derived and is also able to absorb at the blue end of the visible spectrum [86].[8] The so-called "photolyase homology region" is fairly similar across all photolyases and cryptochromes, with the main difference (other than functionally) being in the C-terminal tail, which is extended in cryptochromes. This extension is of variable length and is somewhat consistent between the same phylogenetic types of cryptochrome (e.g. type I cryptochromes), but otherwise not conserved, especially between plant and animal cryptochromes [85, 90]. These extensions in the C-terminal tail are unstructured when expressed alone, but show significant structure when expressed with the photolyase homology region [91–93].

Cryptochromes are typically classed into four main groups: animal types I and II cryptochromes (based on their light responsivity), plant cryptochromes, and CRY-DASH (*Drosophila, Arabidopsis, Synechocystis, Homo*) photoreceptors [35, 87, 94]. CRY-DASH photoreceptors are more like photolyases in their structural and photophysical properties, as well as role in DNA repair (although only for single-stranded DNA) [87]. Interestingly, *Drosophila* and *Homo* do

[7] Cryptochromes are also found in other species, including plants (e.g. cryptochrome 1 from *Arabidopsis thaliana*). Cryptochromes may, therefore, be found in locations other than the retina for some species.

[8] There is also an assumed second cofactor – either 8-hydroxy-5-deazariboflavin or 5,10-methenyltetrahyrdofolate – which is not believed to be involved in the photochemical processes described in this thesis [88, 89].

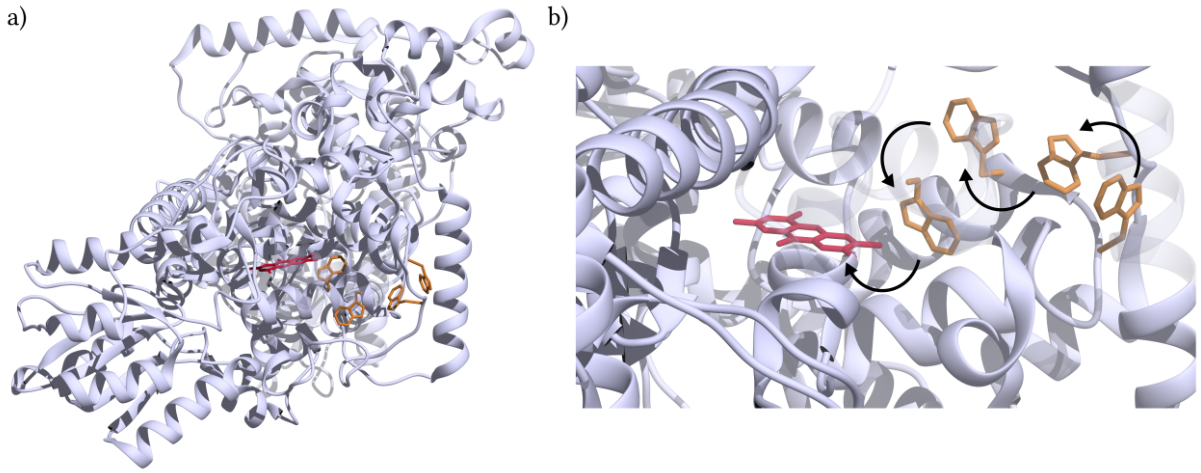


Figure 1.5: a) Secondary structure of cryptochrome from *Drosophila melanogaster* (*Dm*Cry, PDB: 4GU5) showing the flavin isoalloxazine moiety (red) and the conserved tryptophan tetrad (orange) [98]. b) The active site for the proposed radical pair formation, enlarged and rotated from a). In cryptochromes the flavin acts as the acceptor, after which there is a rapid electron transfer cascade along the tryptophans (shown by the arrows) to yield a singlet-born radical pair between the flavin and terminal tryptophan.

not, in fact, possess CRY-DASH, but were included in this grouping due to phylogenetic analyses which suggested that they classed more closely to animal cryptochromes; more recently they have been shown to stem from a cyclobutane pyrimidine dimer photolyase [95–97].

Adding further evidence for the cryptochrome hypothesis is the seasonal expression patterns in migratory and non-migratory species, in particular that of the domestic chicken (*Gallus gallus*) and the European robin (*Erithacus rubecula*). Günther *et al.* showed that cryptochrome 4 from the European robin (*Er*Cry4 WT [9]) had a nearly 2.5 times increase in expression during the migratory season compared to the non-migratory season and *Er*Cry2 WT showed an approximately 1.5 times increase, in contrast with all bar one of the cryptochromes from domestic chickens (*Gg*Crys 1a, 2, and 4, but not 1b); in the case of *Gg*Cry1b, there was only a significant difference between the non- and migratory seasons in postnatal day 1 chickens, but it is a decrease and "could be a statistical outlier" [99]. In the same work, Günter *et al.* also show that the circadian oscillations of expression of *Er*Cry4 are small, especially in comparison to *Er*Cry 1a and b, making it suitable for use as a magnetoreceptor, irrespective of timing of migration [99]. Staining methods also show that *Er*Cry4 is located in the outer segments of double cones in the retina, meaning that it is able to undergo photolysis from natural light to form the magnetosensitive species.

The photochemical process by which magnetosensitivity is hypothesised to occur centres around the radical pair mechanism (see Section 1.3). Photoexcitation of the cryptochrome's

[9] "WT", short for "wild type", indicates that no mutations have been made to the natural sequence during expression.

non-covalently bound FAD cofactor in its fully oxidised redox state (^{1}F) produces the excited singlet state (^{1}F*), which is then rapidly reduced on a picosecond timescale to give a flavosemiquinone radical ($F^{\bullet-}$) [100]. This is mediated by cascade electron transfer along a conserved chain of tryptophan (Trp, W) residues[10] (Fig. 1.5 b), generating the $^1[F^{\bullet-}\ TrpH^{\bullet+}]$ radical pair (RP), the $TrpH^{\bullet+}$ radical cation being derived from the oxidation of the terminal Trp residue and consequent protonation of the same by a nearby residue [35, 101, 103–107]. The RP consequently undergoes coherent singlet-triplet interconversion driven by the hyperfine interaction between the electron and nuclear spins. The cryptochrome hypothesis relies on this singlet-triplet interconversion efficiency being affected by the applied magnetic fields and, as a result of the different fates of the singlet and triplet RPs, the yields and kinetics of the photophysical process being field-sensitive [27, 108].

There is significant debate about the downstream signalling mechanism of cryptochrome's magnetosensitivity. The hypothesis that currently has the greatest traction is that of a conformational change at the C-terminal tail of the cryptochrome [109, 110]. Such light-induced conformational changes at the C-terminal tail have been assumed to play a role in signalling [111–113]. Vaidya *et al.* propose two possible mechanisms for these changes in cryptochrome from *Drosophila melanogaster*, *Dm*Cry, both of which could be possible in avian cryptochromes [114]. Both mechanisms rely on photoexcitation of the cryptochrome, but differ in the starting oxidation state of the flavin: the first model starts from the fully oxidised state, whereas the second assumes the presence of the radical anion ($F^{\bullet-}$). The excited state then triggers the conformational change, leading to a signal transduction.

1.6 Current Work

This work aims to further the understanding of the physical origins of the animal magnetic sense, focussing on the cryptochrome hypothesis in avian species.

Chapter 2 looks at optical spectroscopy and the application of optical cavities for high-sensitivity measurements. The principle of cavity ring-down spectroscopy (CRDS) and its analysis procedures are introduced, along with the possible measurement techniques. The rebuilt and recoded spectrometer used in this work is introduced with discussion around the recoding of the spectrometer in LabVIEW. The role of CRDS within the wider research area and the suite of techniques used alongside it are also explored.

[10] It should be noted that in some species, such as *Arabidopsis thaliana* cryptochrome 1 and *E. coli* photolyase, there is a tryptophan *triad* rather than the tetrad shown in the figure [101, 102]. It was believed for some time that the same was true of *Dm*Cry until reported by Nohr *et al.* [35].

Having rebuilt and recoded the spectrometer, it is critical to ensure that it is working correctly using a well-studied model system – in this case, flavin mononucleotide (FMN) and hen egg-white lysozyme (HEWL). These assessments are shown in Chapter 3. The results from these experiments are compared with the literature and the importance of sample freshness – particularly that of proteins – is discussed. With the rebuild of the spectrometer, it is also possible to measure the pump laser-pulse energy. Experiments are performed to assess whether measurement of this energy provides a means of improving the signal-to-noise ratio.

Having assessed the accuracy of the rebuilt spectrometer, spectroscopic measurements are preformed on the samples of interest – cryptochrome 4 from three avian species: *Erithacus rubecula* (European robin, *Er*Cry4); *Gallus gallus* (chicken, *Gg*Cry4); and *Columba livia* (common pigeon, *Cl*Cry4). The effect of a point mutation in one of the residues involved in the electron transfer process that forms the radical pair is also explored with a hypothesis as to the time dependence of the $B_{1/2}$ value discussed. These results are shown in Chapter 4.

Chapter 2

Introduction to Cavity Ring-down Spectroscopy

2.1 Optical Spectroscopy

The interaction of light with matter has played a critical role in our understanding of the universe. The combination of Lambert's law ("The loss of light intensity when it propagates in a medium is directly proportional to intensity and path length", *Photometria* in 1760), which was taken from an essay by Pierre Brouguer in which he noticed this phenomenon in wine, and Beer's law ("The transmittance of a solution remains constant if the product of the concentration and path length stays constant") has enabled scientists to characterise and explore many phenomena [115–117].

The relationship between the incident (I_{in}) and outgoing (I_{out}) light intensities is given by the Beer-Lambert law:

$$I_{\text{out}} = I_{\text{in}} 10^{-\epsilon(\lambda)cl}, \tag{2.1}$$

where $\epsilon(\lambda)$ is the wavelength-dependent molar absorption coefficient, c is the concentration of the absorbing species, and l is the path length of sample through which the light travels. The wavelength-dependent absorbance, $A(\lambda)$, is more commonly used and is defined as:

$$A(\lambda) = -\log_{10} \frac{I_{\text{out}}}{I_{\text{in}}} = \epsilon(\lambda)cl. \tag{2.2}$$

It is worth noting that while the decadic (base-10) definition is favoured in many analytical communities (especially in the gas-phase community), there is some preference for the

definition based around the natural logarithm:

$$A'(\lambda) = -\ln \frac{I_{\text{out}}}{I_{\text{in}}} = \alpha(\lambda) l, \tag{2.3}$$

where α is the transmission coefficient of the sample and l is the path length, as above.

There is a simple conversion between the two:

$$A(\lambda) = \epsilon(\lambda) c l = \frac{\alpha(\lambda) l}{\ln 10}. \tag{2.4}$$

It is, therefore, possible to determine the concentration of a sample of known path length and attenuation coefficient (either $\alpha(\lambda)$ or $\epsilon(\lambda)$) from a determination of the transmission losses.

While of great use, there are sensitivity issues that arise as a result of the Beer-Lambert law. If $\alpha(\lambda)\, l$ is small as a result of a small molar attenuation coefficient or when sample quantities are restrictive, resulting in a shorter path length, the minimum detectable change in the absorbance is given by:

$$A_{\text{min}} \ln 10 = \alpha_{\text{min}} = \frac{\Delta I_{\text{min}}}{I_{\text{in}}}. \tag{2.5}$$

For measurable changes, this minimum change in light intensity, ΔI_{min}, must be distinguishable over the often large and noisy background. It is currently challenging to determine absolute intensity changes to better than 1 in 1000, meaning that $A_{\text{min}} = \frac{1\times10^{-3}}{\ln 10} \approx 4 \times 10^{-4}$.

2.1.1 Optical Cavities

A natural extension to single-pass experiments is the use of mirrors to pass the light through the sample more than once, effectively increasing the path length. This, in turn, increases the change in intensity, making it easier to distinguish from the background. Early uses of these optical cavities, including the White and Herriott cells, had a non-zero incidence angle and, in order to get the required sensitivity, needed both large mirrors and sample volumes [118–120]. However, the adjustment of this to zero incidence angle, which required coupling of the light through the back of one of the mirrors and removed the need for an aperture into the optical cavity, meant that the sample volume could be reduced substantially.

Light in a stable cavity will reflect multiple times between the two mirrors and, therefore, interfere with itself. It should be unsurprising, therefore, that some interference patterns are sustained while others are not through constructive and destructive interference, respectively. The patterns that are sustained are known as “cavity modes” (or “modes” for short) [121].

Mode structures take the form of a Hermite polynomial multiplied by a Gaussian function, known as “Hermite-Gaussian modes”, which are an approximate solution to the wave

equation. Written in the form TEM_{nm},[1] $m, n \geq 0$ indicate the number of nodes in the y and x directions, respectively, (the z-axis defines the direction along which the light travels). Modes with $m, n = 0$ are called "axial" (or "fundamental") modes, while all others are known as "higher-order" modes. Of particular importance for the work in this thesis is the TEM_{00} mode, into which a laser pulse can most efficiently couple as a result of its Gaussian beam shape. This mode is also the least divergent and is, therefore, most able to be focussed into a small spot within the cavity.

A cavity is said to be "unstable" if the beam would grow until it is no longer fully contained and would miss the mirror on a return trip. The condition for stability is given by [122]:

$$0 \leq g_1 g_2 \equiv \left(1 - \frac{d}{r_1}\right)\left(1 - \frac{d}{r_2}\right) \leq 1, \tag{2.6}$$

where g_i is the so-called "stability" parameter, r_i is radius of curvature for mirror i, and d is the cavity length. The values of stable g and some mirror configurations are shown in Fig. 2.1. The location of the stability parameters for the cavity ring-down spectrometer used in this work is also shown in the diagram with a green star.

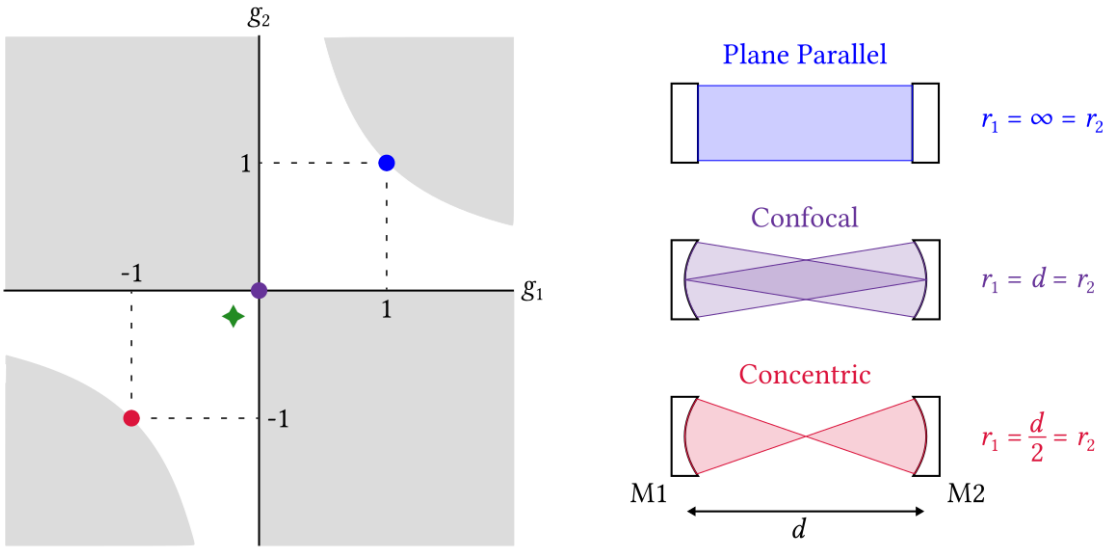


Figure 2.1: Plot showing the stable (unshaded) regions for optical cavities in terms of the stability factor, g_i (defined in the text), for each of the two mirrors (M1, M2). The shaded regions indicate unstable cavities where there is net loss due to uncontrolled beam spread. Three special cases of marginal stability are also shown, along with their beam profiles and the conditions on the radii of curvature, r_i, based (where appropriate) on the cavity length, d. The stability of cavity used in this work is indicated by the green star ($r_1, r_2 = 0.5\,\text{m}$ and $d = 0.6\,\text{m} \Longrightarrow g_1, g_2 = -0.2$).

[1] TEM stands for "transverse electromagnetic".

2.2 Cavity Ring-down Spectroscopy

2.2.1 Principle of Cavity Ring-down Spectroscopy

The principle of cavity ring-down spectroscopy (CRDS) is shown in Fig. 2.2 and will be explained in detail here.

Light of intensity I_{in} is injected into the optical cavity through the back of the first mirror (M1). The light in the cavity decays as a result of various processes: the interaction with the sample, scattering, and loss through the two mirrors. The small fraction of the intensity that escapes the cavity through the second mirror (M2) can be recorded as a function of time.

If the laser pulse-width is shorter than the duration of a round trip in the cavity, the detected intensities are a train of pulses with this exponentially decaying intensity. If the mirrors have reflectivity R, the light intensity after the first pass of the cavity, I_0, is given by:

$$I_0 = I_{\text{in}} \times (1-R) \times \mathrm{e}^{-\alpha l} \times (1-R) = I_{\text{in}}(1-R)^2 \mathrm{e}^{-\alpha l} = I_{\text{in}} T^2 \mathrm{e}^{-\alpha l}, \tag{2.7}$$

where $T = 1 - R$ is the transmissibility of the mirrors, and the other symbols have their usual meanings.[2] It can be seen that the intensity has been attenuated first by the transmissibility of M1, then by the Beer-Lambert interaction with the sample and further by the transmissibility of M2 (Fig. 2.2 a).

The light that remains within the cavity has its intensity, $I_{\text{in}} T \mathrm{e}^{-\alpha l}$, attenuated by R upon its reflection in M2, before passing through the sample again (Fig. 2.2 b). The same is true upon its return (albeit with M1, Fig. 2.2 c). The light upon this second round trip (and subsequently) is therefore attenuated in total by a factor of $R^2 \mathrm{e}^{-2\alpha l}$ before passing through M2 (an attenuation of T) to the detector. Thus, the intensity of the second pulse to the detector is given by:

$$I_1 = I_{\text{in}} T \mathrm{e}^{-\alpha l} \times R \times \mathrm{e}^{-\alpha l} \times R \times \mathrm{e}^{-\alpha l} \times T = \left(I_{\text{in}} T^2 \mathrm{e}^{-\alpha l}\right) \left(R \mathrm{e}^{-\alpha l}\right)^2 = I_0 \left(R \mathrm{e}^{-\alpha l}\right)^2; \tag{2.8}$$

in other words, the intensities of subsequent pulses reaching the detector are attenuated by a factor of $\left(R \mathrm{e}^{-\alpha l}\right)^2$. Hence, the intensity of the nth pulse is given by:

$$I_n = I_0 \left(R \mathrm{e}^{-\alpha l}\right)^{2n} = I_0 \exp\left(2n(\ln R - \alpha l)\right). \tag{2.9}$$

[2] The wavelength component of the attenuation coefficient is omitted for clarity.

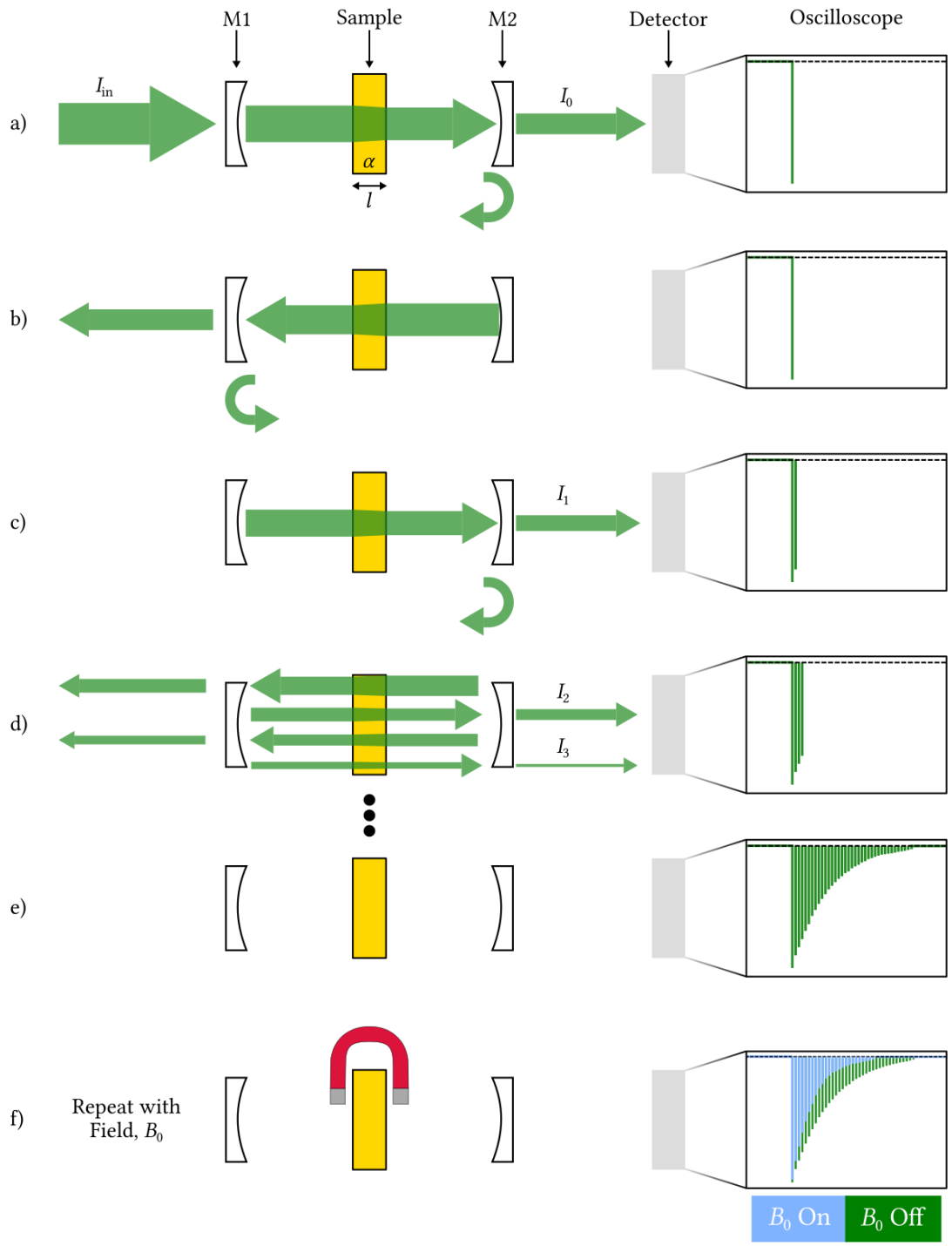


Figure 2.2: Figure showing the principle of CRDS. a) Light is injected into the cavity through the first cavity mirror (M1) after which it passes through the sample of interest. Some of the light is reflected off the second cavity mirror (M2), while a fraction is able to be detected. The transmission coefficient, α, and path length, l, are shown. b) The reflected light once again passes through the sample and M1, while a fraction remains within the cavity. c) The light that remains within the cavity once again passes through the sample and M2 to the detector, leading to a second signal on the oscilloscope. d) & e) The above continues until the light intensity is zero and the full ring-down trace is evident. f) For measurement of magnetic field effects, the experiment can be repeated with a magnetic field (B_0) present and the effect compared (here we assume that B leads to an increase in absorber concentration). A decrease in the width of the arrow indicates a lesser intensity. The technique and the analysis behind it are explained in greater detail in Section 2.2.1.

Due to the shortness of the cavity and resolution of the detectors used, the individual pulses are unresolvable, rather adopting a continuous trace in time, where the discrete n can be converted to a continuous time variable, t, given by:

$$t = n\frac{2d}{c}, \tag{2.10}$$

where d is the mirror separation and c is the speed of light. Rearranging for n and substituting into Eqn 2.9, one obtains a time-dependent intensity exiting the cavity:

$$I(t) = I_0 \exp\left(\frac{ct}{d}(\ln R - \alpha l)\right). \tag{2.11}$$

Due to the high reflectivity of the mirrors ($R > 0.997\ldots$), it is valid to assume that $\ln R \approx -(1-R)$ and one can, therefore, write:

$$I(t) = I_0 \exp\left(-\frac{ct}{d}(1 - R + \alpha l)\right) = I_0 \exp\left(-\frac{t}{\tau}\right), \tag{2.12}$$

where:

$$\tau = \frac{d}{c(1 - R + \alpha l)}, \tag{2.13}$$

is the characteristic "ring-down time" of the exponential (the time taken for the intensity to reach $\frac{1}{e}$ its initial value).

Considering the case of a cavity in the absence of an absorber, i.e. $\alpha = 0$, the ring-down time is simply:

$$\tau_0 = \frac{d}{c(1-R)}. \tag{2.14}$$

Using Eqns 2.13 and 2.14 allows manipulation to obtain the absorbance, A, of the sample (see Eqn 2.4):

$$A \ln 10 = \alpha l = \frac{d}{c}\left(\frac{1}{\tau} - \frac{1}{\tau_0}\right) = \frac{d}{c}\frac{\Delta\tau}{\tau\tau_0}, \tag{2.15}$$

where $\Delta\tau = \tau_0 - \tau$.

In all the work in this thesis, it is not possible to calculate the absolute absorbance due to the continual presence of the sample and sample cell in the spectrometer. Instead, the change in absorbance as a result of photoexcitation, ΔA, is used throughout and follows Eqn 2.15 closely:

$$\Delta A = A_{h\nu} - A = \frac{d}{c \ln 10}\left[\left(\frac{1}{\tau_{h\nu}} - \frac{1}{\tau_0}\right) - \left(\frac{1}{\tau} - \frac{1}{\tau_0}\right)\right] = \frac{d}{c \ln 10}\left(\frac{1}{\tau_{h\nu}} - \frac{1}{\tau}\right), \tag{2.16}$$

where the subscript $h\nu$ indicates photoexcitation and the other symbols have their usual meanings.

2.2.1.1 Analysing the Results

Traces obtained in the running of CRDS are in the form of an exponential decay, as seen above in Fig. 2.2 and in Fig. 2.3. The traces are initially grouped by whether or not a magnetic field was applied and then by either pump-probe delay (PPD) time for time-resolved measurements or field strength for magnetically altered reaction yield (MARY) experiments (experiment types are discussed below in Section 2.3); for the multivariable experiments, the traces are grouped by both variables, as well as the presence or absence of the magnetic field. Following this grouping, all traces are fit to a mono-exponential and the characteristic ring-down time recorded.

At this point the user is able to select and remove traces from the analysis based on the ring-down times. It is not unusual to see fluctuation (approx. 5 %) in ring-down time for a single variable group over the course of an experiment due to fluctuations in alignment of the cavity, but it is only traces that have a ring-down time substantially below the trend (15 %) that should be removed.[3] The drop in ring-down time is usually due to the presence of an additional scatterer (such as dust passing through the cavity) which lowers the intensity observed and, thus, shortens the ring-down time.

Using Eqn 2.16, the ring-down times are converted to ΔA values and the field "off" values are subtracted from their respective field "on" values to obtain the effect of the magnetic field (*viz.* $\Delta\Delta A = \Delta A_B - \Delta A_{B=0}$). These can be plotted to best see the time-/field-evolution of the magnetic field effect.

This analysis procedure is shown schematically in Fig. 2.3 for a time-resolved experiment.

Post-analysis data fitting was performed in OriginPro 2020. Parameters in analysis of the time-resolved measurements were allowed to vary freely. The centre of the Lorentzian, used to fit the MARY traces, was fixed at 0 mT, but all other parameters in both fitting routines were allowed to vary freely.

[3] In some cases, there are ring-down times substantially larger than usual. These are usually a result of a poor automated fit, which can be assessed by the user before considering whether to remove that data-point as an outlier.

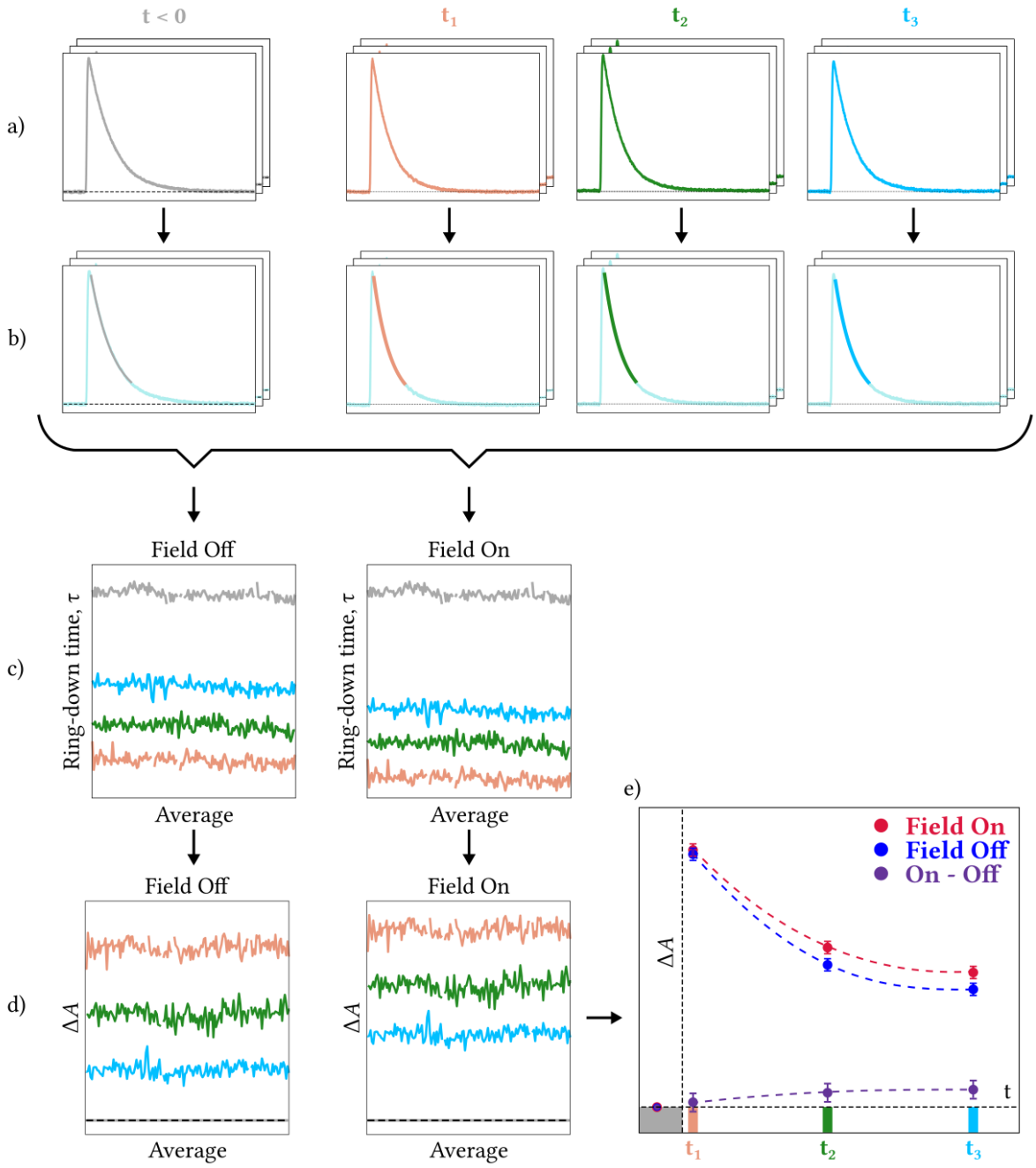


Figure 2.3: Schematic showing the analysis procedure used for CRDS – here for a time-resolved experiment. In MARY-based experiments, the (positive) pump-probe delay (PPD) times are replaced by field strengths. a) The traces at different PPDs are acquired and grouped by PPD. b) The exponential traces from a) (shown in light blue) are fit to mono-exponential decays over the range of 95–5 % of the maximum intensity. c) The ring-down times (exponential decay constant, see text) over the course of the experiment. At this point, trace outliers are removed from the analysis (can be seen by gaps in the traces). d) The ring-down times are converted to ΔA values, using the negative PPDs as the reference ring-down times. e) The ΔA values are averaged and plotted as a function of time with error bars, usually showing the standard error of the mean unless otherwise stated. Further information on the analysis process is provided in the text.

2.2.1.2 Magnetic Field Effects – The Spectroscopic Definition

As discussed in Section 1.4, the magnetic field effect is measured based on concentrations of the transient species. More formally, however, the percentage magnetic field effect, %MFE, measured by absorption is given as:

$$\%\text{MFE} = \frac{\Delta A_B - \Delta A_{B=0}}{\Delta A_{B=0}} \times 100 = \frac{\Delta\Delta A}{\Delta A_{B=0}} \times 100, \tag{2.17}$$

where ΔA_B is the change in absorbance at the wavelength measured in the presence of a magnetic field of strength B.

For completeness, similar is true for emission-based techniques, where %MFE is defined as:

$$\%\text{MFE} = \frac{I_B - I_{B=0}}{I_{B=0}} \times 100 = \frac{\Delta I}{I_{B=0}} \times 100, \tag{2.18}$$

with I_B the emission intensity at a magnetic field strength B.

2.3 Experimental Techniques

There are two main experimental techniques on the CRDS: time-resolved and MARY; the other techniques discussed herein are based on one of these two. All of the techniques are schematically shown in Fig. 2.4.

A single average of the time-resolved experiment involves measuring ring-down traces for "field on" and "field off" couplets at specified pump-probe delay times; the field strength for the "on" traces is constant throughout the experiment. Several of these specified pump-probe delay times are negative, which provides the pre-photoexcitation reference traces, as discussed above. Once traces have been taken at all pump-probe delay times of interest, the process can then be repeated to achieve a better signal-to-noise ratio. This is shown schematically in Fig. 2.4 a).

A single average of a MARY experiment involves recording an initial (non-photoexcited) reference trace, before keeping the pump-probe delay constant (and positive) and altering the magnetic field strength; zero-field measurements are also included in the list of field strengths. After all of the field strengths are recorded, another reference trace is taken and, once again, the cycle can be repeated to achieve a better signal-to-noise ratio. This is shown schematically in Fig. 2.4 b).

The additional three experimental types presented in this thesis are variations of the above two experiments, albeit with averaging over an additional variable.

The first is a time- and wavelength-resolved experiment, where a single average of the time-resolved technique is run before changing wavelength (Fig. 2.4 c). Once all the wavelengths of interest have been recorded, the experiment can be repeated to improve the signal-to-noise ratio.

The second is the time-resolved MARY experiment, where a single MARY average is performed before changing the pump-probe delay time (Fig. 2.4 d). Once again, the procedure can be repeated for improved signal-to-noise following measurements at all pump-probe delay times of interest.

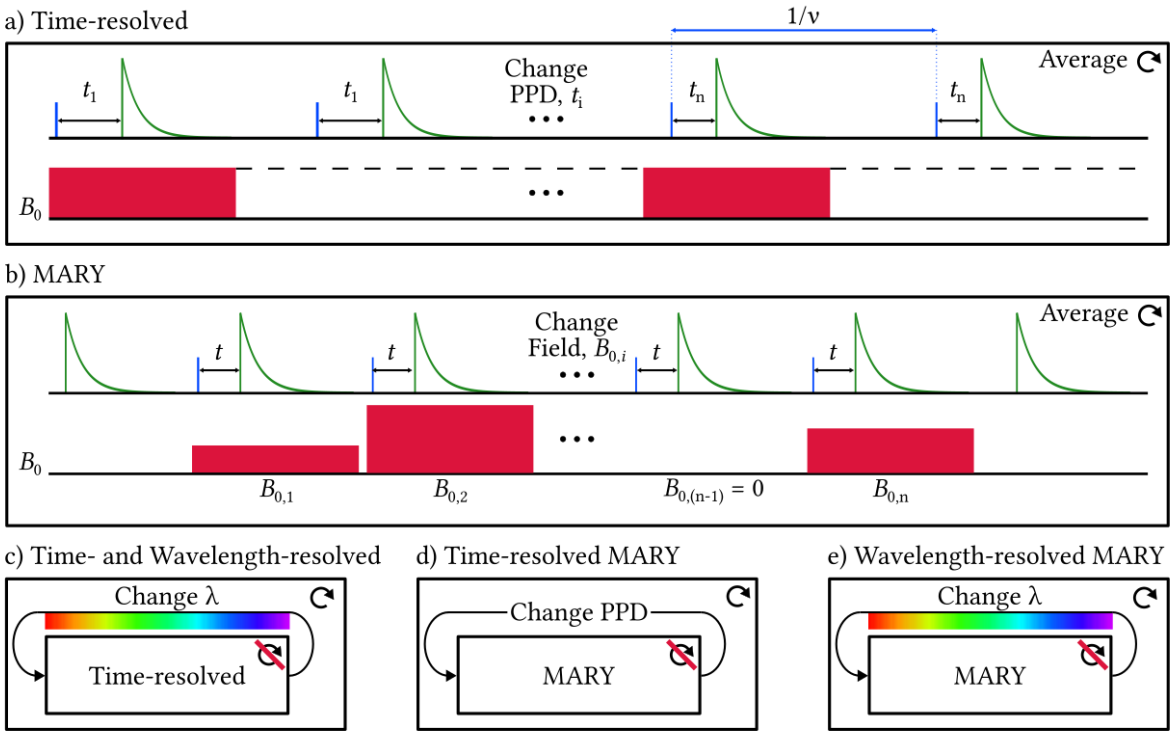


Figure 2.4: Schematic showing the routines for the various CRDS experiment types. The frequency of the experiment is shown above the top panel. a) The time-resolved experiment has pairs of field "on" and "off" couplets with changing pump-probe delay (PPD) time, t_i; at least one of the couplets has $t_i < 0$ to act as a reference trace. The field strength is constant for all the field "on" steps. After all of the couplets have been run, the PPD times are randomised again before acquiring the next average. b) The MARY experiment starts with a non-photoexcited reference trace, before fixing the PPD, t, and altering the field strength, $B_{0,i}$. Once measurements at all the field strengths have been acquired, a second reference trace is taken. After this, the field strengths are randomised again before acquiring the next average. c) The time- and wavelength-resolved experiment performs a single average of the time-resolved experiment at a particular wavelength before scanning through the wavelengths, randomising the PPD times for each. After all of the wavelengths of interest, the experiment can be averaged. d) The time-resolved MARY experiment performs a single MARY average, randomising the field strengths at each PPD, before changing the PPD. After all the PPD times of interest, the experiment can be averaged. e) The wavelength-resolved MARY experiment performs a single MARY average, randomising the field strengths at each wavelength, before changing the wavelength. After all of the wavelengths of interest, the experiment can be averaged.

The final technique is the wavelength-resolved MARY in which a single MARY average is performed before altering the wavelength (Fig. 2.4 e). This technique was introduced for completeness and has not been run in this work.

2.4 Apparatus

The spectrometer used in this work was entirely rebuilt and recoded. This section will look at both the physical apparatus and the operating code.

2.4.1 The Cavity Ring-down Spectrometer

A schematic of the CRDS apparatus is shown in Fig. 2.5. The optical cavity of length 60 cm is formed by two highly reflective mirrors, M1 and M2 (Layertec, broadband-coated, reflectivity > 99.7 % over the wavelength range of 450–800 nm). The probe light from a tunable Nd:YAG-pumped optical parametric oscillator (OPO; Opotek, Opolette) is injected to the cavity through the back of M1 and detected after M2 by a photomultiplier tube (Hamamatsu, H6870). At the centre of the optical cavity is a set of pulsed Helmholtz coils (PTCL Electronics, University of Oxford) capable of providing up to a 30 mT field pulse of 3 ms duration. These coils sit around a sample holder comprising a rotation stage (Thorlabs, PRMTZ8, powered by Thorlabs, K-cube), a goniometric stage (Comar Optics, 92 XT 50), and a custom-built plastic holder into which a quartz cuvette (Hellma 165-1-40 1 mm, 160 µl sample volume) can be placed. The rotation and goniometric stage, along with the mirrors and a flipper-mounted pinhole (Thorlabs, FFP90/M with VRC2D05), are used to align the cavity into the TEM_{00} mode before each experiment.

The sample cell can be connected to two separate flow systems. The first (either Bartels Mikrotechnik, MP6-liq or Chemyx, Fusion 100T) allows for flowing of samples and is typically only used for model systems and systems that more readily photobleach without recovery. The second allows for circulation of a coolant (inhibited ethylene glycol in water, 20% v/v) from a chiller (Grant, Optima T100), allowing the sample in the cell to be kept at low enough temperatures so as to prevent degradation (usually 278 K); this is particularly critical for the cryptochrome proteins used in this thesis, which can denature and aggregate at higher temperatures.

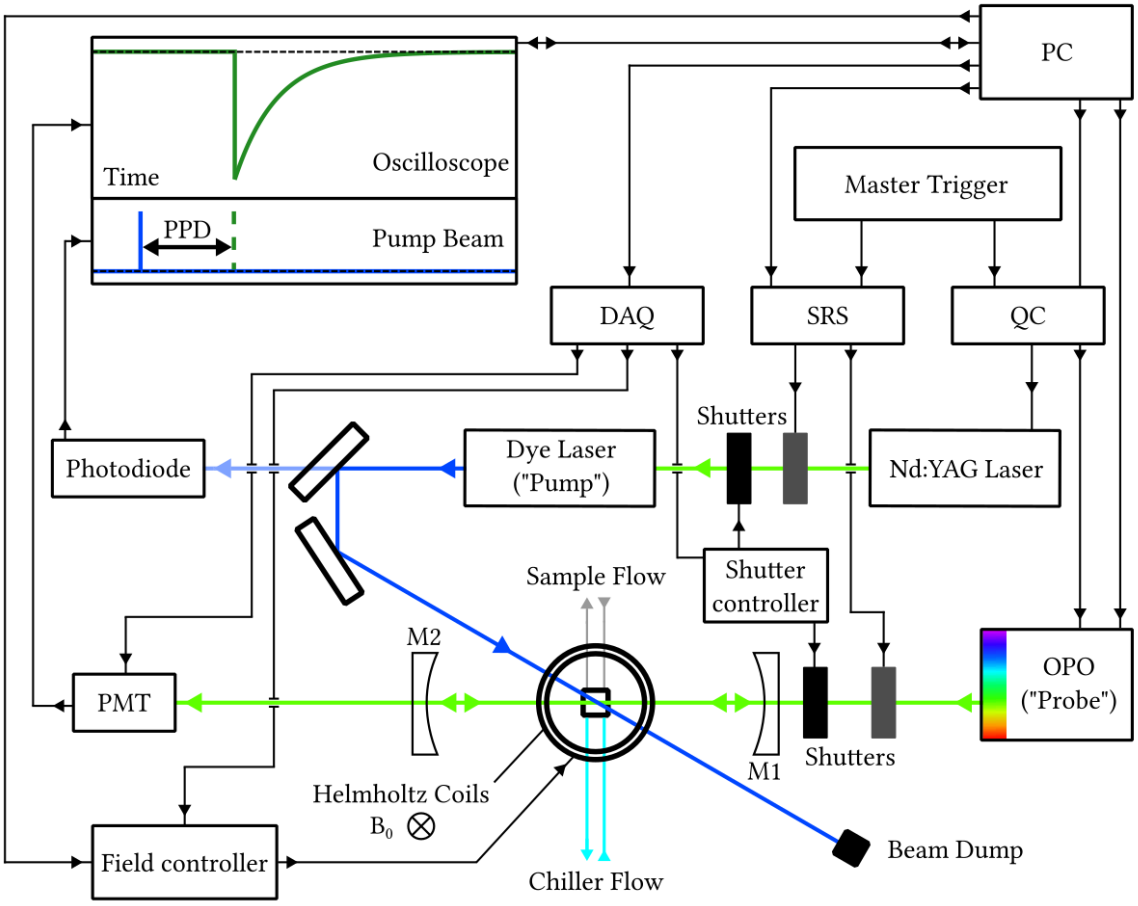


Figure 2.5: Schematic showing the CRDS apparatus. Arrows on connectors indicate the direction of information, light, or liquid flow. The full description of the apparatus is provided in the text. Abbreviations: PPD – pump-probe delay time; DAQ – data acquisition card; SRS – Stanford Research Systems delay generator; QC – Quantum Composers delay generator; PMT – photomultiplier tube; OPO – optical parametric oscillator; M1 and M2 – cavity mirrors.

An additional issue that arises with cooling the cell is that of condensation on the windows, which can cause scattering of the probe beam and a drastic reduction in the ring-down time. This is prevented by gently blowing dry nitrogen gas onto the cell windows and extensive care has been taken to ensure that there are no additional vibrations as a result of its introduction.

The sample is photoexcited at 450 nm with a Nd:YAG-pumped dye laser (Sirah, Cobra, pumped by Continuum, Surelite I at 355 nm); the dye used in this work is Coumarin 450 (Luxottica Exciton). A second photodetector (Thales Optronics, RS350462) is included in the pump laser's beampath to allow measurement of its output power.

In order to improve laser stabilities, the Nd:YAG and OPO lasers are Q-switched at their optimal frequencies (ν = 10 Hz and 20 Hz, respectively). Given that the experiments run at frequencies lower than this (typically 3.33 Hz and 1 Hz), the laser pulses are shuttered to control the frequency at which the experiments are run by a pair of shutters (Thorlabs, SH05/M

powered by SC10) operating at the correct frequency. The Nd:YAG laser is also shuttered before the entry point of the dye laser to prevent dye degradation during experimental pauses or while setting up for an experiment and the OPO is shuttered to prevent entry of the beam into the cavity, both of which are controlled from a single shutter control box (PTCL Electronics, University of Oxford).

The master trigger is provided by a custom-built pulse box (PTCL Electronics, University of Oxford), providing two pulse outputs: one at 20 Hz and the other at $\frac{10}{n}$ Hz, where $n \in \mathbb{N}, 0 < n \leq 10$. This first pulse output acts as the external trigger for a first delay generator (Quantum Composers, 9520) which has the overall function of setting the timings for the two lasers. The second pulse acts as a trigger for a second delay generator (Stanford Research Systems, DG645) which controls the two frequency shutters and acts as the external trigger for the oscilloscope (NI, PXIe-1073 with PXIe-5160). A third output from the master trigger is the current that is sent to the field coils, ultimately controlling the field strength applied.[4]

An input/output (I/O) module (NI, cDAQ-9174),[5] which is controlled from the computer, is used for three purposes: to set the current applied to the coils through an 8-bit connection provided to the master trigger (NI-9403); to open and close the main shutters by sending pulses to the shutter control box (NI-9402), and to set the PMT bias voltage, which acts as the PMT gain (NI-9263).

2.4.2 The Code

The code for this work was written in LabVIEW 2019. In this section, the graphical user interface (GUI) is explored before looking at the underlying code. This subsection is mostly included for completeness and the benefit of future users of the CRDS apparatus.

2.4.2.1 The Graphical User Interface

The GUI can be subdivided into two main sections: the oscilloscope and the experimental controls. These are shown on the left and right of Fig. 2.6, respectively.

The oscilloscope section is designed to look as similar to a standard commercial model, albeit completely encoded into the program and with no physical screen other than on the GUI. The oscilloscope display in Fig. 2.6 shows both channels active with Ch. 0 (blue) showing the ring-down of an empty cavity and Ch. 1 (red) showing the baseline for the photodiode that detects the pump beam.

[4] In Fig. 2.5, this is represented separately from the "Master Trigger" for convenience.
[5] The I/O module is a data acquisition (DAQ) controller comprising three DAQ cards.

The first column of the oscilloscope controls shows the first of the acquisition parameters. The highlighted button keeps the oscilloscope acquiring data at the frequency provided by the SRS delay generator, which is, in turn, governed by the master trigger. Below this, the "Single" button acquires a single trace before pausing acquisition. The "Enforce Realtime" light keeps the sampling rate of the oscilloscope below the maximum real time rate. If set to false, the oscilloscope is able to sample faster, but reconstructs a periodic waveform based on the data that it is able to collect.

The standard horizontal adjustments, such as time per (horizontal) division, sample rate, and horizontal shift are included in the second column of controls. Two indicators (shown with a black background) show the "Actual Sample Rate" and the "Horizontal Offset" (in temporal units) from top to bottom, respectively. The "Number of Records" control allows for multi-recording, which allows the oscilloscope to acquire many triggered waveforms very rapidly without the operating system interrupting the acquisition. Due to the frequencies used in this work, the value of this parameter has always been set to 1, which means that it only acquires the full trace shown on the oscilloscope at the given frequency before recording a new trace as a separate entity.

The third column controls the triggering of the oscilloscope. Going from top to bottom, the triggering channel can be chosen, along with the level of the input that is required to set the trigger off. The "Trigger Slope" can either be positive (the "rising edge") or negative (the "falling edge"), which determines the edge of the rectangular pulse off of which the trigger is taken. The "Trigger Coupling" can be *AC*, *DC*, *HF Reject*, *LF Reject*, or *AC Plus HF Reject*, meaning that certain frequency components are either ignored or expected by the trigger. The "Trigger Holdoff" is a fixed period of time following an initial trigger in which the oscilloscope cannot again register a triggering event. Finally, the "Trigger Delay" is the amount of time from when the oscilloscope registers the trigger to when it acquires the signal.

The last two columns are the controls for the two input channels and show standard controls: "Volts/Div"; vertical "Offset"; and "Input Impedance"; for the latter control, the options are either 50 Ω or 1 MΩ. The "Maximum Input Frequency" control sets the bandwidth and prevents high-frequency noise when sampling at lower rates. This parameter is kept at zero, thus using the default bandwidth of the oscilloscope (500 MHz).

The experimental controls are now considered, going from top left to bottom right.

The top left of the experimental controls has the major controls (Fig. 2.6 b). The "Initialise" button (in faded orange) is the only active button upon start-up of the program and is pressed to initialise the communication between the soft- and hardware. Once this is complete, the button

deactivates (as shown) and all other controls become active. Once set up, the "Start" button commences the experiment. While in an experiment, the "Pause" button can be pressed to stop the acquisition (at the end of the current average for time-resolved and MARY experiments, the end of the current wavelength for time- and wavelength-resolved and wavelength-resolved MARY experiments, or the end of the current PPD for time-resolved MARY experiments) and allow adjustments to other attributes (e.g. alignment of the cavity, PMT gain, etc.). The "Abort" button either terminates the started experiment (at the same point as the "Pause" would take effect) or, if no experiment is running, terminates the connection with the hardware before closing the program.

Fig. 2.6 c) shows the experimental progress indicators. The left-most indicator shows the number of the average being run and the right-most indicator counts down should a pause be required at the end of an average. The central two indicators change depending on the experiment being run, but indicate the variable index being run (in the shown case, a time-resolved experiment only has an index for the PPDs as there is no second variable). The labels automatically change when the experiment type is changed.

Fig. 2.6 d) shows the hardware control. The PMT gain can be adjusted using the slider and the value indicated is the voltage sent through to the PMT unit. To the slider's right is the shutter control for the two main non-frequency-operated shutters. Furthest right is the field test control, which allows the field to switched on at a set value (0 shown in the figure) outside of an experimental run at the frequency determined by the master trigger. All of these elements on the top row of this panel work through the cDAQ unit (see Section 2.4). Immediately below the PMT gain slider is the OPO control, allowing the flashlamp and Q-switch to be controlled from the GUI, rather than the laser unit. The wavelength can also be adjusted, with the current wavelength shown in the left indicator. Any automated commands or outputs from the laser or its software are sent to the larger indicator (which reads "Laser ready"). In cases where a change in PPD is required outside of an experiment (e.g. after an experiment where the final PPD is negative), the control underneath the major laser indicator can be used to send the appropriate commands to the two delay generators. The final button, labelled "Pump Laser Pulse", is there to adjust the pulse delay for the pump laser from the Quantum Composers delay generator. This is required because the Nd:YAG that pumps the dye laser has its frequency halved by a duty cycle from the Quantum Composers delay generator and may, sometimes, be a single pulse out of kilter with the effective Q-switching.

The next panel down (Fig. 2.6 e) houses the experimental parameters which are used in the setup of an experiment. The "Experiment Type" control is a drop-down and allows the user to select which experiment they wish to run; the options are as shown in Fig. 2.4. Below this,

the filename can be entered, which is the name of the folder created for saving of the data. The indicator below ("Field Strength") adjusts depending on the experiment type selected and the value of this parameter can be entered into the control box adjacent. The number of averages for an experiment can be input into the control below this and the wait time (should it be required) into the control therebelow. In order for the experiment to act on the wait time, the "WAIT?" button must be activated (indicated by it turning green). Adjacent to this is the button labelled "MFE?", which is used only for time- and wavelength-resolved experiments where it may not be necessary to obtain the magnetic field effect, but rather just a spectral shape without magnetic field. The two panels on the right-hand side are where the variable values are entered for the experiment. In this case, since the time-resolved experiment only has one variable (*viz.* PPD), only one panel is active and has the name of the variable indicated above it. There are several tabs that are available in each. They are:

- Manual (left panel, first tab): each variable entry is put in separated by a new-line character;
- Vector (left panel, second tab): a list of values is created by providing a start- and end-point, along with a step value;
- Single (right panel, first tab): entries are entered in the same way as for "Manual" above, but the values entered will be applied to all of the entries from the first panel;
- Multi (right panel, second tab): entries are entered into a table so that each of the entries in the first panel has a (potentially) different set of second variable values over which the experiment is run;[6] and
- Step (right panel, third tab): like "Vector" above, a list is created by providing a start- and end-point, along with a step value.

The final panel (Fig. 2.6 f) allows the user to see an approximation of the ring-down time (more accurately the time taken for the trace to go from 90 % to 10 % of its maximum value). This is useful for assessing the alignment, for which the trace can also be plotted by selecting the "RING-DOWN TIME" button. In the trace, one can see a trough in the amplitude before returning to a more stable maximum as it reaches its optimal alignment, here with a "ring-down time" of approximately 3.87 μs.

[6] This may be useful in time- and wavelength-resolved studies where the kinetics at some wavelengths may require fewer/more PPDs.

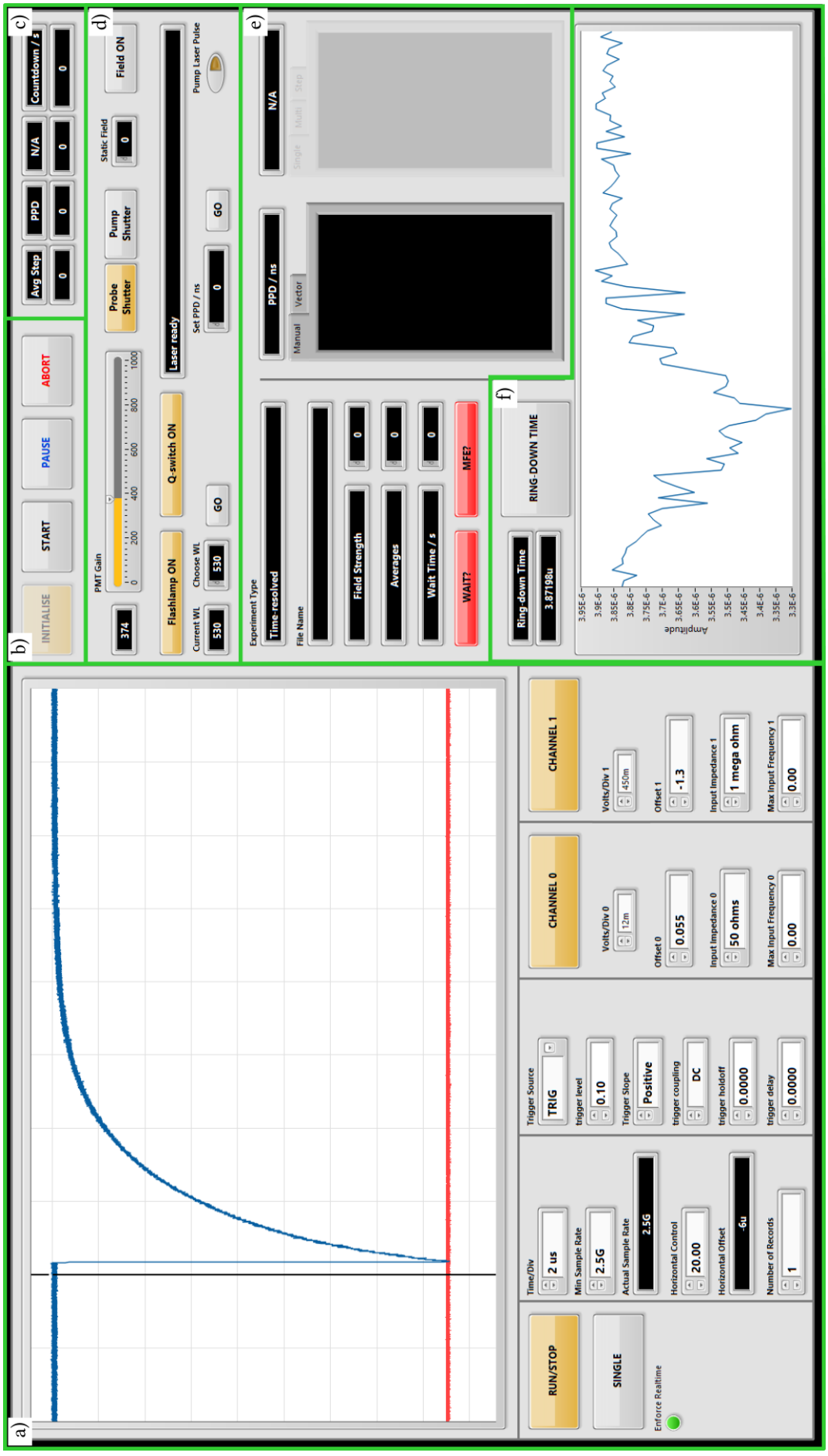


Figure 2.6: Screenshot showing the GUI for the CRDS experiment. The GUI is split into six main sections: a) the oscilloscope and its controls; b) major controls; c) experiment progress indicators; d) hardware control; e) experimental parameters; f) ring-down time and display. Further information about each section is provided in the text.

2.4.2.2 Introduction to Pseudocode

Rather than showing the code itself, which is both complicated and requires knowledge of both LabVIEW and the various manufacturer-produced code libraries, the following sections show a pseudocode that more clearly describes the processes ongoing in the code at different points within running experiments. In order to understand the pseudocode, a legend is provided in Fig. 2.7. Any deviations or clarifications are provided in the figure captions in the respective sections.

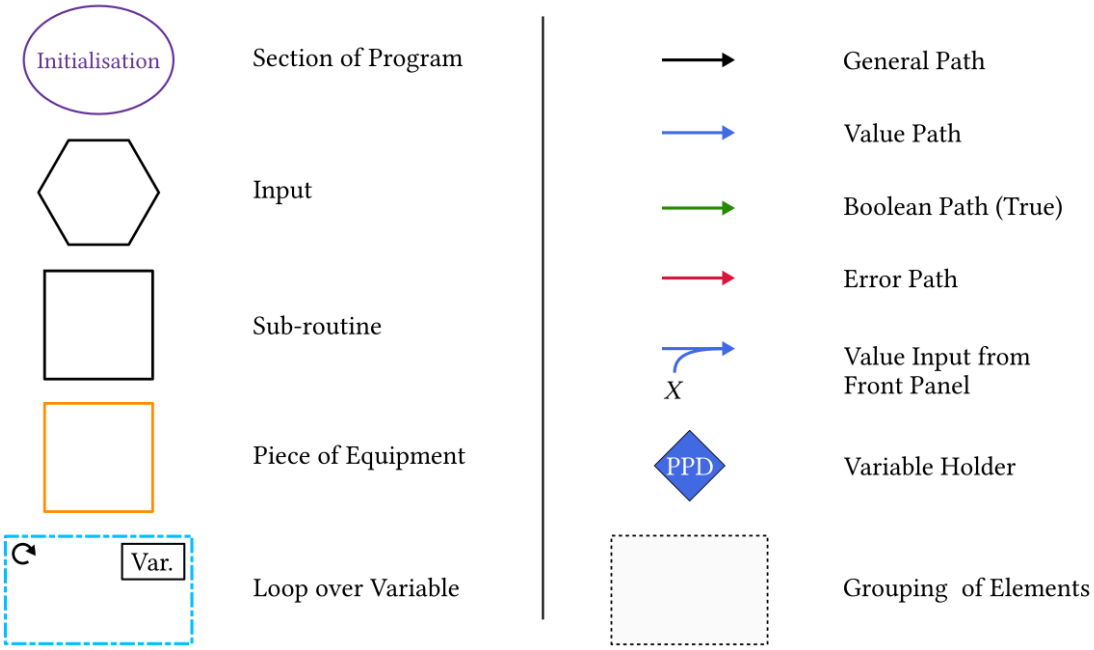


Figure 2.7: Legend showing the meanings of symbols in the pseudocode used in this chapter. Any deviations are indicated in future figure captions.

2.4.2.3 Initialisation

The initialisation sequence is shown in Fig. 2.8.

Upon running the program, all controls on the GUI are disabled except for the "Initialisation" button. This allows the user to ensure that all instruments are switched on prior to attempting formal initialisation. Once the "Initialisation" button is pressed, the OPO is initialised with the default parameters (as defined by Opotek) and the motors homed. The "External Control" configuration is chosen and the wavelength tuned to 530 nm (although the flashlamp remains off). The internal Q-switch delay is set to 177 µs to prevent damage to the laser, while also maximising the output power. The Quantum Composers (QC) and Stanford Research Systems (SRS) delay generators are then initialised with the values shown in Tables 2.1 and 2.2, respectively, with the pump-probe delay time set to 0 s. The 177 µs Q-switch delay can be seen in

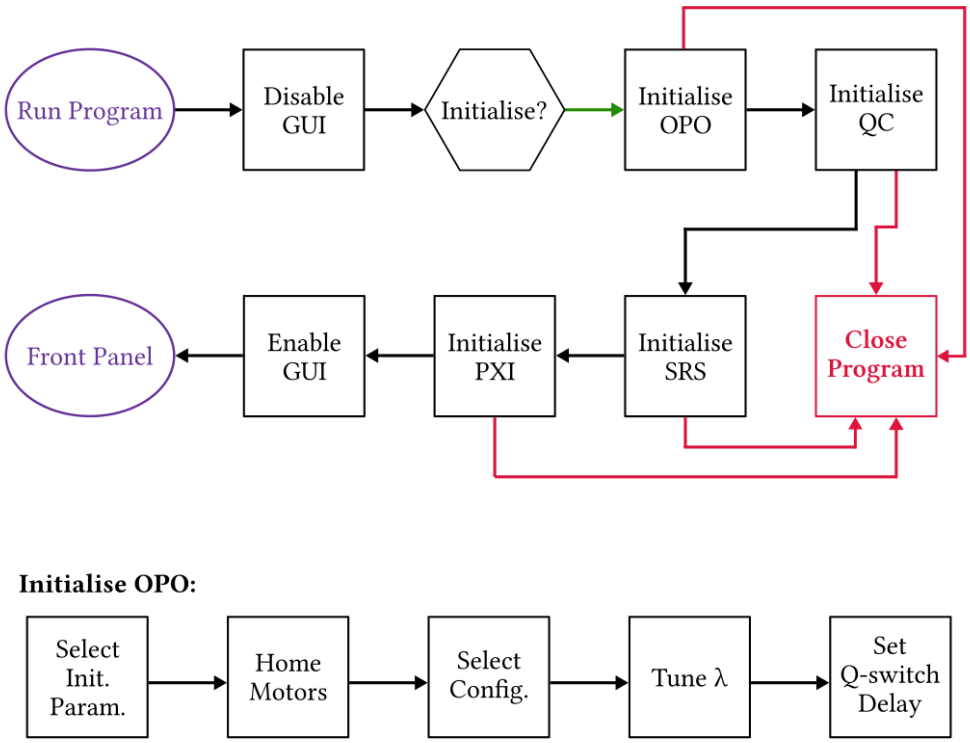


Figure 2.8: Pseudocode showing the initialisation procedure for the CRDS experiment. The OPO initialisation sequence is shown in greater detail below the main procedure. The initialisation parameters for the Quantum Composer (QC) and Stanford Research Systems (SRS) delay generators are shown in Tables 2.1 and 2.2, respectively. The PXI is the oscilloscope. The red arrows show the path followed if an error is encountered in the block from which it originates.

Channel E of the QC. The oscilloscope (PXI) is also initialised with settings that are a good estimate of what is required (as can be seen in Fig. 2.6) for the experiments used in this thesis and set to "Off".

If there is an error during any of the initialisations (shown by red arrows in Fig. 2.8), the program is immediately closed. If there are no errors, the GUI is activated for use and the pre-experiment front panel options are loaded.

Channel	A	B	C	D	E	F	G	H
On?	✓	✓	✓	X	✓	X	✓	X
Sync. Source	B	T_0	T_0	—	C	—	A	—
Mode	Normal	Normal	Duty Cycle (1–1)	—	Normal	—	Normal	—
Width / μs	11	11	11	—	11	—	11	—
Delay / μs	0	11288.377	11764.726	—	177.664	—	665.168	—

Table 2.1: The initialisation parameters used for the Quantum Composers delay generator, which is mainly used for controlling the timings for the two laser on the CRDS.

Channel	A	B	C	D	E	F	G	H
Sync. Source	T_0	A	A	C	A	E	C	G
Delay / ms	1.04	90	0	45	0	1×10^{-3}	10.8995	1×10^{-3}

Table 2.2: The initialisation parameters used for the Stanford Research Systems delay generator which is used to control the frequency shutters (see Section 2.4) and provide the reference trigger to the oscilloscope.

2.4.2.4 Pre-experiment Front Panel Control

The pre-experiment front panel control is shown in Fig. 2.9. There are two main components of this section of the code: the oscilloscope and the additional hardware adjustments. The input parameters for experiments and the adjustments made by adjusting the "Experiment Type" parameter are not shown here for clarity, but are discussed in Section 2.4.2.1. Similarly, the two components are, in fact, two parallel loops, but are shown as separate groupings within a single loop for clarity.

First the oscilloscope. The parameters are housed in an "event structure", which only runs when a parameter is changed. Thus, the "Set Params" structure takes the previous values until updated and loads them to the oscilloscope before it is primed for measurement. The active traces, determined by Boolean values of the "Channel 0" and "Channel 1" buttons on the GUI (see Fig. 2.6), are then acquired after the trigger and displayed on the oscilloscope panel. If Channel 0 (which shows the trace recorded by the PMT, namely that of the optical cavity and ring-down) is active, the time taken for the exponential decay to go from 90 % to 10 % of its maximum value is determined and reported. If the Boolean "RING-DOWN TIME" switch is activated, this temporal value is plotted with each acquired trace to allow for alignment of the cavity. This then returns to the start with the setting of parameters (if changed).

The parameters that can be adjusted have been adjusted to appear more like a commercial oscilloscope for ease of use; these can be seen in the "Parameters" box and are explained further in Section 2.4.2.1.

The additional adjustment controls are also contained in an event structure so as to prevent overloading the CPU with too many commands to the various pieces of hardware.

The two main shutters (one for each of the pump and the probe beams) can be controlled by Boolean switches, the value of which is then communicated by a change in voltage from the compact DAQ unit (NI, cDAQ-9174 and NI-9402) to the custom-built shutter control unit. This Boolean value either opens (true) or closes (false) the shutters.

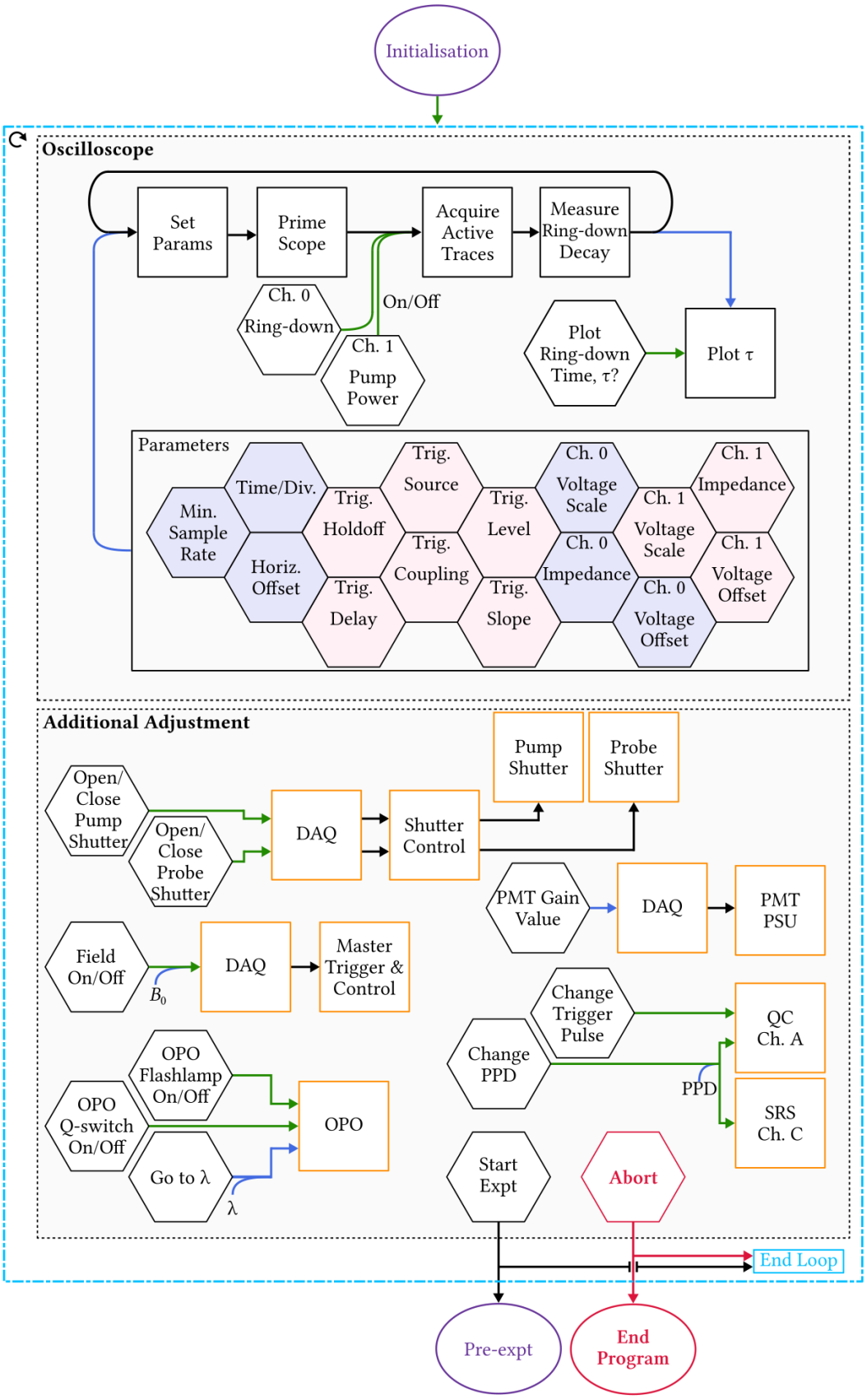


Figure 2.9: Pseudocode showing the two parallel loops (here shown as separate boxes within a single loop) for control of the front panel and oscilloscope before starting an experiment. The loops are terminated either by closing the program with the "Abort" button or by starting the experiment. The "Parameters" are grouped by colour. Further information is provided in the text.

A field switch also proceeds through the cDAQ (NI-9403) by providing an 8-bit number (provided from the field strength input – ranging from 0 to 255 – on the GUI) to the master trigger control, which then adjusts the current being sent to the coils.

The PMT gain is controlled by a slider on the GUI and triggers a scaleable 0–10 V voltage from the cDAQ (NI-9263) to a voltage amplifier, which powers the PMT.

The OPO flashlamp and Q-switch are adjusted using the software development kit provided by Opotek, which requires only a Boolean input. The wavelength-changing subroutine (subVI) provided was modified to correct the number of inputs required for the dynamic link library (DLL) and takes the wavelength to which the laser is tuned from the input on the GUI.

The pump-probe delay time (PPD) can be adjusted by modifying channels A and C on the QC and SRS, respectively. As described in Section 2.4.2.1, an offset in the trigger for the 20 Hz OPO can be activated by a Boolean control on the GUI ("Change Trigger Pulse").

The loop controlling the front panel can be exited either by closing the program (using the "Abort" button) or by starting the prepared experiment; this ends the overall loop (actually two parallel loops) and, in the latter case, proceeds to the pre-experiment phase.

2.4.2.5 Starting an Experiment

If an experiment is started (rather than the program being exited), the variables are processed, with Variable 1 being a 1D array and Variable 2 a 2D array (one row for each entry in the Variable 1 array). For the second variable, this is done by either repeating the input (in the case of the "Single" or "Step" entry) or by importing the 2D table entry (for the "Multi" input). The constant parameter is the input that codes either the field strength (in time-resolved or time- and wavelength-resolved experiments) or pump-probe delay time (for the MARY experiment) and is the input immediately below the "File Name" input on Fig. 2.6. The assignment of variables and the constant parameter can be seen in Table 2.3. Depending on experiment type, whichever variable is the magnetic field strength is checked to ensure that no entry exceeds the maximum allowed input (255, this being the maximum value in 8-bit). If there is a field value that is too large, an error message is produced and the program returns to the front panel to allow for adjustment. If all the field values are in range, then a new folder is created with the input name and a parameter file is written to record all the settings that have been used. Once complete, the experiment starts.

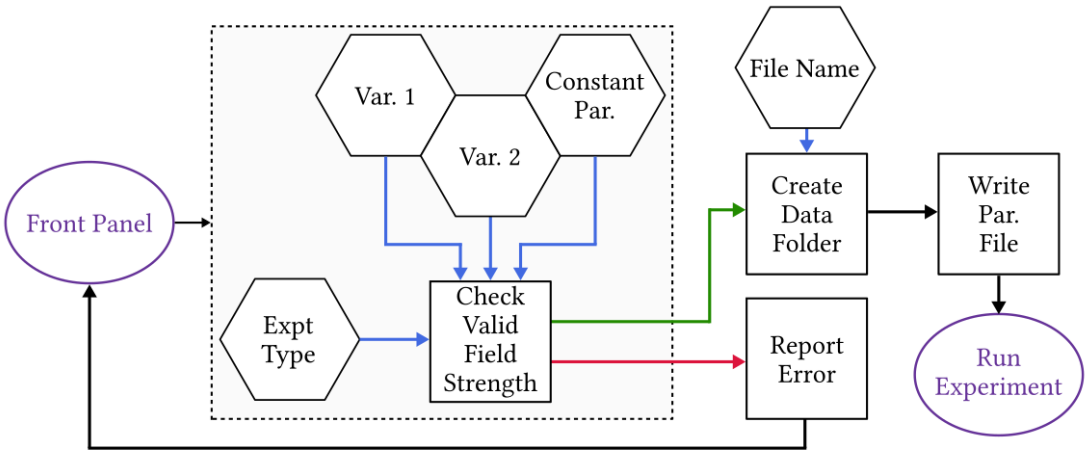


Figure 2.10: Pseudocode showing the automated procedure on starting an experiment. The variable/parameter that encodes the field strength is checked to ensure that it is within range before continuing. If this test is failed, an error message is shown and the program returns to the front panel. If the field value(s) is (are) in range, the data folder is created and parameter file written to it before starting the experiment.

Experiment Type	Var. 1	Var. 2	Constant Par.
Time-resolved	PPD	N/A	Field Strength
MARY	Field Strength	N/A	PPD
Time- and Wavelength-resolved	Wavelength	PPD	Field Strength*
Time-resolved MARY	PPD	Field Strength	N/A
Wavelength-resolved MARY	Wavelength	Field Strength	PPD

Table 2.3: Table showing the assignment of parameters for each experimental type. The field strength for the time- and wavelength-resolved experiment (starred) can be excluded if there is no interest in magnetic field effects in the experiment (see Section 2.4.2.1). The two variable names are displayed above their inputs on the front panel (Fig. 2.6).

2.4.2.6 Running the Experiments

The Time-resolved Experiment

The time-resolved experiment is encased in a loop that runs over the number of averages set, unless terminated earlier by aborting the experiment. The pump-probe delay (PPD) times are randomised and include at least one negative time, *viz.* the pump pulse comes after the probe. Both the pump and probe shutters are opened before entering a second loop that runs over the number of PPDs. For each iteration, the randomised PPD is set on channels A and C of the QC and SRS delay generators, respectively, and the field is set to the constant parameter's input value. The "on" ring-down trace is recorded before the field is switched off and the "off" trace recorded. After acquisition at all the PPDs is complete, the shutters are closed and the ring-down traces, as well as the order of the PPDs, are saved into the folder created in

the "Pre-experiment" section of the code. If the "Wait" button is set to true, then a pause is introduced for the number of seconds input on the front panel. If at the end of the average the "Pause" button is true, the oscilloscope is returned to its primed setting and displays the traces recorded by the input channels at the set frequency. The shutters can be opened and closed and the PMT gain slider adjusted allowing the user to correct alignment issues or just pause the experiment until ready to be resumed. Once this is complete, the next average follows the same pattern. If there are no more averages, then there is a pop-up to inform the user that the experiment is complete and the program returns to the front panel. All of this is shown schematically in Fig. 2.11.

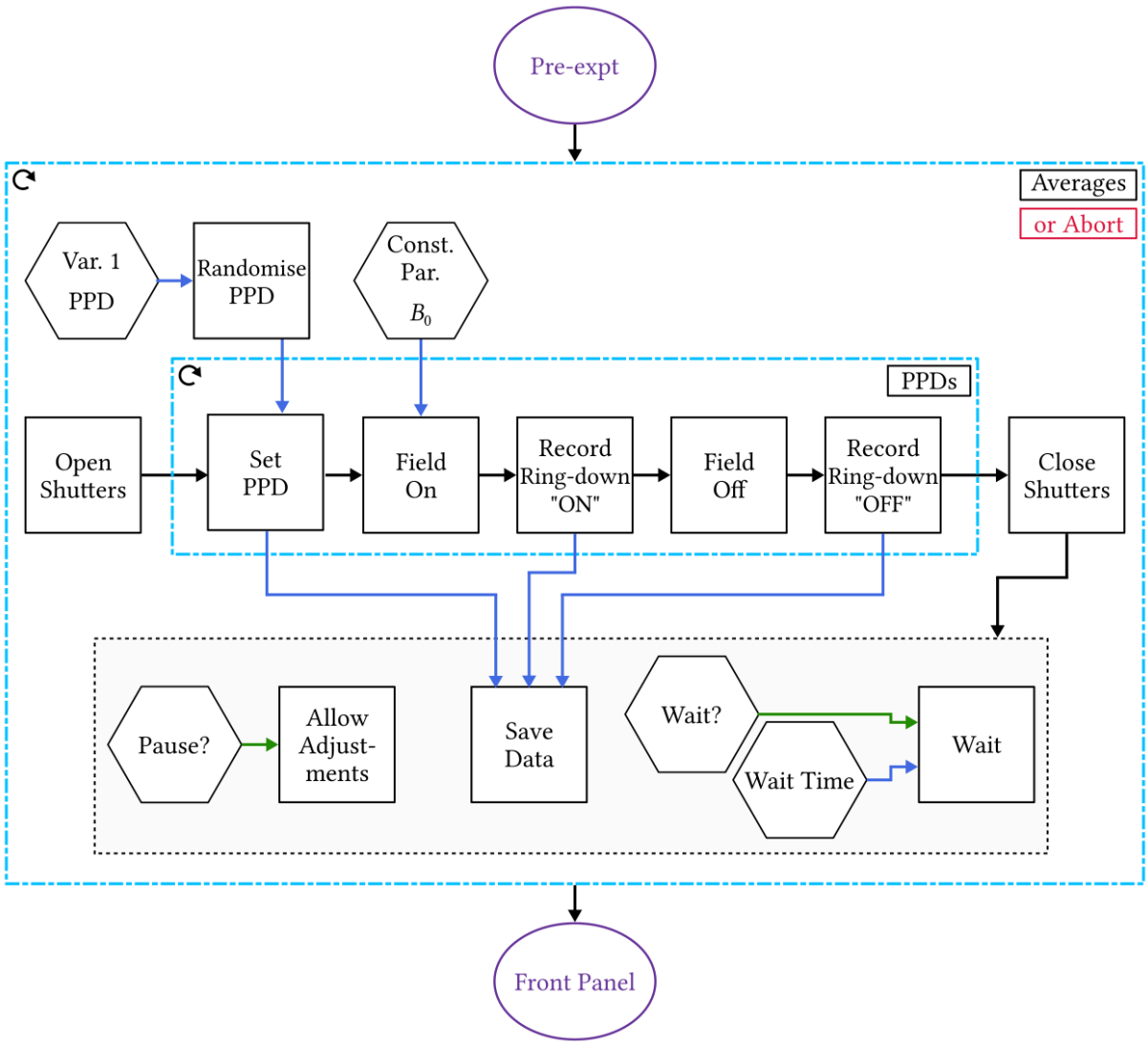


Figure 2.11: Pseudocode showing the procedure for the time-resolved experiment. Following the closing of the shutters, the section shown at the bottom allows for either an automated wait before starting the next average or a manual pause, from which the front panel is activated to allow for adjustments, especially realignment of the cavity. Further information is provided in the text.

In the instance where an experiment needs to be stopped, the "Abort" button can be clicked and the outer averaging loop is terminated at the end of the current average. This too returns the program back to the front panel after a pop-up.

The MARY Experiment

The MARY experiment also occurs within a single averaging loop. Prior to the first average, the pump-probe delay time is set (which is constant over the course of the experiment) using the constant parameter input from the front panel. For each iteration of the loop,

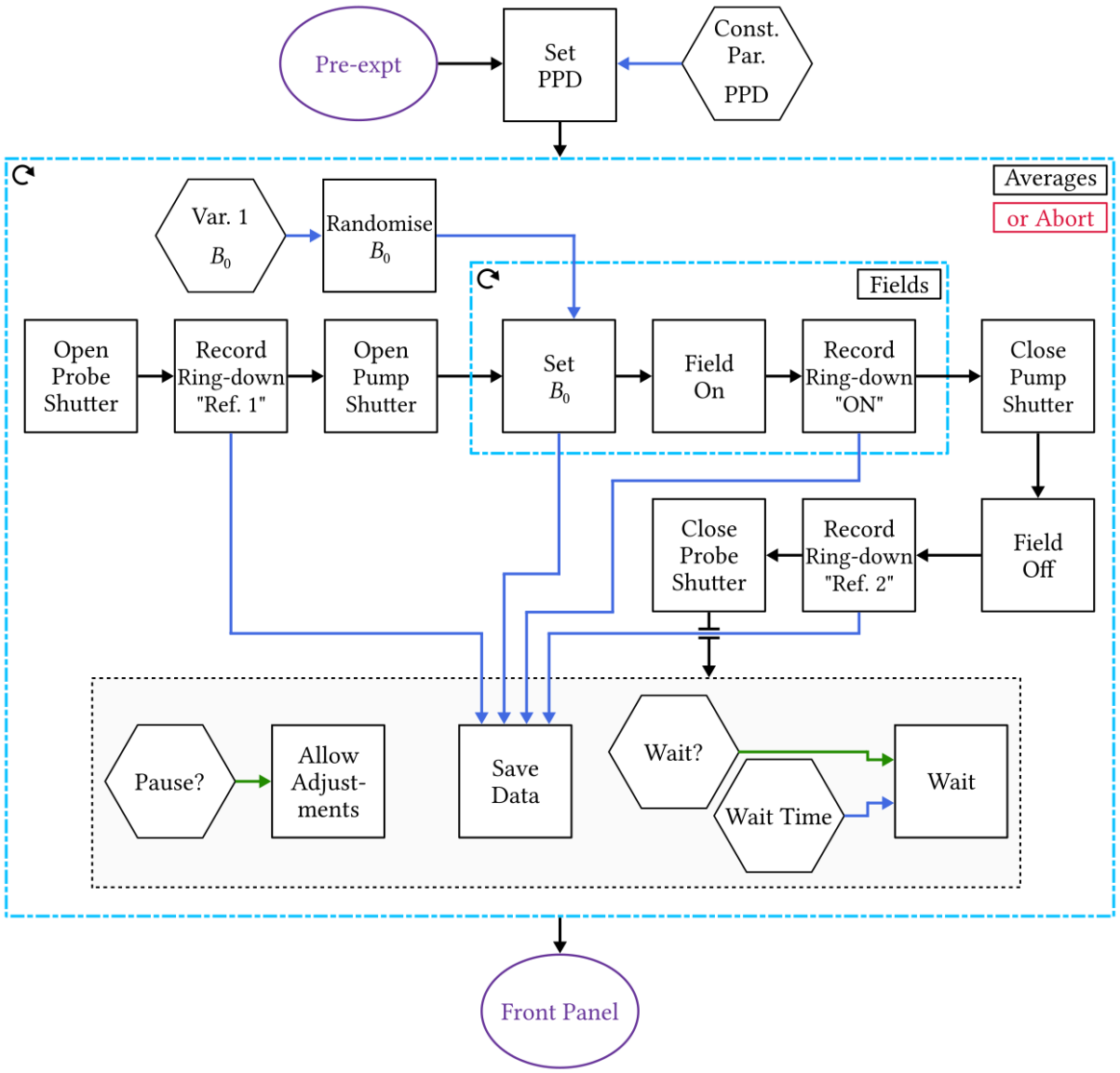


Figure 2.12: Pseudocode showing the procedure for the MARY experiment. Following the closing of the probe shutter, the section shown at the bottom allows for either an automated wait before starting the next average or a manual pause, from which the front panel is activated to allow for adjustments, especially realignment of the cavity. Further information is provided in the text.

the field values (shown as B_0 in Fig. 2.12) are randomised and the probe shutter is opened with the field off to record a non-photoexcited ring-down trace (much like the negative pump-probe delays in the time-resolved experiment); this trace acts as the first reference trace in order to obtain a ΔA value. After the reference trace is acquired, the pump shutter is opened to allow photoexcitation. A second loop then runs over the randomised field strengths where the traces with field on at these various B_0 values are recorded, before closing the pump shutter and turning off the field to record a second non-photoexcited reference ring-down trace and then closing the probe shutter.

Identically to the time-resolved experiment, the data (two reference (non-photoexcited) traces, the "on" traces, and the randomised field values) are saved and the code allows for both a delay before starting the next average or pausing to make adjustments. If the "Abort" button has been pressed, the experiment ends at the end of the current average and a pop-up indicates its completion and the program returns to the front panel control; the same is true if there are no more averages to be taken. All of this is schematically presented in Fig. 2.12.

The Time- and Wavelength-resolved Experiment

The time- and wavelength-resolved experiment is based on the time-resolved experiment (see above) with only a few minor adjustments. The averaging loop in the time-resolved experiment is replaced with one that runs over the wavelengths of interest. The wavelength is set and the PMT gain adjusted to utilise the full input range of the oscilloscope. The same procedure as the time-resolved case (see Fig. 2.11) then occurs before tuning to the next wavelength. Once the data from all of the wavelengths are collected, then the averaging loop can proceed. The experiments are, therefore, much more time consuming and, consequently, fewer averages are usually taken. The procedure is shown schematically in Fig. 2.13.

The Time-resolved MARY Experiment

The time-resolved MARY experiment is based on the MARY experiment (see above) with only one significant adjustment: the pump-probe delay (PPD) time is altered for the different MARY experiments. As such, the (randomised) PPD is set and then followed by the standard MARY experiment procedure before data at the next PPD are recorded. Once the experiment has finished for all the PPDs in the list, then the process can be repeated to acquire further averages. This is all shown schematically in Fig. 2.14.

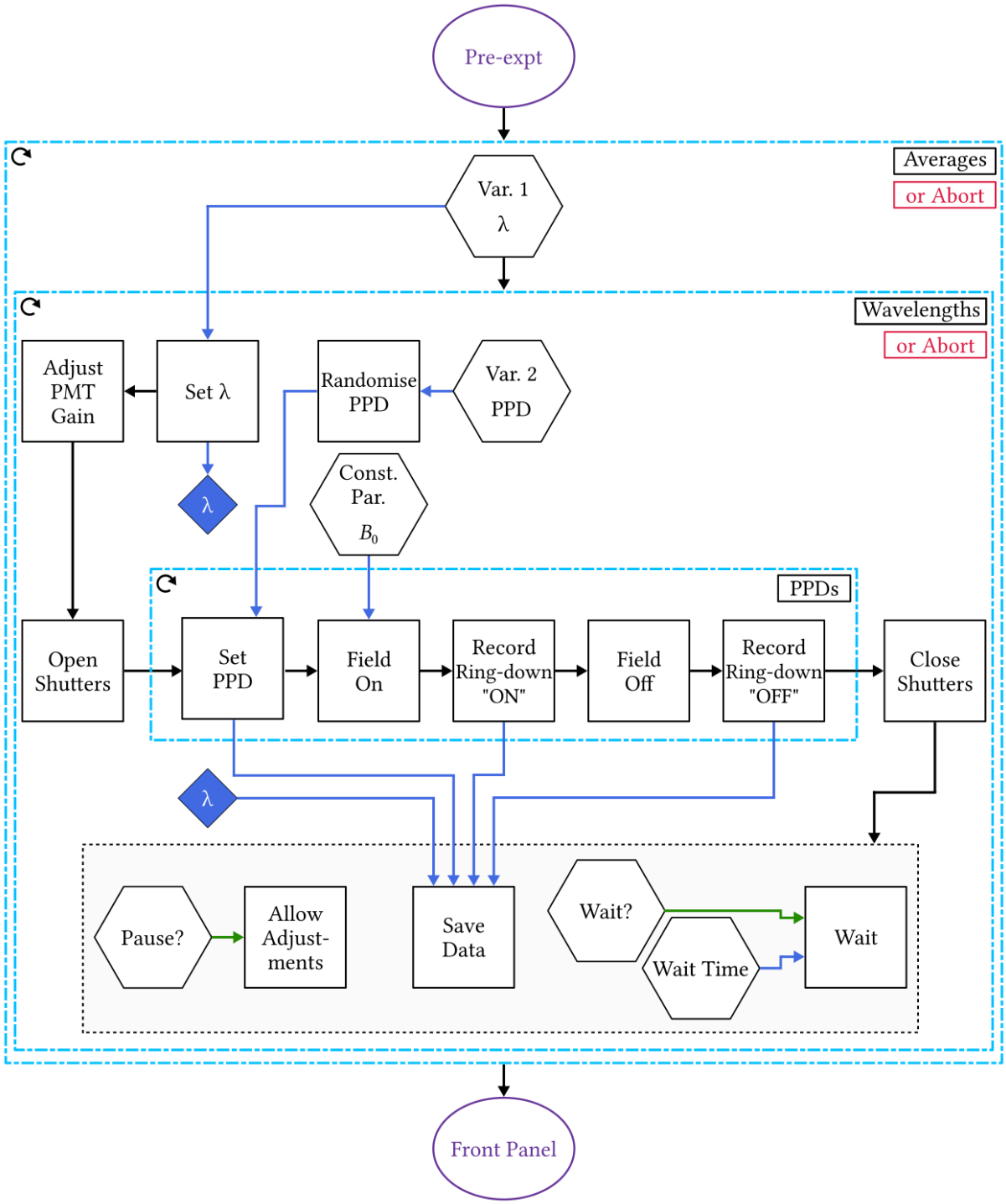


Figure 2.13: Pseudocode showing the procedure for the time- and wavelength-resolved experiment. Following the closing of the shutters, the section shown at the bottom allows for either an automated wait before starting the next average or a manual pause, from which the front panel is activated to allow for adjustments, especially realignment of the cavity. Further information is provided in the text.

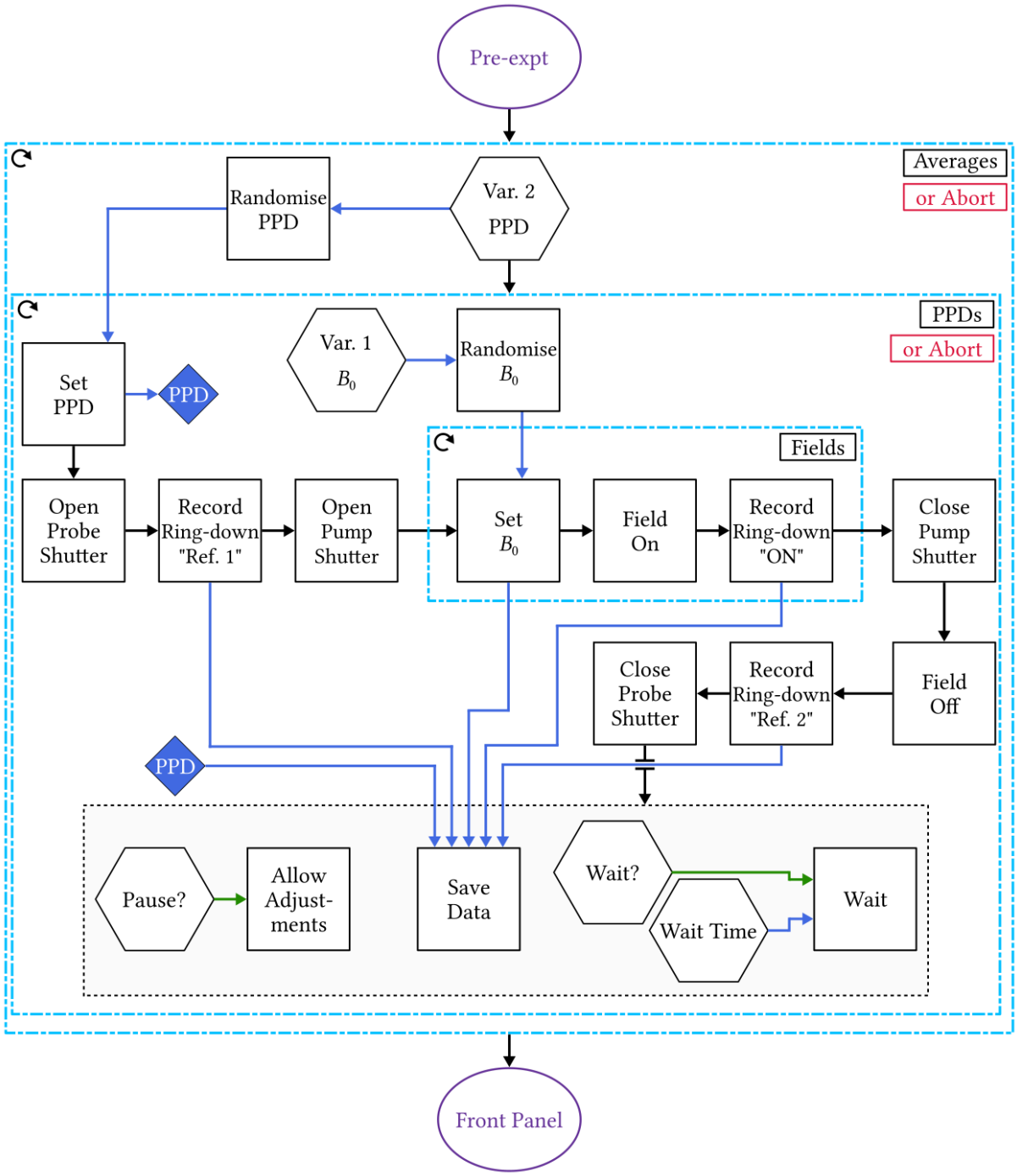


Figure 2.14: Pseudocode showing the procedure for the time-resolved MARY experiment. Following the closing of the probe shutter, the section shown at the bottom allows for either an automated wait before starting the next average or a manual pause, from which the front panel is activated to allow for adjustments, especially realignment of the cavity. Further information is provided in the text.

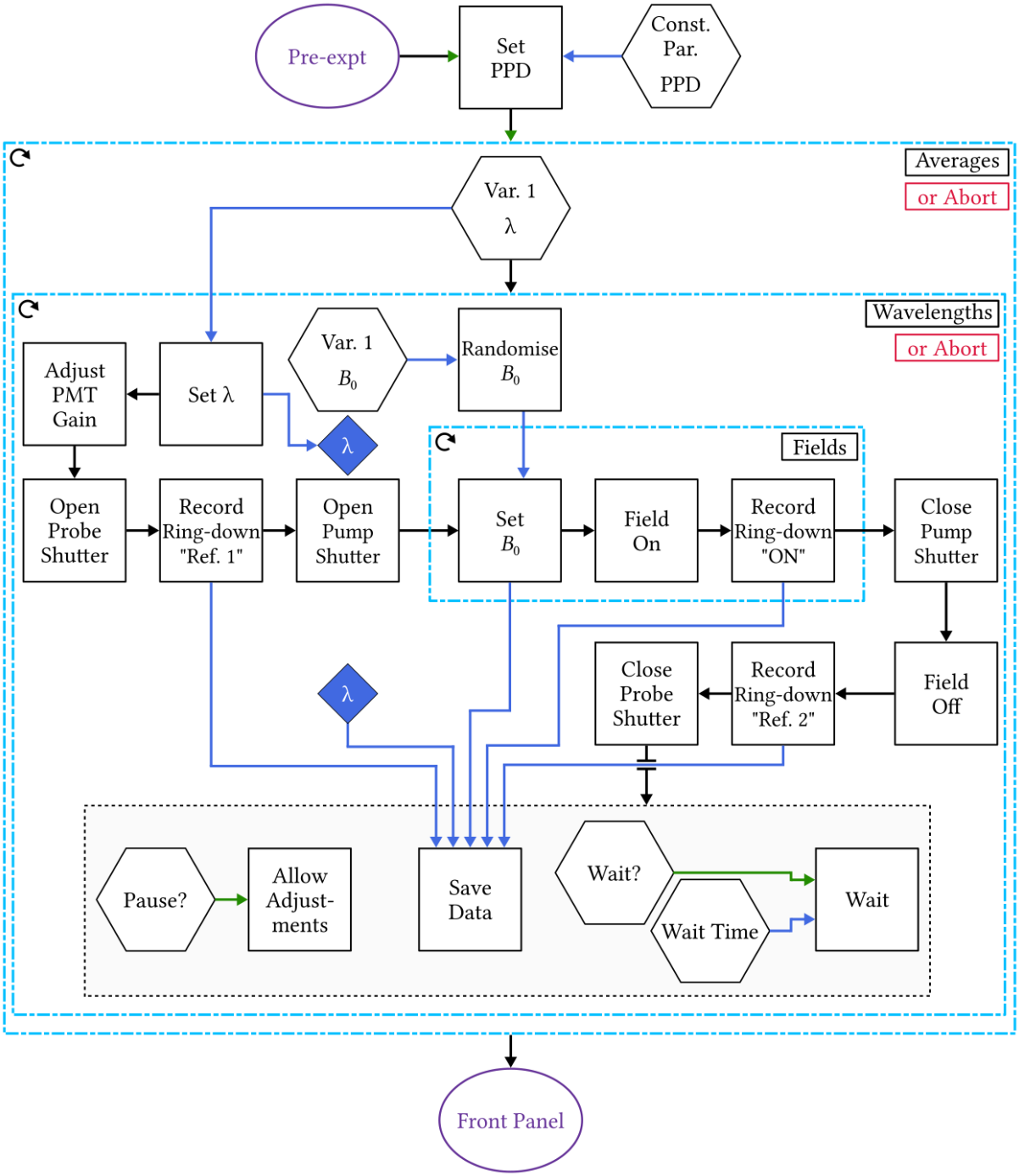


Figure 2.15: Pseudocode showing the procedure for the wavelength-resolved MARY experiment. Following the closing of the probe shutter, the section shown at the bottom allows for either an automated wait before starting the next average or a manual pause, from which the front panel is activated to allow for adjustments, especially realignment of the cavity. Further information is provided in the text.

The Wavelength-resolved MARY Experiment

The wavelength-resolved MARY is also based on the MARY experiment (see above), with this being performed at different wavelengths. The pump-probe delay is constant throughout and set before starting the experiment from the constant parameter on the GUI. The probe beam is then tuned to the first wavelength and the PMT gain adjusted (as in the time- and wavelength-resolved experiment above) to make full use of the oscilloscope range. The MARY experiment is then performed before moving to the next wavelength and repeating. Once all the wavelengths are complete, the process can be repeated to acquire more averages. This experiment is shown schematically in Fig. 2.15.

It should be noted that this experimental type was coded for completeness of the double-variable experiments and has not been used in this thesis.

2.5 Role of CRDS in Understanding Biological Phenomena

One of the challenges of measuring cryptochromes using cavity-based techniques is the fact that they cannot be converted to the gas phase, which would allow for far longer path lengths and, consequently, larger ring-down times. Nevertheless, CRDS can play an important role in understanding light-induced transient processes in biological samples.

In trying to understand magnetic field effects in cryptochrome proteins through the radical pair mechanism (as discussed in Sections 1.3 and 1.5), many techniques are required to understand all of the aspects that make up this magnetosensitivity and the potential downstream processes in the signalling pathway. These techniques include:

- mass spectrometry, both:
  - native MS, used to better understand the stoichiometry, topology and inter-protein interactions; and
  - hydrogen-deuterium exchange (HDX), used to determine the surface exposition of residues in the protein under different conditions;
- electron paramagnetic resonance, used to determine the nature of the radical pair and the inter-radical distance;
- crystallography, used to understand the structures of proteins;

- biologically focussed techniques, such as:
  - behavioural studies to control certain variables that may play a role in magnetoreception;
  - molecular dynamics, to understand protein structures and the effects of mutations;
  - bioinformatics, to understand the evolution of species and the changes in protein sequences; and
  - staining, to determine the locations of the proteins of interest; and
- optical techniques, such as single-pass picosecond transient absorption (ps-TA), and other cavity-based techniques.

Within the absorptive optical techniques commonly used to measure similar samples, CRDS sits in between the ps-TA and broadband cavity-enhanced absorption spectroscopies (BBCEAS).[7] Relative to the ps-TA, the CRDS provides an increased sensitivity as a result of multi-passing within the optical cavity [123]. The initial nanosecond timescale, for which the ps-TA is crucial as a result of the limited temporal resolution of CRDS, is also not of great interest for the study of magnetic field effects. This is because the initial electron transfer process which takes place on this timescale is not magnetically sensitive. In comparison with the BBCEAS, CRDS achieves the time-resolution that BBCEAS cannot offer, but is both substantially slower at collecting wavelength-resolved data and cannot assess the steady state behaviour of the samples.

CRDS is, therefore, perfectly placed to measure the small changes that occur upon application of a magnetic field to a transient species and can, alongside the other techniques, provide understanding of the magnetosensitive biological processes.

[7] BBCEAS is a steady-state multi-pass technique. The sample is continuously photoexcited while broadband light from a supercontinuum source is used as the probe beam, enabling wavelength resolution from a single pulse of light.

Chapter 3

Testing the Improved Cavity Ring-down Spectrometer with a Model System

3.1 Introduction

Before considering the biological samples of interest – cryptochromes – it was critical to ensure that the rebuilt CRDS apparatus was able to reproduce results on better-known systems. In this work, a solution of flavin mononucleotide (FMN) and hen egg-white lysozyme (HEWL) was chosen as it has a well-characterised magnetic field effect, and is sufficiently inexpensive

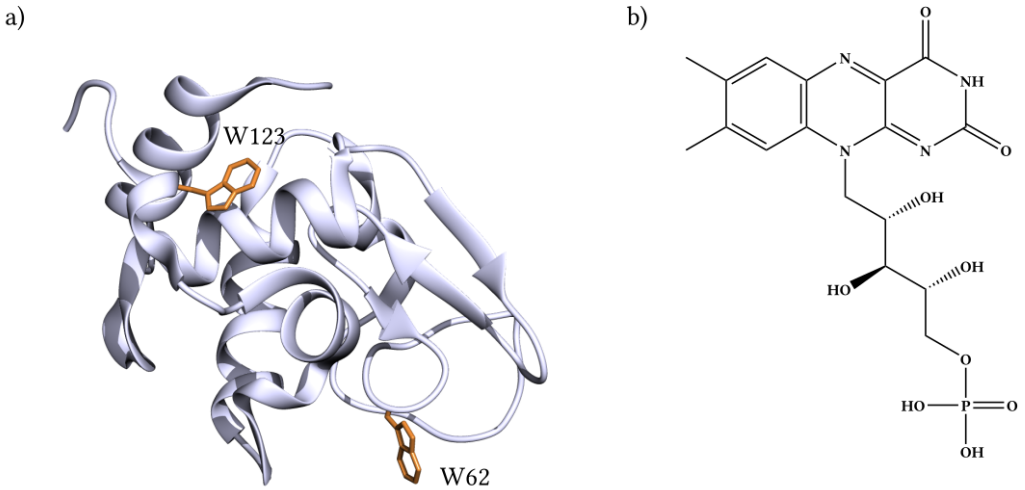


Figure 3.1: a) Secondary structure of hen egg-white lysozyme (HEWL; PDB: 5WR9) [124]. The two surface-exposed tryptophan residues at positions 62 and 123 (W62 and W123, respectively), which are the most likely candidates for the electron-transfer process (to the flavin) leading to the radical pair, are shown in orange [125]. b) Chemical structure of flavin mononucleotide (FMN).

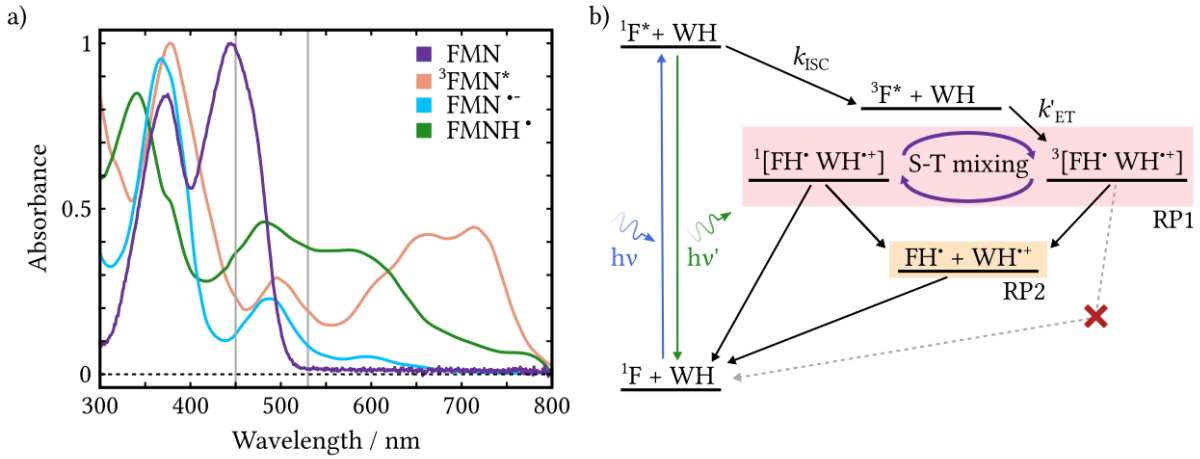


Figure 3.2: a) UV-vis spectrum of aqueous FMN (purple, normalised to the peak at 445 nm) showing the two absorption peaks centred at 373 nm and 445 nm, which are assigned to the $S_0 \longrightarrow S_2\,(n \longrightarrow \pi^*)$ and $S_0 \longrightarrow S_1\,(\pi \longrightarrow \pi^*)$ transitions, respectively. Spectra for the excited state and radical flavin species are reproduced from Ref. [126] and are scaled to the vertical scale shown for FMN (purple), as shown in the reference. Experiments are performed with photoexcitation at 450 nm and wavelength-unresolved measurements are recorded with a probe wavelength of 530 nm, both indicated by grey lines. b) Photoscheme for the FMN/HEWL system. The flavin is photoexcited and undergoes intersystem crossing (ISC). This is followed by electron transfer (ET) from one of the surface-exposed tryptophan residues in the HEWL and protonation of the newly formed flavin anion from a solvent water molecule to form the radical pair (RP1), which can undergo singlet-triplet (S-T) mixing. Only the singlet state can recombine to the ground state due to spin conservation (the inability of the triplet to undergo this recombination is indicated by the red cross on the dashed grey line). The radical species can also drift out of their solvent cage and may either form a second radical pair which can recombine back to the ground state – again, only if this radical pair is in an overall singlet state – or separately return to the ground state. The radicals that diffuse apart are summarised as RP2.

and conveniently accessible so as to be used as a model system. FMN/HEWL as a sample had already been measured on the previous CRDS instrument by Dr D. Sheppard, allowing for comparison [127]. The structures of HEWL and FMN are shown in Fig. 3.1 a) and b), respectively [124].

Fig. 3.2 a) shows the UV-vis spectrum of FMN. The two peaks at 445 nm and 373 nm are assigned to the $S_0 \longrightarrow S_1\,(\pi \longrightarrow \pi^*)$ and $S_0 \longrightarrow S_2\,(n \longrightarrow \pi^*)$ transitions, respectively [128].

As described in Section 1.3 and shown in the photoscheme in Fig. 3.2 b), ground state FMN is photoexcited at 450 nm,[1] close to the $S_0 \longrightarrow S_1$ absorption maximum of FMN, to form the excited

[1] All experiments in this chapter employ photoexcitation at 450 nm with a pulse energy of 300 µJ.

flavin singlet, ^{1}FMN*. This undergoes intersystem crossing on a nanosecond timescale, yielding the excited triplet state (^{3}FMN*) before there is an electron transfer from a surface-exposed tryptophan residue (W) – most likely W62 or W123,[2] or both (shown in orange in Fig. 3.1 a) – to form the radical pair (RP1) within a solvent cage [125]. This radical pair (often called the "geminate pair") is triplet-born due to the faster rate constant of the intersystem crossing, k_{ISC}, in comparison to that of electron transfer, k_{ET}, and the conservation of spin on electron transfer [123]. Once formed, the radical pair can interconvert between the singlet and triplet states under processes collectively known as "S-T mixing" (see Section 1.2.2) while only singlet radical pairs can recombine back to the ground state due to spin conservation.

Radicals that do not recombine to the ground state are able to escape their solvent cage and form free radicals which diffuse through solution. These free radicals can: recombine upon encountering another radical species, returning to the ground state if the overall radical pair is in a singlet state; simply return to the ground state as separate entities; or remain in the same solvent cage, but form species that prevent the reverse electron transfer, possibly by deprotonation [127]. These three states comprising the long-lived radicals that escaped the solvent cage and cannot recombine geminately are represented by RP2 in Fig. 3.2 b). This non-geminate recombination is much slower than that of the geminate radical pair and therefore dominates the radical population being measured [127].

As already discussed in Section 1.4, the T_+ and T_- states become energetically separated from the S/T_0 manifold as the field increases as a result of the Zeeman interaction, reducing the singlet-triplet mixing ability. This means that at high fields, in the case of a triplet-born radical pair, there is a greater concentration of RP2 being formed (since there is less singlet state that can recombine to the ground state, instead allowing the formation of free radicals) in comparison to zero field. This leads to a positive magnetic field effect by CRDS (i.e. an absorption-based technique) when measuring at wavelengths corresponding to the radical absorption (in this case, the radical species with absorptive spectra at 530 nm, marked by a grey vertical line in Fig. 3.2 a).

All measurements in this chapter were made on FMN (10 μM) and HEWL (500 μM) in water (Milli-Q, resistivity 18.2 MΩ cm) at pH ≈ 7.

[2]Residues within proteins are usually labelled by their single-letter code (e.g. "W" for tryptophan or "F" for phenylalanine) and the residue number, numbered from the N-terminus end to the C-terminus end.

3.2 Results

3.2.1 Time-resolved Measurement of FMN/HEWL

Fig. 3.3 a) shows the time-resolved CRDS spectrum of FMN/HEWL recorded at 530 nm, close to the peak of the radical absorption spectrum, i.e. the radical concentration is being measured. The sample is photoexcited, after which the radical pair is formed in a few nanoseconds [125]. The sample is then measured by the probe laser at a set of pump-probe delay times (PPDs) following photoexcitation (with the earliest at 250 ns), as well as two prior to photoexcitation (not shown) which are used as reference measurements (see Section 2.2.1).

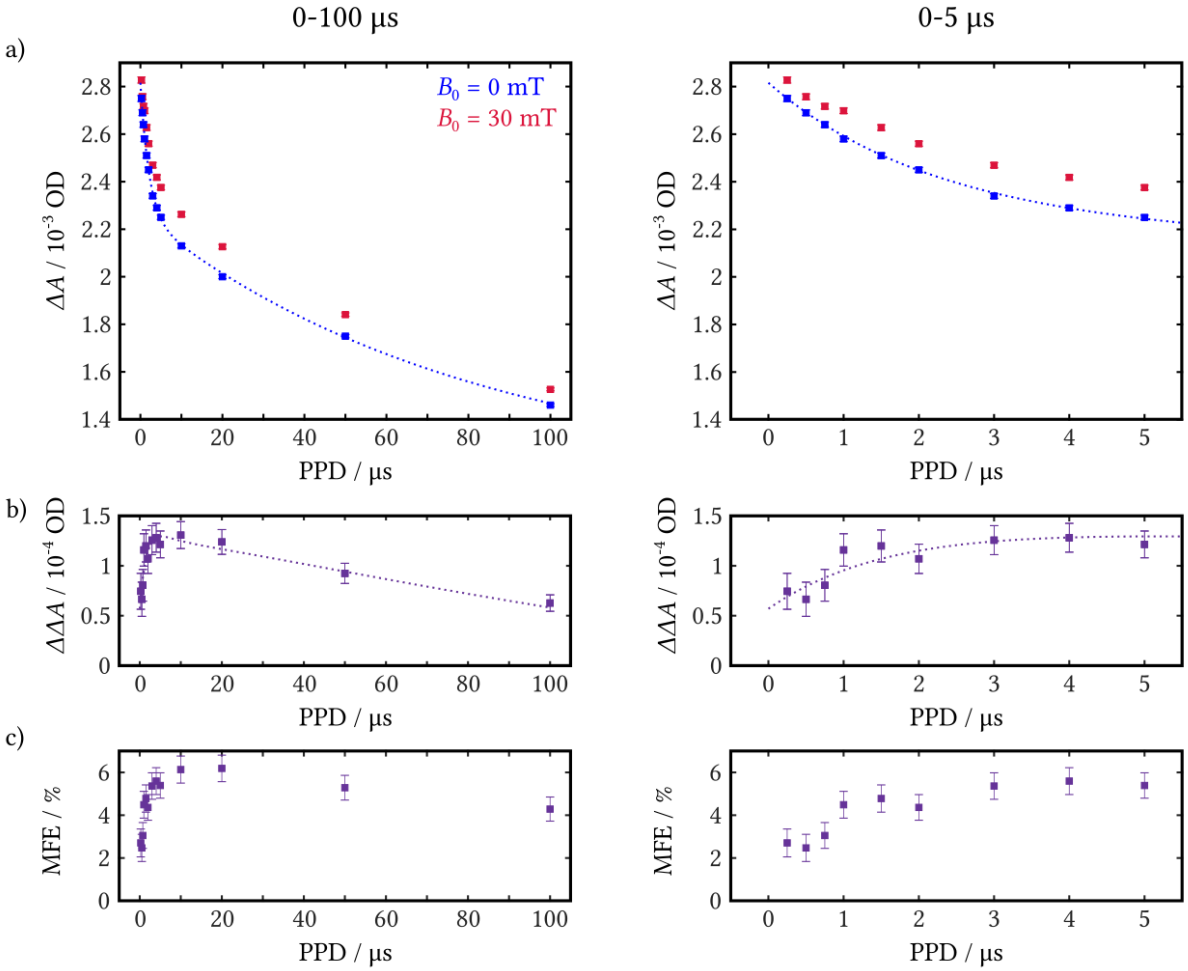


Figure 3.3: CRDS results for a time-resolved measurement on FMN (10 µM) and HEWL (500 µM) in water measured at 530 nm – corresponding mostly to $FMNH^{\bullet}$ (see Fig. 3.2 a) – following photoexcitation at 450 nm (300 µJ). Error bars represent the standard error of the mean of 200 measurements at each time-point. The sample was flowed at approx. 0.25 ml min^{-1} at 20 °C. The right panels show the horizontally expanded early pump-probe delay times (PPDs) from the left panels on the same vertical scale. a) ΔA in the presence (red) and absence (blue) of a 30 mT magnetic field at various PPDs. b) $\Delta\Delta A$, which is the subtraction of the field "off" data from the field "on" data in a). c) The percentage magnetic field effect.

The ΔA traces – showing the change in absorbance relative to the non-photoexcited state – show a fast decay component, which is attributed to the geminate radical pair recombination and triplet flavin decay,[3] and a long-lived decay, attributed to the diffusing species and their subsequent return to the ground state [123]. The data were fitted to a bi-exponential with time constants of $2.1 \pm 0.1\,\mu s$ and $80 \pm 8\,\mu s$ in the "off" measurements. The former is in agreement with Sheppard, while the long timescale value presented here is smaller than Sheppard's 100 µs time constant as a result of the longer PPDs used in this work which provide greater temporal information [127].[4]

The effect of the 30 mT field on the radical pair system is most clearly seen in Fig. 3.3 b), which shows the value of $\Delta\Delta A \equiv \Delta A_B - \Delta A_{B=0}$. The effect is seen to grow and peaks approximately 4 µs after photoexcitation before decaying, which is in good agreement with Maeda *et al.* [123]. The same can be seen in the magnetic field effect (MFE), shown in Fig. 3.3 c), the magnitude of which is in good agreement with Sheppard [127].

3.2.2 MARY Measurement of FMN/HEWL

Fig. 3.4 shows the MARY curve for the FMN/HEWL system measured again at a probe wavelength of 530 nm, 2 µs after photoexcitation. The increase in MFE is evident as the T_+ and T_- levels become more energetically isolated from the S/T_0 manifold, making the likelihood of the radical pair remaining in the triplet state higher, thus increasing the chance of formation of RP2. The freely diffusing radicals return to the ground state much more slowly than through the geminate case and, therefore, dominate the signal measured here, especially as the field increases. This, therefore, yields a positive MFE since the measurement at 530 nm corresponds to the radical absorbance and, by extension, concentration.

The MFE appears to be close to saturation at 30 mT and fitting the trace to a Lorentzian yielded a $B_{1/2}$ of 7.3 ± 0.5 mT, both of which are in good agreement with Sheppard, as is the approximately 5 % magnetic field effect at 30 mT [127]. The $B_{1/2}$ value is much larger than the Weller-predicted 3 mT value for a flavin-tryptophan radical pair and is a result of both the slow dynamics of the system and the involvement of dephasing; this dephasing is enhanced by the multiple re-encounters likely to occur as a result of the slow diffusion of HEWL and the Coulombic interaction between the two radical partners [59, 123, 129].

[3] The triplet flavin decay is a result of the photoexcited flavin molecules that have undergone intersystem crossing but have not formed a radical pair, which would happen prior to the earliest measurement possible by CRDS at 250 ns.

[4] Sheppard only recorded the time-resolved measurement up to 20 µs, in contrast to the 100 µs performed here.

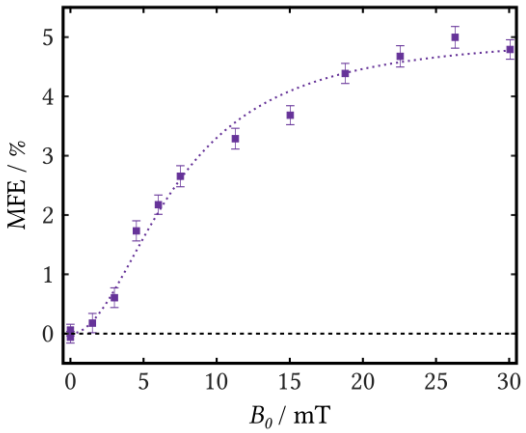


Figure 3.4: The MARY curve for FMN (10 µM) and HEWL (500 µM) in water measured at 530 nm, 2 µs after photoexcitation at 450 nm (300 µJ). With the energetic separation of the S/T_0 and T_+/T_- manifolds with increasing field, there is an increase in the radical concentration (compared to the zero-field case) due to the reduced ability to convert to the singlet state. This effect begins to saturate at high fields. The data is fitted to a Lorentzian (dashed line), from which the characteristic $B_{1/2}$-value can be obtained as 7.3 ± 0.5 mT. Error bars represent the standard error of the mean of 400 measurements at each field point. The sample was flowed at approx. 0.25 ml min^{-1} at 20 °C.

3.2.3 Time- and Wavelength-resolved Measurement of FMN/HEWL

Repeating the time-resolved experiment at a variety of wavelengths allows for a better understanding of the chemical species involved in the processes being observed. For FMN/HEWL the two particular species of interest are the radical absorption and the triplet state, which are evident at 500–600 nm and at wavelengths > 620 nm, respectively [130, 131]. This can be seen by considering the absorption spectra for the individual transient species in Fig. 3.2 a):

- the long-wavelength (>620 nm) region is dominated by ^{3}FMN*, which also exhibits absorption across the region measured,
- FMNH$^\bullet$ and TrpH$^{\bullet+}$ show absorption over a wider range of wavelengths, 500–625 nm, and
- FMN$^{\bullet-}$ is most likely absent as a result of the rapid protonation (faster than 250 ns) following electron transfer [131].

Fig. 3.5 a) shows the time- and wavelength-resolved spectra for FMN/HEWL in the absence of an applied magnetic field.[5] As performed by Sheppard, measurements are run with 20 nm steps from 500 nm to 700 nm. It is evident that the triplet state decays rapidly, particularly noticeable at longer wavelengths (620–700 nm), while the radical region (500–600 nm) shows

[5]These spectra were obtained using a sample that included HEWL that was not stored correctly. The effects of this are explored in Section 3.2.4.

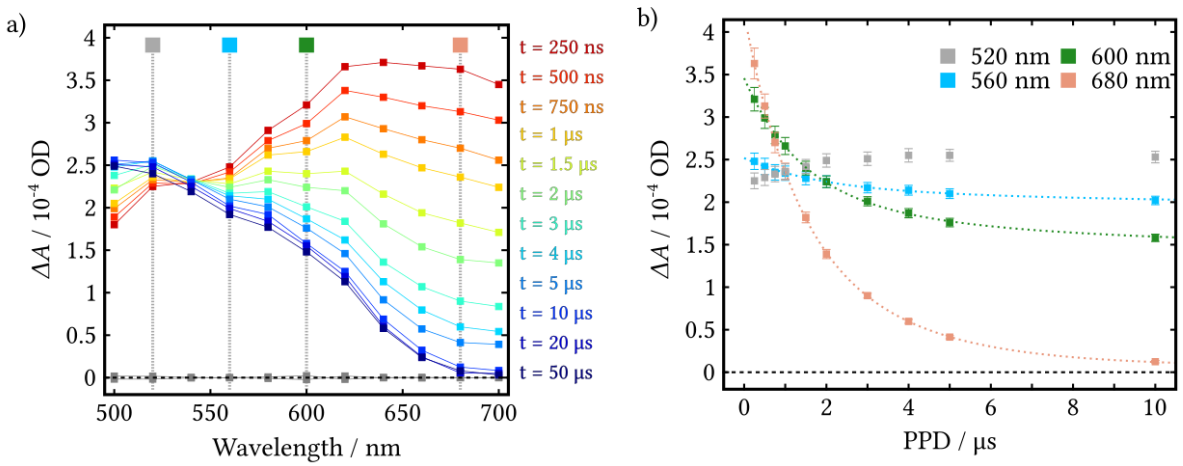


Figure 3.5: The time- and wavelength-resolved spectra of FMN (10 µM) and HEWL (500 µM) in water following photoexcitation at 450 nm (300 µJ). Error bars represent one standard error of the mean of 20 measurements. The sample was flowed at approx. 0.25 ml min^{-1} at 20 °C. a) The wavelength-resolved spectra (with wavelength steps of 20 nm). The spectra are coloured based on pump-probe delay time ranging from 250 ns (red) to 50 µs (blue). The time evolution of the signals at four wavelengths of interest which are shown in b) and are marked with grey vertical lines. b) Extraction of the time-resolved spectra from a) at 520 nm (grey), 560 nm (blue), 600 nm (green), and 680 nm (orange). The data of the latter three wavelengths are fit to a bi-exponential model (dashed lines) with fast components of 1.86 ± 0.41 µs at 560 nm, 1.34 ± 0.20 µs at 600 nm, and 1.14 ± 0.18 µs at 680 nm. The bi-exponential fitting parameters are shown in Table 3.1.

far less of a decay over the timescale of the measurements. A small amount of the ground state bleach is evident at 500–520 nm, evidenced by the rise in absorption which most likely corresponds to the ^{3}FMN* ⟶ FMN transition.

Four wavelengths of interest, indicated by vertical grey lines, are extracted and shown in Fig. 3.5 b), three of which are fit to bi-exponentials for which the fast time constants are:[6] 1.86 ± 0.41 µs at 560 nm, 1.34 ± 0.20 µs at 600 nm, and 1.14 ± 0.18 µs at 680 nm. These are, once again, in agreement with Sheppard [127]. The fitting parameters for the bi-exponential fits are given in Table 3.1.

3.2.4 The Importance of Sample Freshness

An interesting observation in comparing the data in Fig. 3.5 a) with that obtained by Sheppard, which are in good qualitative agreement, is the slight bathochromic shift of approximately 5–10 nm, particularly noticeable in the data at 540 nm. Consideration of the trace at 520 nm, extracted in grey in Fig. 3.5 b), (and the less prominent data at 540 nm) revealed a potential

[6]The fourth wavelength of interest, 520 nm, will be discussed further in Section 3.2.4.

Wavelength / nm	560	600	680
y_0 / 10^{-4} OD	1.92 ± 0.03	1.50 ± 0.02	0.0684 ± 0.0098
A_1 / 10^{-4} OD	0.384 ± 0.054	1.33 ± 0.22	2.12 ± 0.66
t_1 / µs	1.86 ± 0.41	1.34 ± 0.20	1.14 ± 0.18
A_2 / 10^{-4} OD	0.214 ± 0.050	0.627 ± 0.227	2.03 ± 0.67
t_2 / µs	15.8 ± 8.4	5.28 ± 1.70	2.71 ± 0.41

Table 3.1: Table showing the bi-exponential fitting parameters for fits of the time evolution of the signal at three wavelengths in the time- and wavelength-resolved FMN/HEWL measurement, shown in Fig. 3.5 b).

discrepancy with what is seen in the time-resolved measurement shown above in Fig. 3.3:[7] the value of ΔA appears to increase first, rather than showing a pure exponential decay.

This phenomenon was further investigated by performing a time-resolved measurement, again at 530 nm (in order to compare it to the time-resolved data shown in Fig. 3.3). The results from this measurement are shown in Fig. 3.6 and show an initial rise in ΔA – in contradiction to the time-resolved measurement shown in Fig. 3.3. Both the $\Delta\Delta A$ and ΔA values are larger than those seen in Fig. 3.3, leading to a magnetic field effect that is in good agreement between the two measurements shown in this work. It is evident, however, that the initial rise in ΔA becomes more pronounced with time, evidenced by consideration of the just the first five averages (Fig. 3.6 d) which show a much smaller rise.

Following many checks of the spectrometer, the sample was checked by purchasing new components from Sigma Aldrich and performing the measurement again. This was found to return the same results as seen originally (Fig. 3.3) and by previous investigators [123, 127]. It was found that the HEWL that showed the peculiar behaviour seen in Fig. 3.6 had been stored at 4 °C, rather than at −20 °C as advised by the data sheet.[8] This higher temperature during storage may have resulted in denaturation of the protein, altering its secondary structure and folding the surface-exposed tryptophan residues into less accessible positions for electron transfer, which may also have been a result of oligomerisation.

[7] It should be noted that, due to the 20 nm steps in the time- and wavelength-resolved measurement, a direct comparison is not possible between the data at 540 nm shown in Fig. 3.5 and that from the time-resolved measurement in Fig. 3.3.

[8] The HEWL used in the time-resolved and MARY experiments in this chapter (Figs 3.3 and 3.4) was stored at −20 °C; it was only the HEWL used for the time- and wavelength-resolved experiment and the further investigations that was stored at 4 °C.

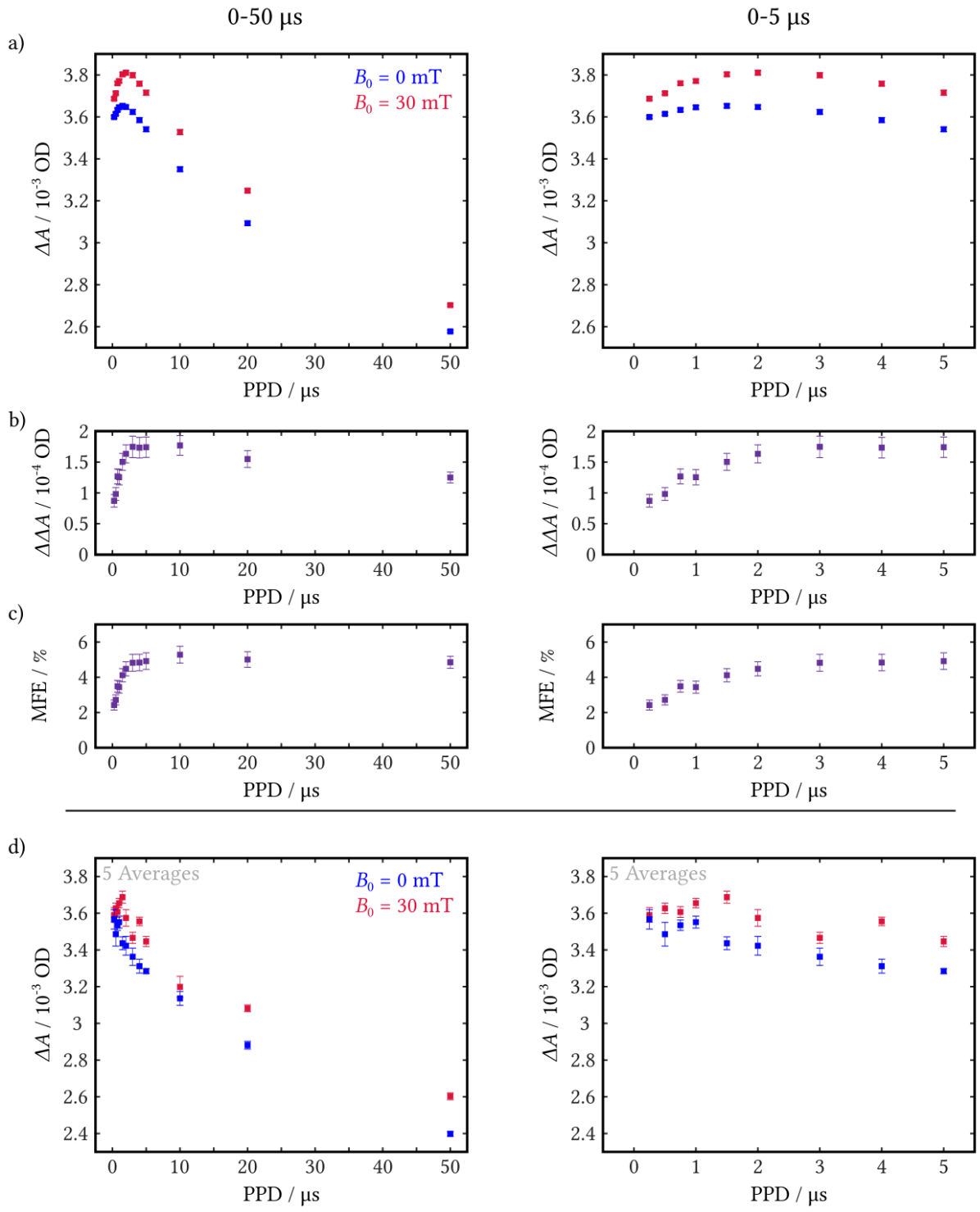


Figure 3.6: CRDS results for a time-resolved measurement on FMN (10 µM) and *incorrectly stored* HEWL (500 µM; further information in the text) in water measured at 530 nm following photoexcitation at 450 nm (300 µJ). Error bars represent the standard error of the mean of 250 measurements at each time-point. The sample was flowed at approx. 0.25 ml min^{-1} at 20 °C. The right panels show the horizontally expanded early pump-probe delay times (PPDs) from the left panels on the same scale. a) ΔA in the presence (red) and absence (blue) of a 30 mT magnetic field at various PPDs. b) $\Delta\Delta A$, which is the subtraction of the field "off" data from the field "on" data in a). c) The percentage magnetic field effect. d) ΔA in the presence (red) and absence (blue) of a 30 mT magnetic field showing only the first five averages of the data presented in panel a).

This structural change could explain too why the concentration of the radicals increases over the first 2 µs. Immediately following photoexcitation, only a fraction of the excited flavin molecules can undergo the electron transfer process to produce the radical pair due to many of the tryptophan residues being inaccessible as a result of the change in the protein's secondary structure. As structural fluctuations in the HEWL protein allow greater surface access of the tryptophan residues, more electron transfers can occur to the excited state flavin, increasing the concentration of the radical pairs – which is the predominant species being measured by detection at 530 nm. The concentration of the excited flavin state, however, is rapidly decaying, losing more than 80 % of its initial intensity over the first 5 µs, evidenced by the decay of the signal at 680 nm in Fig. 3.5.

3.3 Power-dependence of ΔA

CRDS, unlike some other optical techniques, does not require the initial probe beam power to be measured in order to determine the absorbance or change thereof (as discussed in Section 2.2.1). In fact, the incident power is irrelevant in the ringing of the optical cavity and simply needs to be sufficient to be detected after several round trips. Given that the ring-down of the cavity following photoexcitation depends on the concentration of absorbers, the natural fluctuation in pump laser power will also result in a change in the concentration and, therefore, the ring-down time.

A significant component of the new CRDS design was the facility to monitor the pump laser's power throughout an experiment. In order to ensure this capability, an additional detector was placed in the beam path of the pump laser. Experiments were conducted to assess whether a greater signal-to-noise ratio could be achieved by correcting for the pump power. As this was a proof-of-principle study, the power intensity is not measured on the oscilloscope in absolute units, but is rather compared within the experiment. This is done by fitting the power profile acquired by the photodetector to a Gaussian function[9] and calculating the area under the fitted curve, yielding the energy of each pulse. The mean pulse energy is 300 µJ, measured at the start and end of the experiment using an external power meter, and this suggests that fluctuations in this energy are approximately 30 µJ.[10]

There is a natural fluctuation in the ring-down time, τ, even in a cavity with no absorber or cell, as can be seen by the vertical spread in Fig. 3.7 a), which shows the difference of each τ-value from the mean τ-value for the experiment, *viz.* $\Delta\tau = \tau_i - \overline{\tau}$. This fluctuation is, however,

[9] The pump power traces take the form of a Gaussian which was fit in MATLAB using the *Gauss1* model. The peak intensity and centre parameters were bound at 2.5 % from the maximum value in the trace, while all other parameters were allowed to vary freely.

[10] The fluctuation of 30 µJ assumes a ±10 % change in the output power from the dye laser, which is in good agreement with that seen by Ityaksov, as well as seen in measurements shown in this section [132].

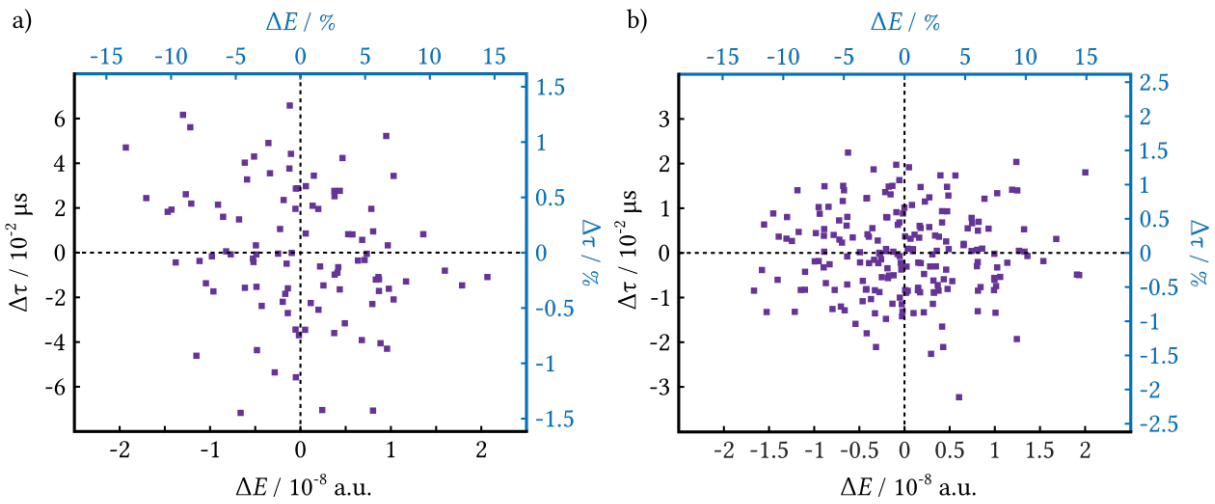


Figure 3.7: Figure showing the deviation of the ring-down time, τ, and the pump pulse energy (in arbitrary units; see text for further explanation), E, from their mean values for a) an empty cavity, and b) a cavity with a sample cell filled with water. The right and top axes show the percentage changes from the mean values.

small – of the order of 1 % – and is most likely a result of the resolution of the photodetector or, in some cases, scatterers passing through the beam path. This is in stark contrast to the 10 % fluctuation in the pump pulse energy, which is presented in the same way as τ in the horizontal direction. Performing the same experiment with a sample that does not absorb at 450 nm, in this case water, shows the same fluctuations and is on par with the empty cavity, meaning that the cell itself is not introducing additional noise. This water measurement is shown in Fig. 3.7 b).

Extending this further to include FMN/HEWL as the absorber shows a small increase in the fluctuation to the ring-down time to approximately 2 % when static and 5 % when flowed – this is expected as the flow causes some motion in the solution that may result in greater scattering or motion of the cell, as well as fluctuations in the pump speed. Additional factors that may lead to this increased noise include the presence of (micro)bubbles, aggregates and precipitates, although these latter two are more common in protein samples and samples that have a high viscosity. This increase in $\Delta\tau$ can be seen as the vertical spread of the points in Fig. 3.8 which shows the results from the static (a) and flowed (b) sample.

Considering now the relationship between the measured parameters for the static sample, shown in Fig. 3.8 a), there is a clear trend, as expected, of τ decreasing with increasing pulse energy – understood by recognising that there is a higher radical concentration with greater photoexcitation which leads to greater absorbance, i.e. a shorter ring-down time (see Eqn 2.13). This is reduced, but nevertheless still evident, in the flowed data, which also shows many more outliers as a result of scattering and turbulence in the cell.

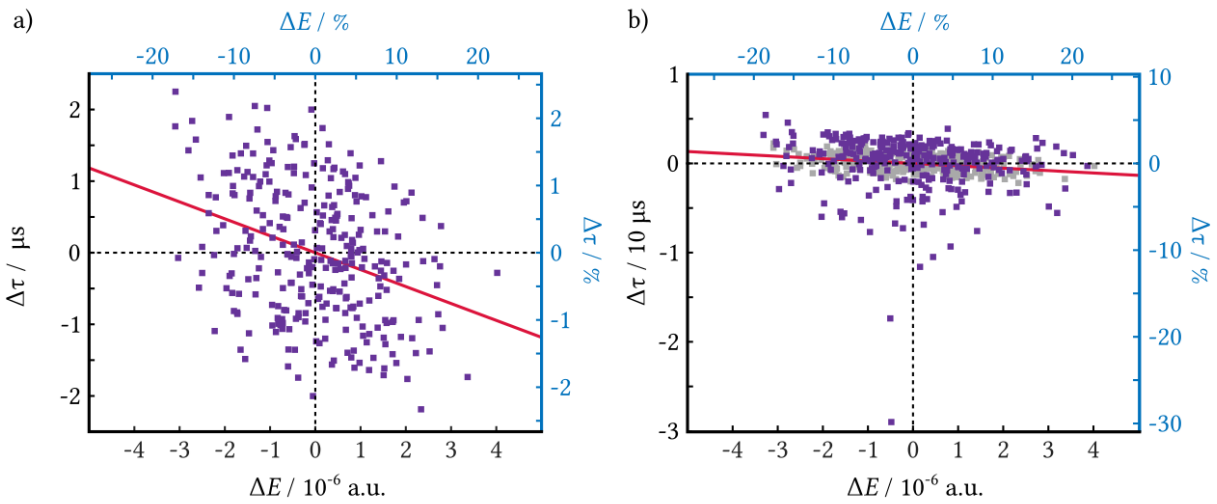


Figure 3.8: Figure showing the deviation of the ring-down time, τ, and the energy (in arbitrary units; see text for further explanation), E, from their mean values for a solution of FMN (10 µM) and HEWL (500 µM) in water for a a) static and b) flowed sample (at a rate of 0.25 ml min^{-1}). The static data from a) are shown in grey in b) for comparison. The right and top axes show the percentage changes from the mean values.

Fitting the data from the static sample to a linear model shows a negative gradient of −0.24±0.04 and a regression coefficient of $R^2 = 0.11$, suggesting that the data are not highly correlated. The flowed sample had a gradient of −0.27 ± 0.13 and a regression coefficient of $R^2 = 0.01$, i.e. there is no correlation. The fits for both samples are shown in Fig. 3.8. The fitting of the static data suggests that, while there is a fluctuation as a result of the changing pump power, this is not the greatest contributor to the noise seen in the ring-down time and its continual monitoring during experiments would not prove helpful in increasing the signal-to-noise ratio. As such, no monitoring of the pump laser power is employed in the further measurements performed in this work.

3.4 Conclusions

This chapter has shown test measurements on the rebuilt CRD spectrometer, which are in good agreement with those reported previously. The sensitivity of the instrument is particularly evident in being able to see the bathochromic shift in the time- and wavelength-resolved experiment. As a result of these findings, it is important to ensure that HEWL used in magnetic field effect experiments should be stored at −20 °C and it may also be worth exploring whether the sample should be kept cool (much like the cryptochromes measured in this work) during measurement.

Chapter 4

CRDS Measurements on Cryptochromes

4.1 Background

Since their implication in magnetosensitivity, cryptochromes – along with the closely related photolyases – have shown magnetic field effects (MFEs) by a variety of techniques, not least CRDS. Such MFEs have been shown on: *E. coli* photolyase (*Ec*PL), *Arabidopsis thaliana* cryptochrome 1 (*At*Cry1), *Drosophila melanogaster* cryptochrome (*Dm*Cry), and *Xenopus laevis* cryptochrome-DASH (*Xl*Cry) [60, 104, 133].

Cryptochromes are blue-light photoreceptor proteins that share large portions of sequence identity with photolyases [89]. In contrast to photolyases, though, cryptochromes do not have any DNA repair activity [134]. In the role of magnetoreception, this activation is hypothesised to occur through the vitamin-derived FAD cofactor that is non-covalently bound to the protein. Following blue-light photoexcitation, which excites the flavin to its excited singlet state ($^1F \longrightarrow {}^1F^*$), there is a rapid reduction to form the flavosemiquinone radical ($F^{\bullet -}$), mediated by electron transfer along a conserved tetrad (or triad) of tryptophan residues (Fig. 4.1 a) [35, 100]. This photoreduction forms the radical pair ($^1[F^{\bullet -}TrpH^{\bullet +}]$) in the singlet state – due to conservation of spin angular momentum and the rate of electron transfer, which is faster than intersystem crossing – which can then undergo coherent singlet-triplet mixing. As a result of spin conservation, only the radical pair in the singlet state can recombine to return to the ground state, while the triplet state has one of two options: either interconvert back to the singlet to recombine back to the ground state, or form a secondary radical pair (RP2) by protonation, which can then lose its spin coherence and return to the ground state [100, 133]. These photoprocesses are shown in Fig. 4.1 b).

In this work, three avian species are considered: the European robin (*Erithacus rubecula*), the common pigeon (*Columba livia*), and the chicken (*Gallus gallus*). The robin is a well-known

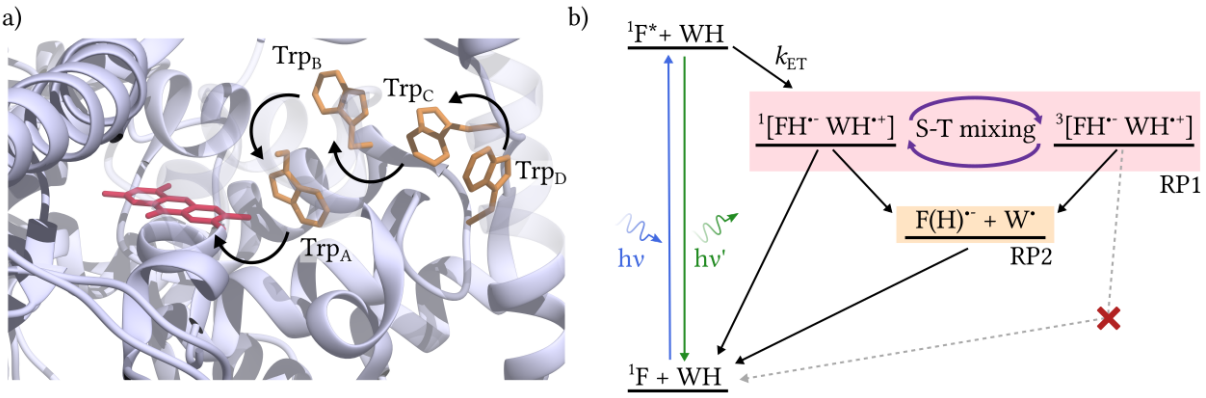


Figure 4.1: a) The active site for the proposed radical pair formation in cryptochrome, here shown in cryptochrome from *Drosophila melanogaster* (*Dm*Cry, PDB: 4GU5) showing the flavin cofactor (red) [98]. In the avian cryptochromes considered in this work, the conserved tetrad of tryptophan residues (orange) comprises W395, W372, W318 and W369 – often labelled Trp_A to Trp_D – in order of their electron transfer position in the cascade to form the radical pair. b) Photoscheme for cryptochromes. The flavin cofactor is photoexcited by blue light before being rapidly reduced to form the flavosemiquinone radical by electron transfer along the tryptophan tetrad (or triad in the case of W369F mutants). This forms the radical pair (RP1) in the singlet state due to spin conservation, which can undergo coherent singlet-triplet mixing. Only the singlet state can recombine back to the ground state (the inability of the triplet to do so is indicated by the red cross on the dashed grey line). Protonation or deprotonation of one or both of the radical partners can lead to a second long-lived radical pair (RP2), which can lose spin coherence and return to the ground state.

migrator, flying south from Britain to southern Europe,[1] while the other two species do not migrate, although pigeons are also known to orient with the magnetic field [67]. In spite of this difference, the three species are somewhat phylogenetically similar, having a common ancestor approximately 90 million years ago, after which the branch that contains chickens split from the other two; the same split for the European robin and pigeon occurred approximately 70 million years ago. This can be seen in the phylogenetic tree shown in Fig. 4.2 [135].

Considering now specifically cryptochrome 4 – the cryptochrome that is believed to be the magnetoreceptor under the hypothesis[2] – across the three species, there is good sequence conservation (shown in green in Fig. 4.3), despite the early branch point in the phylogeny. Of particular importance in these sequences is the conserved tryptophan tetrad, comprising W395, W372, W318 and W369 – often labelled Trp_A, Trp_B, Trp_C, and Trp_D, respectively – which are involved in the electron transfer cascade that leads to the radical pair (shown in orange in Fig. 4.1 b).

[1] Robins usually found in Russia and Scandinavia migrate to western Europe.

[2] There are some discussions around the use of Cryptochrome 1a (Cry1a) as the potential magnetoreceptor, mostly related to a conformational change upon photoexcitation [136]. However, Cry1a and 1b show no alteration in their expression quantities between the migratory and non-migratory season and show a clear circadian oscillation, unlike Cry4, as well as failing to bind the flavin cofactor (at least in *Cl*Cry1a) [99, 100, 137].

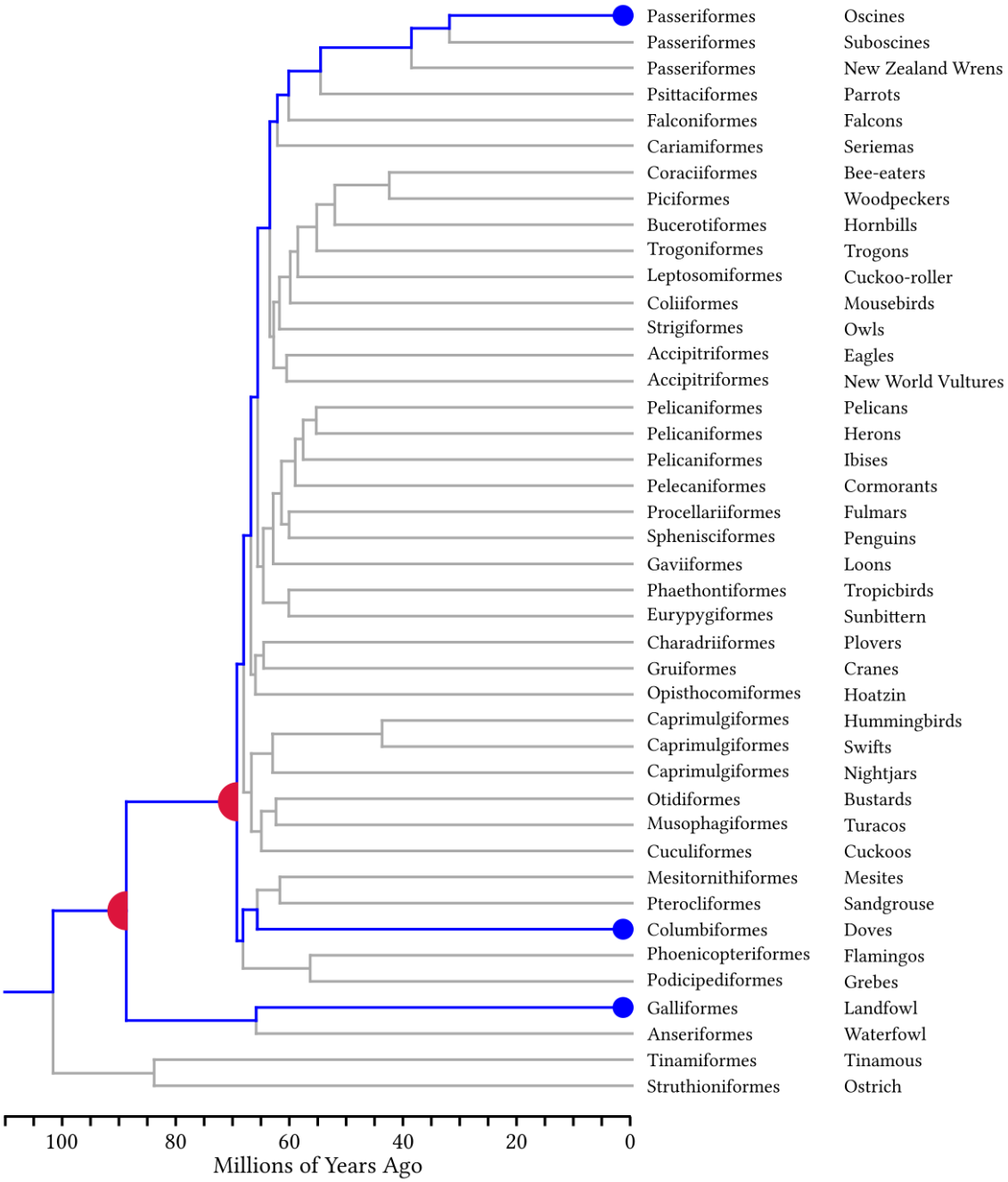


Figure 4.2: Phylogenetic tree based on that presented by Jarvis *et al.* [135]. The evolutionary paths taken by the three species considered in this work are highlighted in blue and the branching points marked with a red semicircle. The three species highlighted in the figure (including their path) and their respective orders are: *Erithacus rubecula* – Passeriformes; *Columba livia* – Columbiformes; and *Gallus gallus* – Galliformes. The English group terms are included alongside the order names.

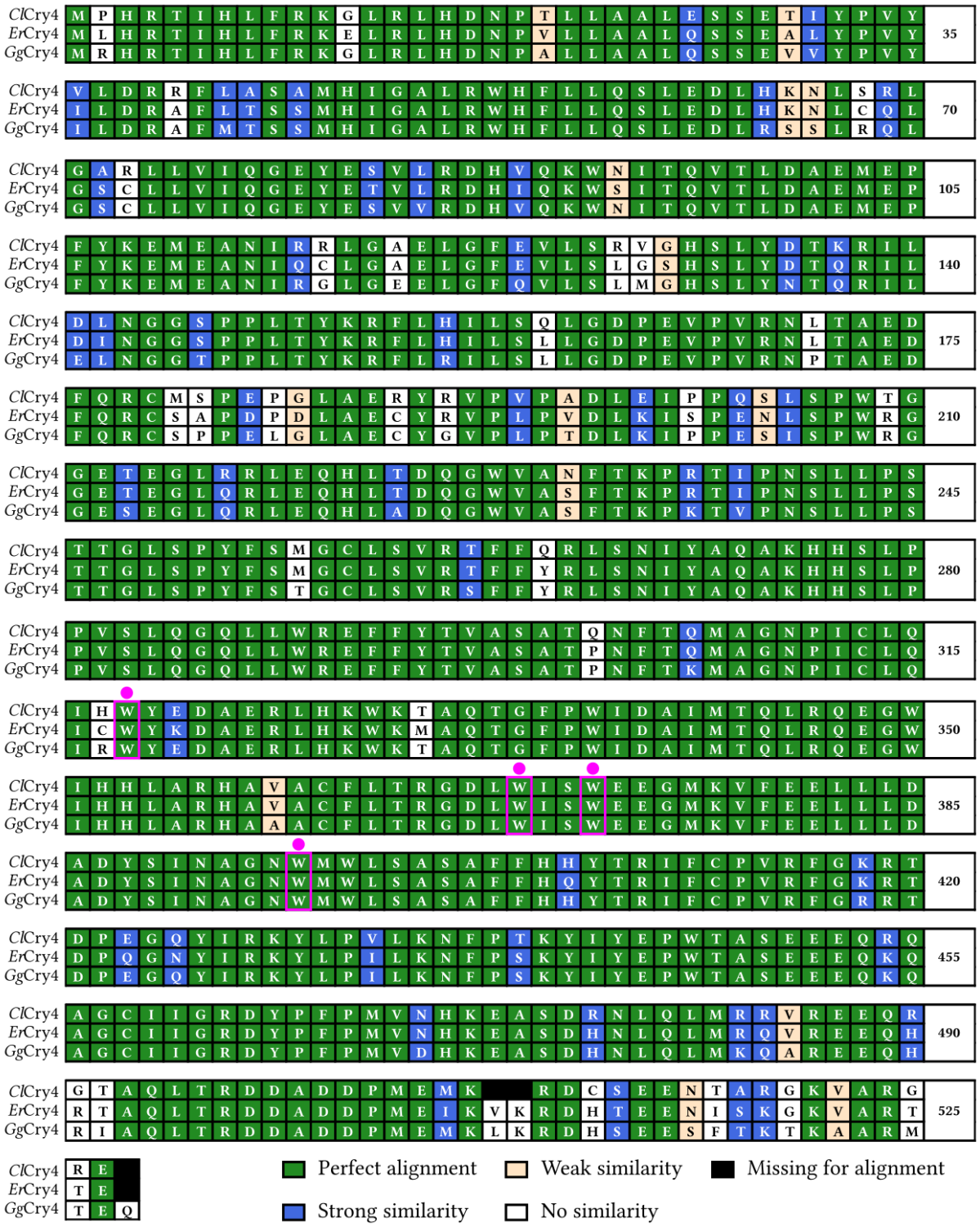


Figure 4.3: Figure showing the alignment of the sequences of cryptochrome 4 from pigeon (*Columba livia*, *Cl*Cry4 – top line), the European robin (*Erithacus rubecula*, *Er*Cry4 – middle line), and chicken (*Gallus gallus*, *Gg*Cry4 – bottom line). A legend for the colour code is provided at the bottom of the figure based on the markers provided by the alignment program *Clustal* [138]. The conserved tetrad of tryptophan residues at positions 318, 369, 372, and 395 – involved in the electron transfer cascade – are marked with a pink box and circle above the residues.

While there is such close alignment between these three cryptochromes, crystal structures have not been solved for all of them, with only the structure of *Cl*Cry4 having been determined to date [107]. It is, therefore, unknown what evolutionary differences in structure are present, if any, that may lead to differential roles of these receptors in the various species.

Measurements presented in this chapter were performed on both the wild type proteins and W369F mutants – where the terminal tryptophan (W369, Trp_D) is mutated to a phenylalanine, which is unable to take part in the electron transfer process. A large amount of this work contributed either directly or indirectly to a significant part of a publication in *Nature* [100].

4.2 Cryptochrome Synthesis and Preparation

4.2.1 Cryptochrome Expression and Purification

Samples for this work were kindly prepared by Jingjing Xu, Jessica Schmidt, Rabea Bartölke, and Marco Bassetto at Carl-von-Ossietzky Universität Oldenburg (Germany) – for which the author is grateful – and their procedure is outlined here.

The full-length cDNA sequence (*Er*Cry4, GenBank: KX890129.1; *Gg*Cry4, GenBank: AY102068; *Cl*Cry4, GenBank: KX168611) was cloned into an expression vector and site-specific mutagenesis performed (in the case of the mutated cryptochrome samples measured). A polymerase chain reaction was undertaken to amplify the expression construct. This construct was then transferred to BL21(DE3)-competent *E. coli* cells and cultured overnight. Monoclonal colonies were harvested and recultured as starters. These starters were incubated before being moved to an expansion medium. Following further incubation, the optical density at 600 nm (OD_{600}) was measured. If $OD_{600} < 0.5$, the culture was left to continue incubating, while the culture was cooled to 15 °C if $OD_{600} \approx 0.6$. Upon reaching 15 °C, isopropyl-D-1-thiogalactopyranoside (IPTG) was added and the sample reincubated at the same temperature. Following incubation, the culture was harvested by centrifugation and the cell pellet resuspended with Ni-binding buffer, after which the sample was recentrifuged and the cell pellet stored at −20 °C for later processing.

When ready for further processing, the pellets were thawed in a room-temperature bath before being resuspended in Ni-binding buffer, along with a protease inhibitor to prevent degradation. The cell suspensions were then lysed using an ultrasonic homogeniser in an ice bath; the lysis mode (4 s on/8 s off) was chosen also to prevent heating the samples. The lysed suspension was fractioned by centrifugation and the supernatant retained. A purification routine was then applied involving both nickel affinity (based on the His-tags used in expression) and anion exchange chromatography (based on the protein's surface charge). The buffers (10 mM Tris, pH ≈ 8, 250 mM NaCl, 20 % glycerol v/v) had 10 mM 2-mercaptoethanol added in order

to prevent protein dimerisation. Following elution from the anion exchange chromatograph, the protein was concentrated and glycerol was added up to 20 % v/v. Aliquots of 100–200 µl were then shock-frozen in liquid nitrogen and stored at −80 °C. The aliquots were shipped on dry ice and either used immediately or stored at −80 °C until required for spectroscopic measurements.

Further details can be found in Xu *et al.* and Qin *et al.* [100, 139].

4.2.2 Sample Preparation

Following shipping of the samples on dry ice, the samples were either stored at −80 °C or used immediately. They were first thawed on (water-)ice before being buffer-exchanged (by centrifugation) to remove the 2-mercaptoethanol that was used to prevent dimerisation. If the sample showed signs of reduced flavin forms (typically seen by the doublet peak centred at approximately 600 nm ($FADH^{\bullet}$) or by the peak with shoulder centred around 370 nm (either $FADH^{-}$ or $FAD^{\bullet -}$), which are evident in Fig. 4.4 a), the sample was reoxidised by addition of 50 µM $K_3Fe(CN)_6$ and left on ice until fully oxidised.

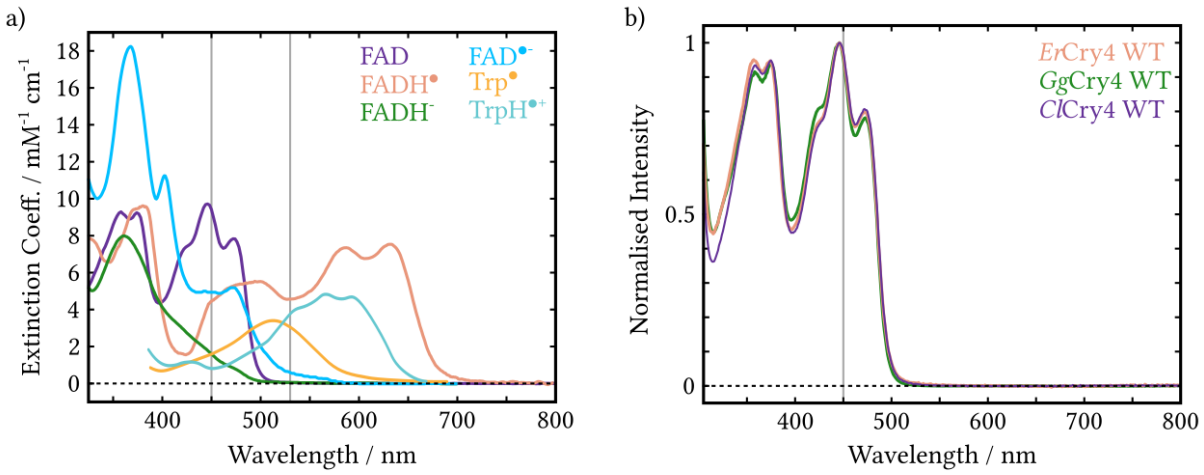


Figure 4.4: a) UV-vis spectra of the radical species of interest in cryptochromes. The spectra for the oxidation states of FAD, as determined from FAD bound in cryptochrome 1 of a mosquito (*Ag*Cry1), and the tryptophanyl radicals are taken from the literature [140–142]. The samples in this work are photoexcited at 450 nm and ring-down traces recorded at 530 nm, both indicated by the grey vertical lines. b) UV-vis spectra of the fully oxidised wild type cryptochrome proteins measured in this work, normalised to their maximum value in the peak around 450 nm. The wavelength at which photoexcitation occurs (450 nm) in all experiments is shown by a grey line.

Following reoxidation, the $K_3Fe(CN)_6$ was removed and the sample concentrated to obtain a 200 µl sample of absorption 0.6 OD at 450 nm (approximately 60 µM). The buffer (10 mM Tris, pH ≈ 8, 250 mM NaCl, 20 % glycerol v/v) then had $K_3Fe(CN)_6$ added up to a concentration of 5 mM before being centrifuged for at least 1 h at 4 °C. Following centrifugation, the supernatant was carefully removed by pipetting to prevent disturbance of any polymerised protein at the base of the PCR tube and placed into the cuvette, already cooled to 5 °C in the spectrometer.

The UV-vis spectra for the three wild type cryptochromes used in this work are shown in Fig. 4.4 b). All three show the characteristic fully oxidised flavin peaks seen in panel a), as well as the vibrational structure around the 450 nm peak, which are characteristic of the flavin being bound within the protein [100].

Throughout this chapter it should be noted that this project sits on the forefront of cryptochrome research. As such, many of the sample expression and purification protocols, along with transportation mechanisms, were developed over the course of the project and, as a result, there may be some variability in the data acquired. Data that are not in this thesis were discarded after careful consideration and comparison with results obtained from other techniques, and the latter-stage data, where reproducibility was much improved, are shown here. The data presented in this work show robust reproducibility, even if minor differences remain in some experimental results.

4.3 Comparing the Avian Wild Type Cryptochromes

As performed in Chapter 3, time-resolved measurements were recorded with a probe wavelength of 530 nm – corresponding to the radical absorption of four species ($FAD^{\bullet}$, $FAD^{\bullet-}$, $Trp^{\bullet}$and $TrpH^{\bullet+}$), as can be seen in Fig. 4.4 – at certain times following photoexcitation at 450 nm (with pulse energy of 300 µJ).

Following the work of Zollitsch, the first cryptochrome measured was the wild type of the migratory European robin, *Erithacus rubecula* (*Er*Cry WT) [108]. This was even more important than previously expected as the *Er*Cry WT sample measured by Zollitsch contained minor sequence errors at the C-terminus tail [100, 108]. Fig. 4.5, therefore, shows the first time-resolved measurement on cryptochrome 4 from a migratory bird. The field "off" data are fit to three different functions to assess the most appropriate model for use. These models are: mono-exponential with offset, bi-exponential without offset, and bi-exponential with offset, shown in Fig. 4.5 a), b), and c), respectively. The offset contributes to the presence of a photogenerated species with lifetime exceeding the measurement. Although the parameters for the bi-exponential fit with offset seem excessive, they simply improve the fitting. The fitting parameters are shown in Table 4.1.

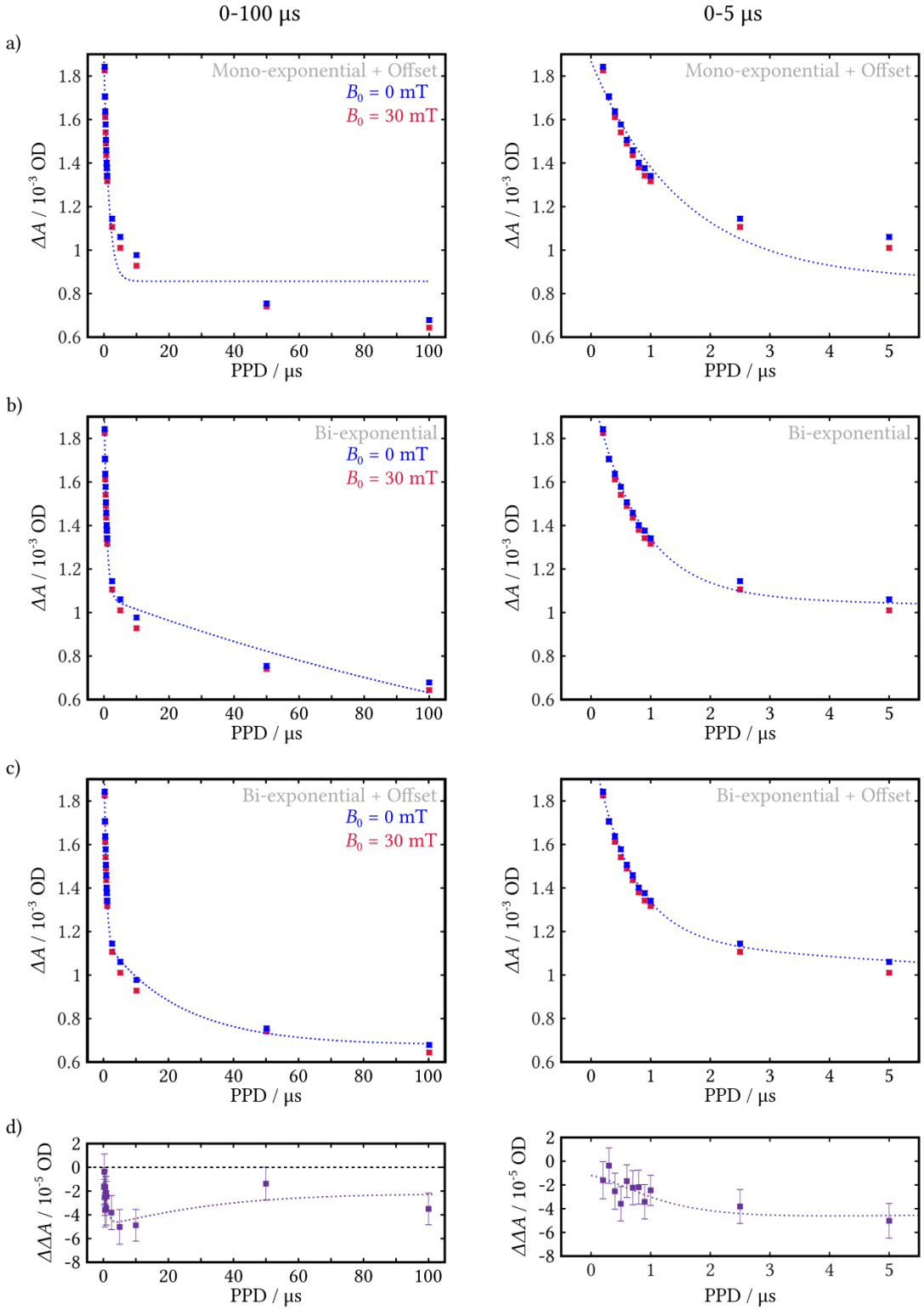


Figure 4.5: CRDS results for a time-resolved measurement on *Er*Cry WT measured at 530 nm following photoexcitation at 450 nm (300 µJ). Error bars represent the standard error of the mean of 200 measurements at each time-point. The dashed lines show the various fits (described in grey) to the zero-field ΔA trace (blue) – a) mono-exponential with offset, b) bi-exponential without offset, and c) bi-exponential with offset. The field "on" (30 mT) traces are shown in red. The right panels show the horizontally expanded early pump-probe delay times (PPDs) from the left panels on the same vertical scale. d) $\Delta\Delta A$, which is the subtraction of the field "off" data from the field "on" data. The fit is the subtraction of the bi-exponential with offset fits to the ΔA data.

***Er*Cry WT**			
Parameter	Mono + Offset	Bi	Bi + Offset
y_0 / 10^{-3} OD	0.857 ± 0.053	–	0.684 ± 0.016
A_1 / 10^{-3} OD	1.01 ± 0.10	0.962 ± 0.050	0.908 ± 0.025
t_1 / µs	1.52 ± 0.40	0.800 ± 0.080	0.653 ± 0.037
A_2 / 10^{-3} OD	–	1.07 ± 0.03	0.476 ± 0.19
t_2 / µs	–	192 ± 22	22.9 ± 3.8
R^2	0.931	0.992	0.999

Table 4.1: Table showing the fitting parameters for the three exponential models, fit over the full range of pump-probe delay times, for the wild type cryptochrome 4 samples from *Erithacus rubecula* (*Er*Cry WT).

In all three cases it is clear that there is a short-lived component with decay constant of approximately 1 µs. The mono-exponential model fits this reasonably well, but is improved by adjustment to the bi-exponential model, which better accounts for the clearly evident long-lived component. The two bi-exponential models suggest that the amplitudes of the short- and long-lived components (A_1 and A_2, respectively) are approximately equal.

Considering Figs 4.5 a)–c), the application of a magnetic field (of strength 30 mT) lowers the concentration of radicals observed (i.e. the ΔA_{On} value is below ΔA_{Off}), as expected for a singlet-born radical pair. This is a result of the energetic separation of the S/T_0 and T_+/T_- manifolds through the Zeeman interaction, reducing the efficiency of singlet-triplet mixing. There is, therefore, a greater chance that the singlet-born radical pair can recombine to the ground state – not possible from the triplet state due to spin conservation – since it is less able to mix into the triplet state. The secondary radical pair, RP2, which is formed by deprotonation of the tryptophan or protonation of the flavin (or both), returns to the ground state over a much longer timescale as the radicals lose spin coherence, seen in the long-lived non-zero signal.

Consideration of $\Delta\Delta A$, shown in Fig. 4.5 d), shows an initial increase in the effect of a magnetic field over the first 5 µs, before it decays; the maximum MFE is approximately 2 %, in good agreement with Zollitsch [108]. The MFE is derived in RP1 which can undergo singlet-triplet mixing, and appears to take effect over approximately the first 5 µs; the effect of the magnetic field is evident throughout the timescale shown. The fit shown is the subtraction of the fit to the field "off" from that of the field "on" data, which shows satisfactory agreement.

Looking more closely at the region over which the $\Delta\Delta A$ increases in magnitude, it is evident that both the decay of ΔA and the growth of $\Delta\Delta A$ are on the same timescale, clearly evident in Fig. 4.6; the MFE is also plotted. The ΔA over the first 5 µs is fit to a mono-exponential with offset for which the decay (growth, for $\Delta\Delta A$ and MFE) constant is 1.23 µs, which is in reasonable agreement with those seen in the two bi-exponential models considered above. The data also agree with the decay seen by Zollitsch previously on the incorrect sequence, as well as that seen by picosecond-transient absorption spectroscopy [100, 108]. In both of these

previous reports, the approximately 1 µs decay constant is attributed to the deprotonation of $TrpH^{\bullet+}$. Xu *et al.* further suggest that the two rate constants for the fit to ΔA should be three orders of magnitude different from one another, suggesting that recombination should be the quicker process and the return to the ground state from radical pair 2 the slower one.

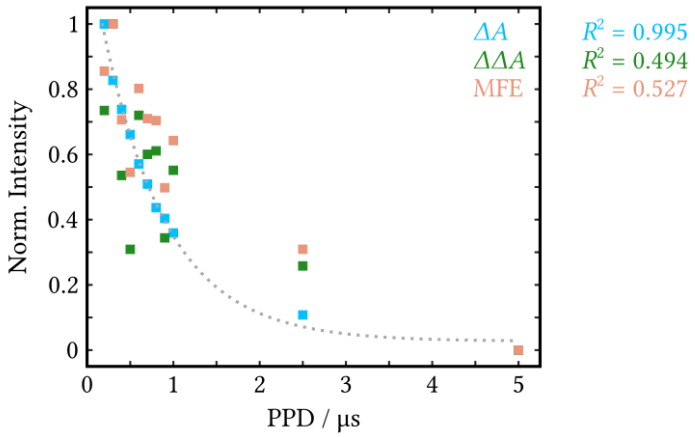


Figure 4.6: Normalised and baseline-corrected data from the time-resolved measurement on *Er*Cry WT showing the ΔA, $\Delta\Delta A$, and MFE. The ΔA data are fit to a mono-exponential with decay constant of 1.23 µs. The goodness of fit (R^2) for each dataset to the fit shown is provided alongside the figure.

Next, cryptochrome 4 from the migratory robin (*Er*Cry WT) is compared with that from the non-migratory chicken (*Gg*Cry WT), the result of the latter being shown in Fig. 4.7. The initial intensity of ΔA is approximately a third of that seen in *Er*Cry WT. Assuming similar protein quality, this suggests that there is a lower concentration of the radical species being measured – something that may be expected for a non-migratory species which does not require the radical pair for magnetoreception. Once again, the data are fit to three exponential models. All of the models show a (short) decay constant that is somewhat larger than that seen in *Er*Cry WT.

The $\Delta\Delta A$ trace reveals no growth on the timescale of the measurement, showing only a far more rapid decay of the magnetically sensitive species than seen in *Er*Cry WT – well below the 1 µs hypothesised to be needed for use as a compass sensor [27]. Comparing the magnitude of $\Delta\Delta A$ with that of *Er*Cry WT shows a similar intensity of approximately −0.3 OD, corresponding to an MFE of around 6 %. The $\Delta\Delta A$ data is fit to a mono-exponential as subtraction of the fits to the ΔA data yielded a fit that did not make physical sense.

Since $\Delta\Delta A$ does not increase in magnitude on the timescale of the measurements, it does not make sense to perform the same analysis as seen above on *Er*Cry WT in which the ΔA, $\Delta\Delta A$ and MFE are compared to one another. The fact that there is no rise in the magnitude of $\Delta\Delta A$ suggests that the competition between the recombination and formation of radical pair 2 is very different to that seen in *Er*Cry WT, most notably that recombination outcompetes the formation of radical pair 2, leading to a much shorter-lived magnetic field effect.

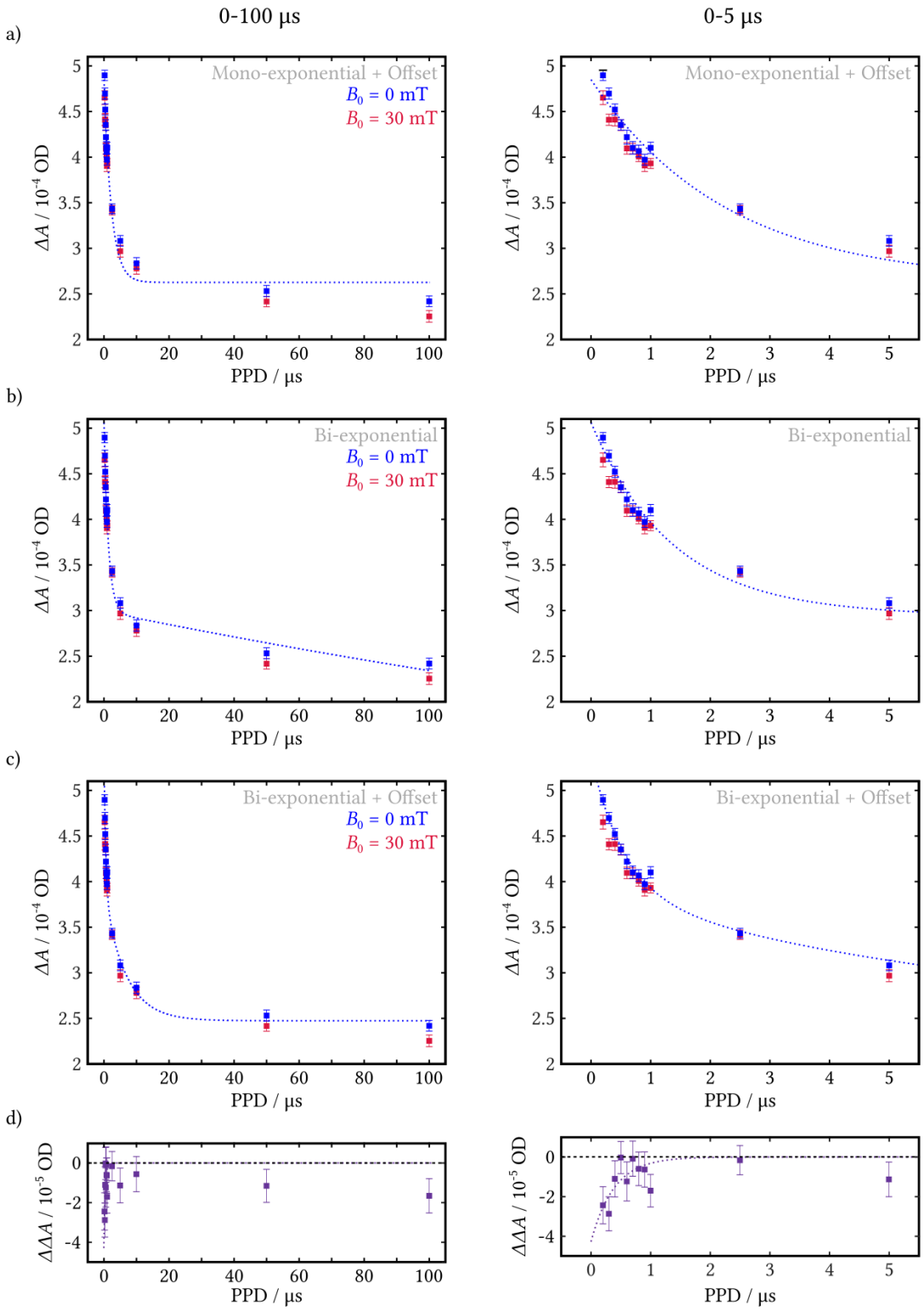


Figure 4.7: CRDS results for a time-resolved measurement on *Gg*Cry WT measured at 530 nm following photoexcitation at 450 nm (300 µJ). Error bars represent the standard error of the mean of 100 measurements at each time-point. The dashed lines show the various fits to the zero-field ΔA trace (blue) – a) mono-exponential with offset, b) bi-exponential without offset, and c) bi-exponential with offset. The field "on" (30 mT) traces are shown in red. The right panels show the horizontally expanded early pump-probe delay times (PPDs) from the left panels on the same vertical scale. d) $\Delta\Delta A$, which is the subtraction of the field "off" data from the field "on" data. The fit is a mono-exponential to the $\Delta\Delta A$ data.

***Gg*Cry WT**			
Parameter	Mono + Offset	Bi	Bi + Offset
y_0 / 10^{-3} OD	0.263 ± 0.009	–	0.248 ± 0.005
A_1 / 10^{-3} OD	0.222 ± 0.013	0.207 ± 0.012	0.148 ± 0.018
t_1 / µs	2.26 ± 0.44	1.34 ± 0.21	0.550 ± 0.152
A_2 / 10^{-3} OD	–	0.299 ± 0.009	0.141 ± 0.021
t_2 / µs	–	415 ± 101	6.50 ± 1.53
R^2	0.966	0.986	0.994

Table 4.2: Table showing the fitting parameters for the three exponential models, fit over the full range of pump-probe delay times, for the wild type cryptochrome 4 samples from *Gallus gallus* (*Gg*Cry WT).

Having compared a migratory and non-migratory species, it is worth comparing to these a non-migratory species that is known to orient using magnetic fields – cryptochrome 4 from the pigeon (*Cl*Cry WT). The data from the measurement of this cryptochrome are shown in Fig. 4.8. The magnitude of ΔA (i.e. the concentration of radical species) sits almost halfway between that seen in *Er*Cry WT and *Gg*Cry WT. Two of the models, the mono-exponential and the bi-exponential without offset, fit the long-timescale data less well than those seen in the other two species, with a good fit only achieved with the full bi-exponential model. Once again, the fits all show a decay constant of approximately 2 µs, although all are larger than their comparative *Er*Cry WT and *Gg*Cry WT values. It is also interesting to note that the mono-exponential model and that of the bi-exponential without offset are equivalent, with the component with infinite decay constant acting as the offset for the mono-exponential model.

Much like *Gg*Cry WT, $\Delta\Delta A$ in *Cl*Cry WT decays within the first microsecond, i.e. too fast to be recognised on the timescale of the experiment. This effect, however, appears to be shorter-lived than both *Gg*Cry WT and *Er*Cry WT and corresponds to an MFE of approximately 1.5 %. Once again, the $\Delta\Delta A$ data were fit to a mono-exponential as the subtraction of the ΔA fits yielded physically nonsensical results.

***Cl*Cry WT**			
Parameter	Mono + Offset	Bi	Bi + Offset
y_0 / 10^{-3} OD	0.754 ± 0.012	–	0.697 ± 0.023
A_1 / 10^{-3} OD	0.247 ± 0.015	0.247 ± 0.016	0.209 ± 0.007
t_1 / µs	3.11 ± 0.64	3.11 ± 0.68	1.30 ± 0.11
A_2 / 10^{-3} OD	–	0.754 ± 0.013	0.129 ± 0.020
t_2 / µs	–	∞	59.4 ± 24.0
R^2	0.962	0.962	0.998

Table 4.3: Table showing the fitting parameters for the three exponential models, fit over the full range of pump-probe delay times, for the wild type cryptochrome 4 samples from *Columba livia* (*Cl*Cry WT).

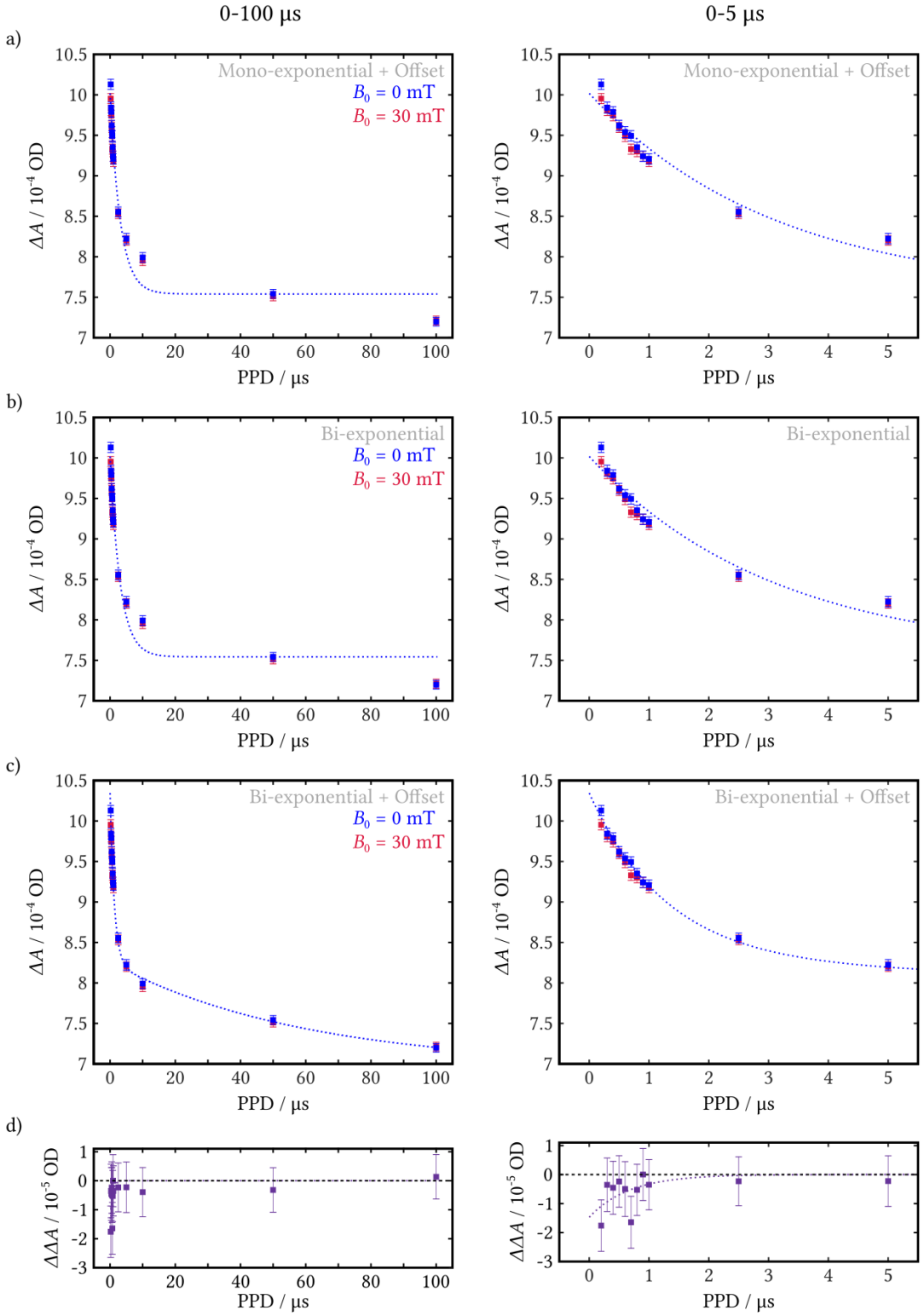


Figure 4.8: CRDS results for a time-resolved measurement on *Cl*Cry WT measured at 530 nm following photoexcitation at 450 nm (300 µJ). Error bars represent the standard error of the mean of 150 measurements at each time-point. The dashed lines show the various fits to the zero-field ΔA trace (blue) – a) mono-exponential with offset, b) bi-exponential without offset, and c) bi-exponential with offset. The field "on" (30 mT) traces are shown in red. The right panels show the horizontally expanded early pump-probe delay times (PPDs) from the left panels on the same vertical scale. d) $\Delta\Delta A$, which is the subtraction of the field "off" data from the field "on" data. The fit is a mono-exponential to the $\Delta\Delta A$ data.

Again, since there is no increase in magnitude in the $\Delta\Delta A$ signal on the timescale of the measurements performed, it does not make sense to perform a comparison of the ΔA, $\Delta\Delta A$ and MFE values. This, once again, suggests that the competition between recombination and formation of radical pair 2 is won by the former, leading to a much shorter-lived MFE.

Before proceeding to further experimental results, it is worth comparing the results seen above to one another more closely and commenting on a few features. To aid this comparison, the ΔA_{Off} traces for all three of the wild type cryptochromes and their respective $\Delta\Delta A$ traces are plotted in Fig. 4.9 a) and b), respectively.

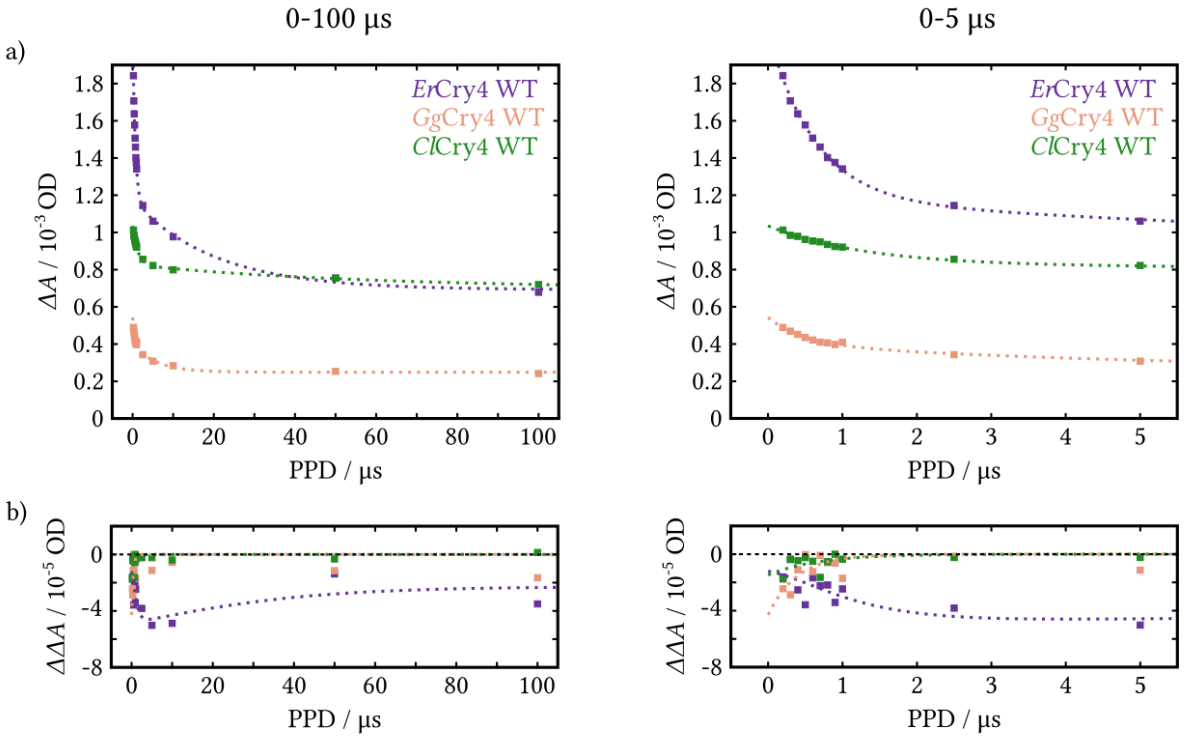


Figure 4.9: Figure showing a comparison of the time-resolved data, both a) the field "off" ΔA and b) $\Delta\Delta A$ values, as seen above for *Er*Cry WT (Fig. 4.5), *Gg*Cry WT (Fig. 4.7), and *Cl*Cry WT (Fig. 4.8) on the same scale. The bi-exponential fits are also shown to guide the eye; the fits to the $\Delta\Delta A$ traces of *Gg*Cry WT and *Cl*Cry WT are mono-exponential (explained in text). Error bars are omitted for clarity and can be seen above in the respective figures.

The trend described above in the initial intensities of ΔA is immediately noticeable, with the late-time values from *Er*Cry WT and *Cl*Cry WT being very similar. These two traces are also at nearly three times the magnitude of the *Gg*Cry WT, with all of them appearing to decay at approximately the same (slow) rate. The decay constants for the three species under the three exponential models are summarised again in Table 4.4.

However, the most striking difference between the migratory and non-migratory species is clear in the $\Delta\Delta A$ traces (Fig. 4.9 b). The magnitude of $\Delta\Delta A$ in *Er*Cry WT is the only one to increase on the timescale considered and is larger than both of the other samples. Additionally, it is clear that the effect of the magnetic field is felt over a much longer timescale than that of *Gg*Cry WT and *Cl*Cry WT, most likely due to the better competition between recombination and the formation of the secondary radical pair in the two non-migratory species, in contrast to the favoured formation of the secondary radical pair in *Er*Cry WT. The long-lived component could be a result of other conformations, some of the triplet state, or kinetics of the flavin. The latter is supported by transient absorption measurements that show a millisecond decay of $FADH^{\bullet}$ – a much longer timescale than is accounted for here.

It is also worth commenting on the non-zero $\Delta\Delta A$ in *Gg*Cry WT at late pump-probe delay times given that the $\Delta\Delta A$ trace decays to zero at early times – up to 2–3 µs. There is not a sensible physical reason as to why these points are non-zero (within error). It may, however, be noise as a result of the minute changes being detected, especially given the small magnitude of ΔA in *Gg*Cry WT. It is likely that the late pump-probe delay time points bias the bi-exponential fit, leading to compounding errors in the subtraction, which evidence themselves in the nonsensical fits to the data.

Fit	Parameter	**Wild Type**		
		Er	*Gg*	*Cl*
Mono + Offset	y_0 / 10^{-3} OD	0.857 ± 0.053	0.263 ± 0.009	0.754 ± 0.012
	A_1 / 10^{-3} OD	1.01 ± 0.10	0.222 ± 0.013	0.247 ± 0.015
	t_1 / µs	1.52 ± 0.40	2.26 ± 0.44	3.11 ± 0.64
	R^2	0.931	0.966	0.962
Bi	A_1 / 10^{-3} OD	0.962 ± 0.050	0.207 ± 0.012	0.247 ± 0.016
	t_1 / µs	0.800 ± 0.080	1.34 ± 0.21	3.11 ± 0.68
	A_2 / 10^{-3} OD	1.07 ± 0.03	0.299 ± 0.009	0.754 ± 0.013
	t_2 / µs	192 ± 22	415 ± 101	∞
	R^2	0.992	0.986	0.962
Bi + Offset	y_0 / 10^{-3} OD	0.684 ± 0.016	0.248 ± 0.005	0.697 ± 0.023
	A_1 / 10^{-3} OD	0.908 ± 0.025	0.148 ± 0.018	0.209 ± 0.007
	t_1 / µs	0.653 ± 0.037	0.550 ± 0.152	1.30 ± 0.11
	A_2 / 10^{-3} OD	0.476 ± 0.19	0.141 ± 0.021	0.129 ± 0.020
	t_2 / µs	22.9 ± 3.8	6.50 ± 1.53	59.4 ± 24.0
	R^2	0.999	0.994	0.998
	MFE / %	2	6	1.5

Table 4.4: Table showing the fitting parameters for the wild type cryptochrome 4 samples from *Erithacus rubecula* (*Er*Cry WT), *Gallus gallus* (*Gg*Cry WT), and *Columba livia* (*Cl*Cry WT). The approximate magnetic field effects are shown for each species.

4.4 Comparing the Avian W369F Cryptochrome Mutants

It has not until recently been known how many tryptophan residues are involved in the electron transfer process in *Er*Cry as there are three in cryptochrome 1 from thale cress (*Arabidopsis thaliana*, *At*Cry1) and four in cryptochrome from fruit flies (*Drosophila melanogaster*, *Dm*Cry) [35, 90, 134]. The penultimate radical pair of the proposed magnetosensing, therefore, has been unknown. The strategy employed by the group was, therefore, based on expression of several mutant samples of *Erithacus rubecula* cryptochrome in which each of the tryptophan residues is replaced by a phenylalanine in turn, phenylalanine not being able to undergo electron transfer.[3] Using picosecond-transient absorption spectroscopy, it was found that there was no radical signal in the W395F (Trp_A) sample, as expected [100]. For the W372F (Trp_B) and W318F (Trp_C) samples, radicals were detected showing increasing lifetimes from about 200 ps to 1 ns. More interestingly, however, was the fact that both the W369F (Trp_D) and wild type protein showed radical signals with lifetimes greater than 1 µs.

Following work by Zollitsch on both *Dm*Cry W394F, which also has the terminal tryptophan residue replaced with a phenylalanine, and *Er*Cry W369F,[4] which showed much stronger magnetic field effects, it was decided to compare the three avian wild type proteins measured above with their W369F mutants.

Following the same order of species as above, the time-resolved measurement of *Er*Cry W369F at 530 nm is shown in Fig. 4.10. The ΔA magnitude is approximately half of that seen in the wild type sample, corresponding to a lower concentration of radical species. Once again, the application of a magnetic field decreases the initial concentration of radicals, as expected for a singlet-born radical pair. The various fitting parameters are shown in Tables 4.5 (full fit) and 4.6 (100 µs).

The effect of the applied magnetic field is most noticeable in the $\Delta\Delta A$ signal (Fig. 4.10 d), which shows marked differences to the wild type. The first, and perhaps clearest, change is the long-lived nature of the magnetic field effect. After growing to a maximum magnitude in the first approximately 2 µs, it decreases to approximately half of its original intensity and decays extremely slowly therefrom. The maximum MFE is approximately 21 %.

It is clear that the data are reasonably well-fitted to a mono-exponential model, with the short-timescale data understandably better fitted by moving to the bi-exponential models, which effectively provide an offset due to t_2 being being longer than the largest experiment pump-probe delay time.

[3] Measurements by the author were not performed on all the tryptophan ⟶ phenylalanine mutants – only on the W369F mutant. The experiments on the tryptophan mutants were performed by single-pass picosecond transient absorption spectroscopy and results are presented in the work by Xu *et al.* [100].

[4] Zollitsch's *Er*Cry W369F samples also contained the minor sequence errors at the C-terminus tail, as for the wild type sample.

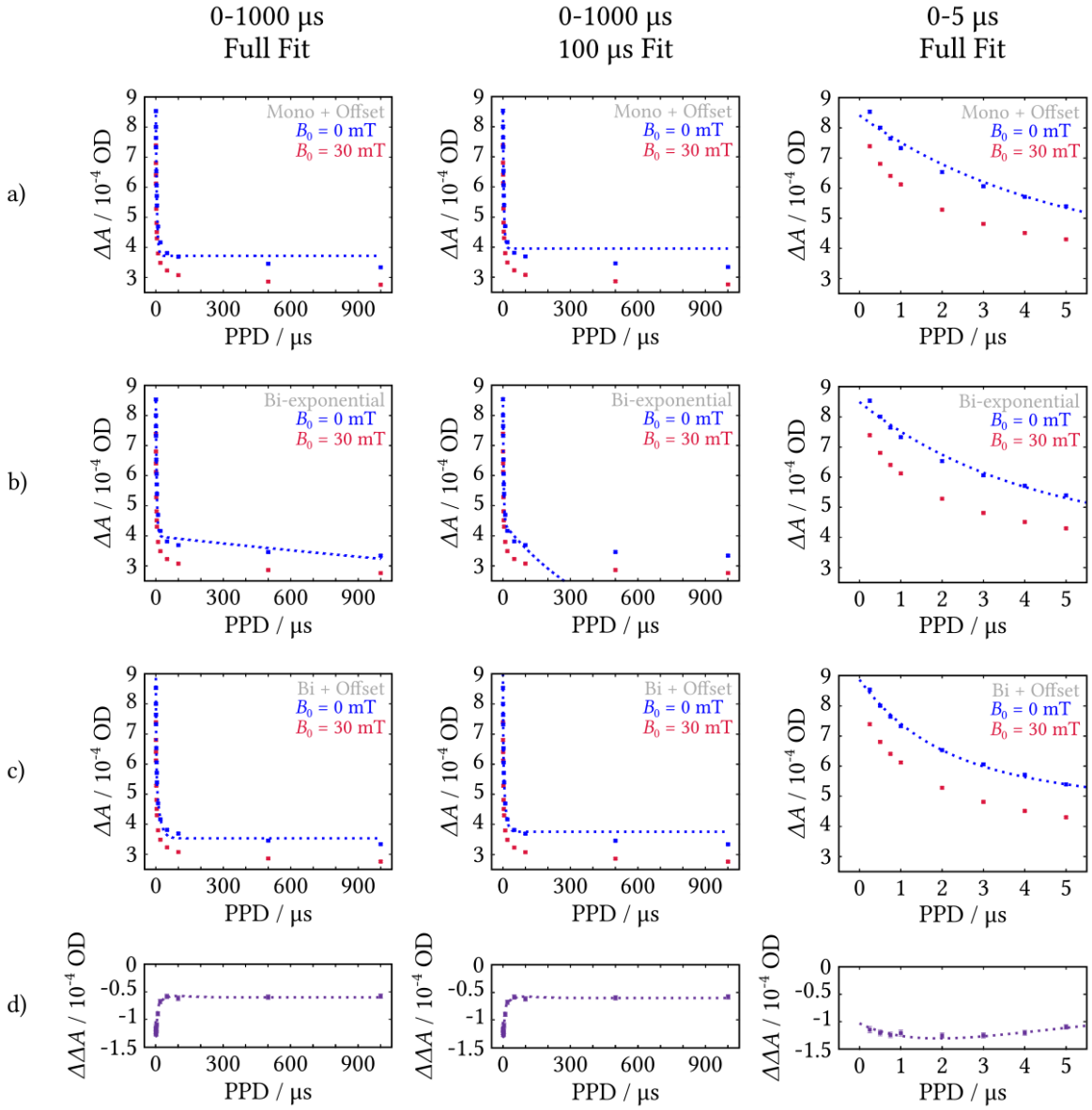


Figure 4.10: CRDS results for a time-resolved measurement on *Er*Cry W369F measured at 530 nm following photoexcitation at 450 nm (300 µJ). Error bars represent the standard error of the mean of 150 measurements at each time-point. The dashed lines show the various fits (described in grey) to the full trace (left and right columns) and first 100 µs (centre) of the zero-field ΔA trace (blue) – a) mono-exponential with offset, b) bi-exponential without offset, and c) bi-exponential with offset. The field "on" (30 mT) traces are shown in red. The right panels show the horizontally expanded early pump-probe delay times (PPDs) from the left-most panels on the same vertical scale. d) $\Delta\Delta A$, which is the subtraction of the field "off" data from the field "on" data. The fit is the subtraction of the bi-exponential with offset fits to the ΔA data.

Also noticeable is that the fitting performed over both the full and shorter pump-probe delay times provide very similar time constants, with an obvious exception for the bi-exponential without offset in the 100 µs fitting which is clearly wrong and completely ignores the long-lived component in the data, having been biased by the early-timescale data. The approximately 4 µs time constant seen in the mono-exponential and bi-exponential (without offset) fits could be the weighted average of the two time constants seen in the bi-exponential fit with offset, the two decay constants being similar to those seen in the wild type representing the deprotonation of $TrpH^{\bullet+}$(short, ≈ 1 µs) and formation of radical pair 2 (long, ≈ 20 µs).

***Er*Cry W369F – Full Fit**			
Parameter	Mono + Offset	Bi	Bi + Offset
y_0 / 10^{-3} OD	0.372 ± 0.012	–	0.353 ± 0.007
A_1 / 10^{-3} OD	0.469 ± 0.021	0.450 ± 0.018	0.303 ± 0.034
t_1 / µs	4.72 ± 0.55	4.08 ± 0.41	1.74 ± 0.39
A_2 / 10^{-3} OD	–	0.399 ± 0.012	0.230 ± 0.038
t_2 / µs	–	4790 ± 1620	16.2 ± 4.2
R^2	0.981	0.990	0.997

Table 4.5: Table showing the fitting parameters for the three exponential models, fit over the full range of pump-probe delay times, for the W369F mutant cryptochrome 4 samples from *Erithacus rubecula* (*Er*Cry W369F).

***Er*Cry W369F – 100 µs Fit**			
Parameter	Mono + Offset	Bi	Bi + Offset
y_0 / 10^{-3} OD	0.395 ± 0.013	–	0.376 ± 0.004
A_1 / 10^{-3} OD	0.453 ± 0.018	0.416 ± 0.018	0.246 ± 0.018
t_1 / µs	4.14 ± 0.44	3.26 ± 0.35	1.21 ± 0.17
A_2 / 10^{-3} OD	–	0.444 ± 0.017	0.280 ± 0.019
t_2 / µs	–	473 ± 149	9.59 ± 1.03
R^2	0.986	0.993	0.999

Table 4.6: Table showing the fitting parameters for the three exponential models, fit over the first 100 µs of pump-probe delay times, for the W369F mutant cryptochrome 4 samples from *Erithacus rubecula* (*Er*Cry W369F).

Performing analysis similar to that seen in the wild type, i.e. over the period in which $\Delta\Delta A$ increases in magnitude, it is clear that, once again, there is good agreement between the rise of the magnetic field effect and the decay of the ΔA signal, as seen in Fig. 4.11, although there is more noise and the data points are too few to make any conclusive statements. The decay constant for this is 1.59 µs, which is not far off the value obtained for the wild type sample (1.23 µs). This agreement suggests that the decay is, once again, the deprotonation of $TrpH^{\bullet+}$(as also seen in the bi-exponential fit above), after which there is competition between this and

the formation of radical pair 2. The much longer-lived nature of the magnetic field effect suggests that there may be other processes that maintain this effect that are not immediately identifiable through the measurements performed here.

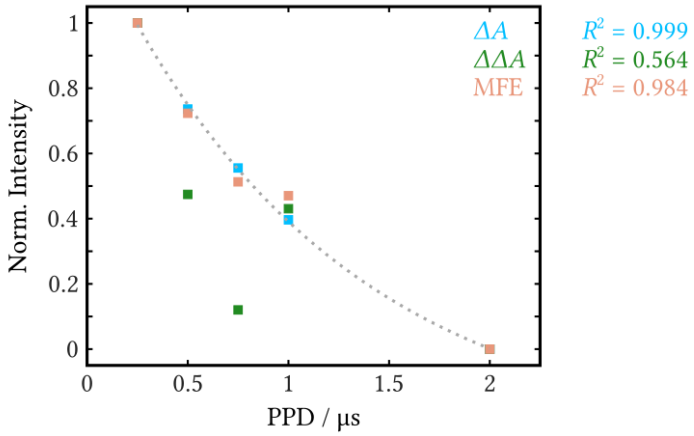


Figure 4.11: Normalised and baseline-corrected data from the time-resolved measurement on *Er*Cry W369F showing the ΔA, $\Delta\Delta A$, and MFE. The ΔA data are fit to a mono-exponential with decay constant of 1.59 µs. The number of data points limit clear conclusions, but the ΔA, $\Delta\Delta A$ and MFE all show reasonable agreement. The number of data points limits clear conclusions, but the ΔA, $\Delta\Delta A$ and MFE all show reasonable agreement. The goodness of fit (R^2) for each dataset to the fit shown is provided alongside the figure.

Performing the same time-resolved experiment on *Gg*Cry W369F yields a similar comparison with *Gg*Cry WT to that of the samples of *Er*Cry, with the magnitude of ΔA sitting at approximately half that of the wild type. The data are, as in the *Er*Cry W369F sample, fit to three different exponential functions and over two separate temporal regions – one over the full millisecond measured and the other over the first 100 µs and shown in Fig. 4.12, respectively. The fitting parameters for these temporal fits are shown in Tables 4.7 and 4.8.

Looking now at $\Delta\Delta A$ for *Gg*Cry W369F, the trace shows similarities to the *Er*Cry W369F measurement with a long-lived magnetic field effect with initial rise over the first 2 µs, before decaying at roughly the same rate as the ΔA values. The maximum MFE is approximately 14 % – smaller than that seen in *Er*Cry W369F, which is also a switch in the order of the magnitudes of the magnetic field effects seen in the wild type proteins. The value of $\Delta\Delta A$ is approximately the same as that seen in *Gg*Cry WT, but is five times smaller than seen in *Er*Cry W369F.

The data are, again, reasonably well-fitted by the mono-exponential and improved by allowing for the short decay constant, especially at the short pump-probe delay times. The approximate 10 µs decay constant seen in all the fits is, like the *Er*Cry W369F, a weighted average of the geminate recombination and forward reaction to radical pair 2, but evidently shows a different weight of the two components, being more dominated by the latter.

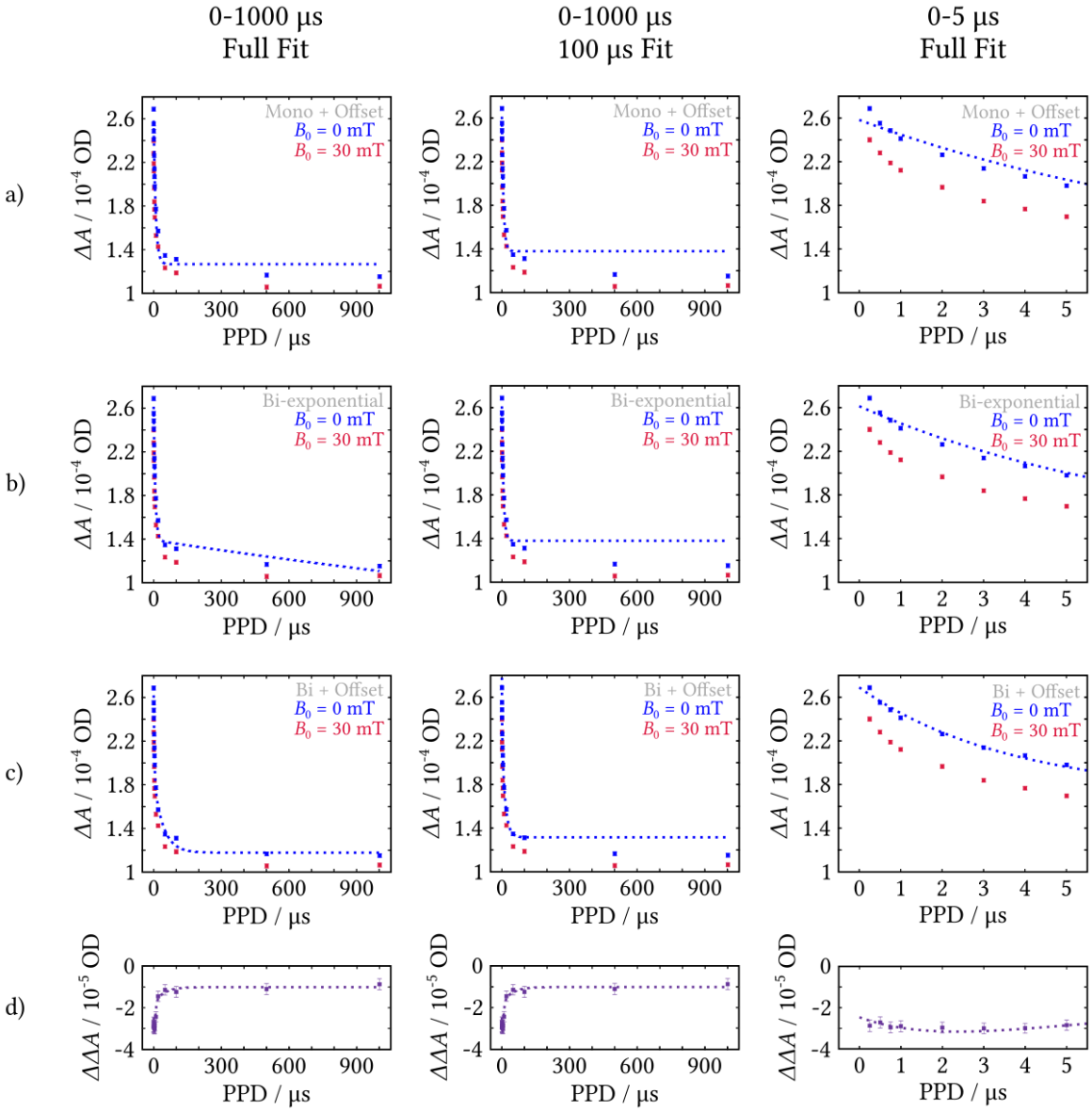


Figure 4.12: CRDS results for a time-resolved measurement on *Gg*Cry W369F measured at 530 nm following photoexcitation at 450 nm (300 µJ). Error bars represent the standard error of the mean of 150 measurements at each time-point. The dashed lines show the various fits (described in grey) to the full trace (left and right columns) and first 100 µs (centre) of the zero-field ΔA trace (blue) – a) mono-exponential with offset, b) bi-exponential without offset, and c) bi-exponential with offset. The field "on" (30 mT) traces are shown in red. The right panels show the horizontally expanded early pump-probe delay times (PPDs) from the left-most panels on the same vertical scale. d) $\Delta\Delta A$, which is the subtraction of the field "off" data from the field "on" data. The fit is the subtraction of the bi-exponential with offset fits to the ΔA data.

***Gg*Cry W369F – Full Fit**			
Parameter	Mono + Offset	Bi	Bi + Offset
y_0 / 10^{-3} OD	0.127 ± 0.005	–	0.118 ± 0.003
A_1 / 10^{-3} OD	0.132 ± 0.007	0.122 ± 0.006	0.0831 ± 0.0090
t_1 / µs	9.30 ± 1.42	7.29 ± 1.00	3.27 ± 0.65
A_2 / 10^{-3} OD	–	0.139 ± 0.005	0.0682 ± 0.0093
t_2 / µs	–	4400 ± 1470	41.7 ± 10.5
R^2	0.974	0.986	0.996

Table 4.7: Table showing the fitting parameters for the three exponential models, fit over the full range of pump-probe delay times, for the W369F mutant cryptochrome 4 samples from *Gallus gallus* (*Gg*Cry W369F).

***Gg*Cry W369F – 100 µs Fit**			
Parameter	Mono + Offset	Bi	Bi + Offset
y_0 / 10^{-3} OD	0.138 ± 0.005	–	0.132 ± 0.002
A_1 / 10^{-3} OD	0.123 ± 0.006	0.123 ± 0.006	0.0509 ± 0.0040
t_1 / µs	7.36 ± 1.00	7.36 ± 1.06	1.17 ± 0.22
A_2 / 10^{-3} OD	–	0.138 ± 0.005	0.0956 ± 0.0041
t_2 / µs	–	∞	14.4 ± 1.3
R^2	0.980	0.980	0.999

Table 4.8: Table showing the fitting parameters for the three exponential models, fit over the first 100 µs of pump-probe delay times, for the W369F mutant cryptochrome 4 samples from *Gallus gallus* (*Gg*Cry W369F).

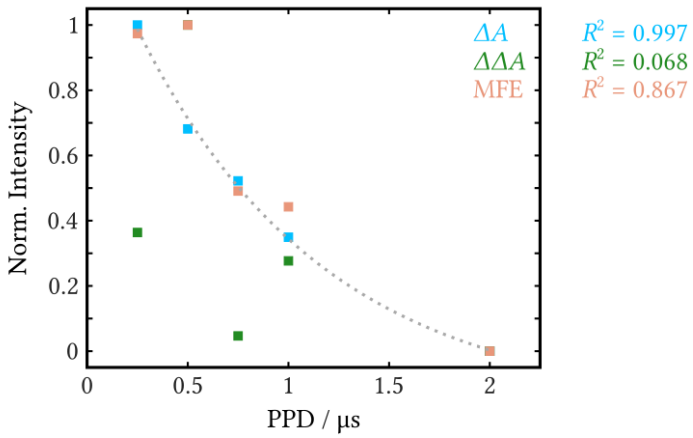


Figure 4.13: Normalised and baseline-corrected data from the time-resolved measurement on *Gg*Cry W369F showing the ΔA, $\Delta\Delta A$, and MFE. The data are fit to a mono-exponential with decay constant of 1.52 µs. The number of data points limits clear conclusions, but the ΔA and MFE show reasonable agreement; the $\Delta\Delta A$ shows a poorer fit, which may be a result of the number of data points. The goodness of fit (R^2) for each dataset to the fit shown is provided alongside the figure.

Once again, analysis on the timescale of the building in of the $\Delta\Delta A$ intensity can be performed, shown in Fig. 4.13, and has a slightly poorer match between the three parameters than in *Er*Cry, both the WT and W369F samples. This may be a remnant from the weaker competition between recombination and formation of radical pair 2, which was evident in the wild type by the purely decaying trace seen in the $\Delta\Delta A$ signal, which is not overcome in the mutant. The decay constant is 1.52 µs, which is similar to that seen in *Er*Cry WT and W369F, corresponding to the deprotonation of $TrpH^{\bullet+}$.

The final time-resolved measurement is that of *Cl*Cry W369F, shown in Fig. 4.14, with fitting parameters shown in Tables 4.9 and 4.10. The magnitude of ΔA is, once again, much diminished in comparison to the wild type measurement, although not quite as much as seen in the *Er*Cry and *Gg*Cry cases. The fits appear to be a poorer match in the 100 µs fits and, in all cases, seem to misfit either the long or short component. The non-offset bi-exponential 100 µs fit is clearly wrong and fails to match the late-PPD data, while the other two fits overestimate the offset (or similar through the long decay constant).

***Cl*Cry W369F – Full Fit**			
Parameter	Mono + Offset	Bi	Bi + Offset
y_0 / 10^{-3} OD	0.223 ± 0.012	–	0.199 ± 0.008
A_1 / 10^{-3} OD	0.369 ± 0.016	0.341 ± 0.014	0.229 ± 0.027
t_1 / µs	11.6 ± 1.6	9.25 ± 1.07	4.60 ± 0.88
A_2 / 10^{-3} OD	–	0.258 ± 0.012	0.186 ± 0.029
t_2 / µs	–	2840 ± 830	48.2 ± 12.0
R^2	0.981	0.991	0.996

Table 4.9: Table showing the fitting parameters for the three exponential models, fit over the full range of pump-probe delay times, for the W369F mutant cryptochrome 4 samples from *Columba livia* (*Cl*Cry W369F).

***Cl*Cry W369F – 100 µs Fit**			
Parameter	Mono + Offset	Bi	Bi + Offset
y_0 / 10^{-3} OD	0.25 ± 0.012	–	0.240 ± 0.005
A_1 / 10^{-3} OD	0.345 ± 0.014	0.279 ± 0.020	0.108 ± 0.011
t_1 / µs	9.49 ± 1.14	6.10 ± 0.89	0.958 ± 0.225
A_2 / 10^{-3} OD	–	0.329 ± 0.020	0.297 ± 0.009
t_2 / µs	–	264 ± 68	14.7 ± 1.1
R^2	0.985	0.993	0.999

Table 4.10: Table showing the fitting parameters for the three exponential models, fit over the first 100 µs of pump-probe delay times, for the W369F mutant cryptochrome 4 samples from *Columba livia* (*Cl*Cry W369F).

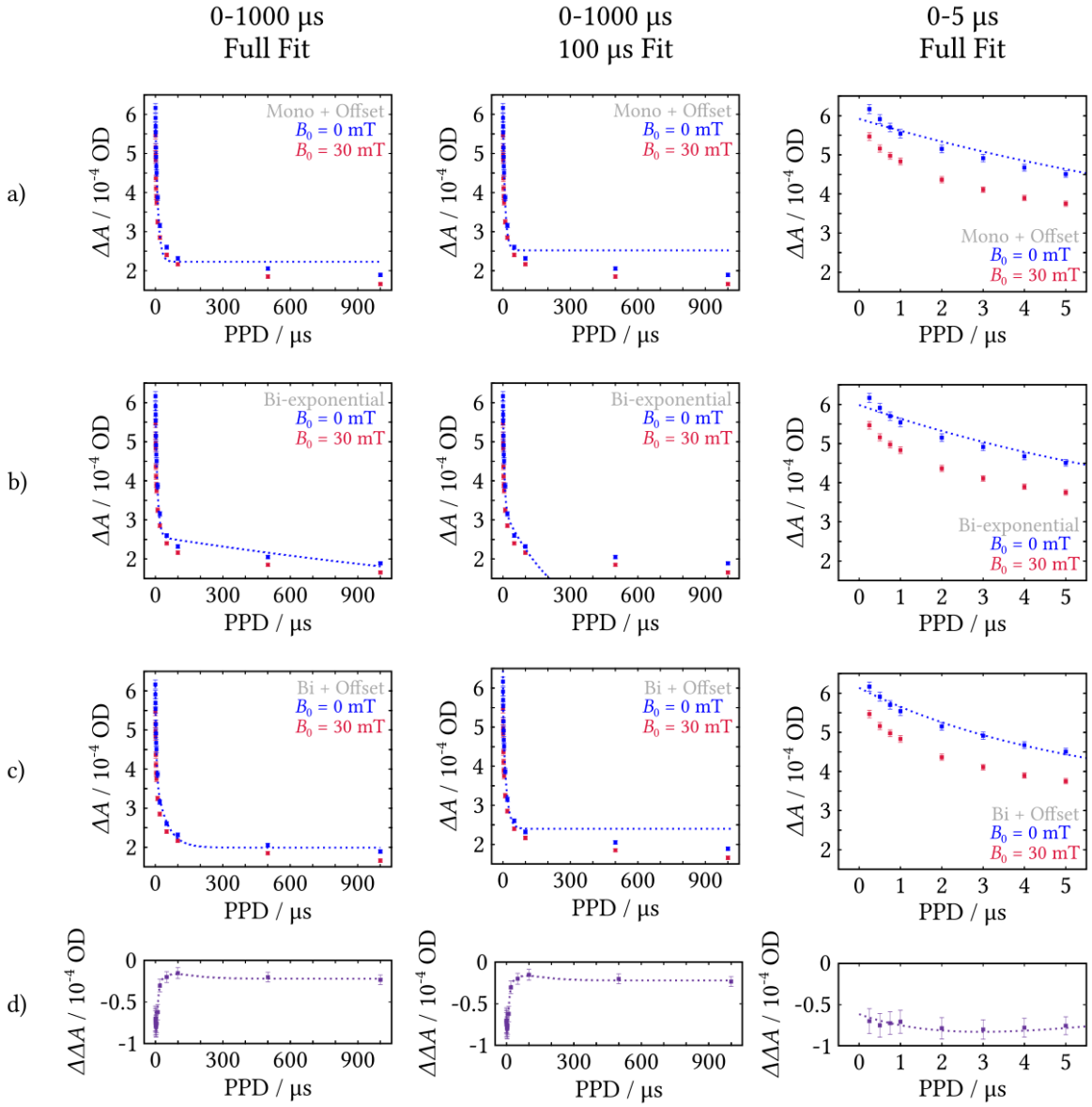


Figure 4.14: CRDS results for a time-resolved measurement on *Cl*Cry W369F measured at 530 nm following photoexcitation at 450 nm (300 µJ). Error bars represent the standard error of the mean of 150 measurements at each time-point. The dashed lines show the various fits (described in grey) to the full trace (left and right columns) and first 100 µs (centre) of the zero-field ΔA trace (blue) – a) mono-exponential with offset, b) bi-exponential without offset, and c) bi-exponential with offset. The field "on" (30 mT) traces are shown in red. The right panels show the horizontally expanded early pump-probe delay times (PPDs) from the left-most panels on the same vertical scale. d) $\Delta\Delta A$, which is the subtraction of the field "off" data from the field "on" data. The fit is the subtraction of the bi-exponential with offset fits to the ΔA data.

Considering now the $\Delta\Delta A$ for *Cl*Cry W369F, similarities to both the other W369F mutants measured are clear, most notably the long-lived MFE which reached a maximum of approximately 16 %.

The first couple of microseconds are, once again, considered and show a better match of the ΔA, $\Delta\Delta A$ and MFE traces (seen in Fig. 4.15) than that seen in *Gg*Cry W369F, but not as good a match as that in *Er*Cry W369F. This could be rationalised in the same way as for the *Gg*Cry W369F sample in that the mutation does not fully overcome the poorer competition between the two main processes – recombination and formation of radical pair 2. In nearly perfect agreement with the two other W369F mutants, the decay constant – corresponding to the deprotonation of $TrpH^{\bullet+}$ – is approximately 1.58 µs.

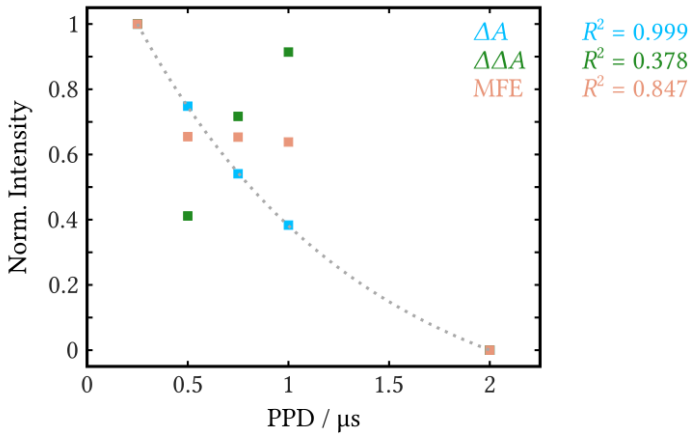


Figure 4.15: Normalised and baseline-corrected data from the time-resolved measurement on *Cl*Cry W369F showing the ΔA, $\Delta\Delta A$, and MFE. The data are fit to a mono-exponential with decay constant of 1.58 µs. The number of data points limits clear conclusions, but the ΔA, $\Delta\Delta A$ and MFE all show reasonable agreement. The goodness of fit (R^2) for each dataset to the fit shown is provided alongside the figure.

Once again, a comparison is made of all three of the W369F mutants, the field "off" ΔA traces and $\Delta\Delta A$ traces being shown in Fig. 4.16 a) and b), respectively. The data are shown up to the 100 µs pump-probe delay time to allow greater comparison with the wild type samples. The trend in initial ΔA values is the same as seen in the wild type samples with *Er*Cry W369F being the largest and *Gg*Cry W369F the smallest. All three traces decay at approximately the same rate before plateauing at times larger than 100 µs (not shown, but evident above). The fits shown are the model using a bi-exponential with offset. The fitting parameters for the ΔA traces of the W369F mutants are shown in Tables 4.11 (fit over the full microsecond) and 4.12 (fit over the first 100 µs).

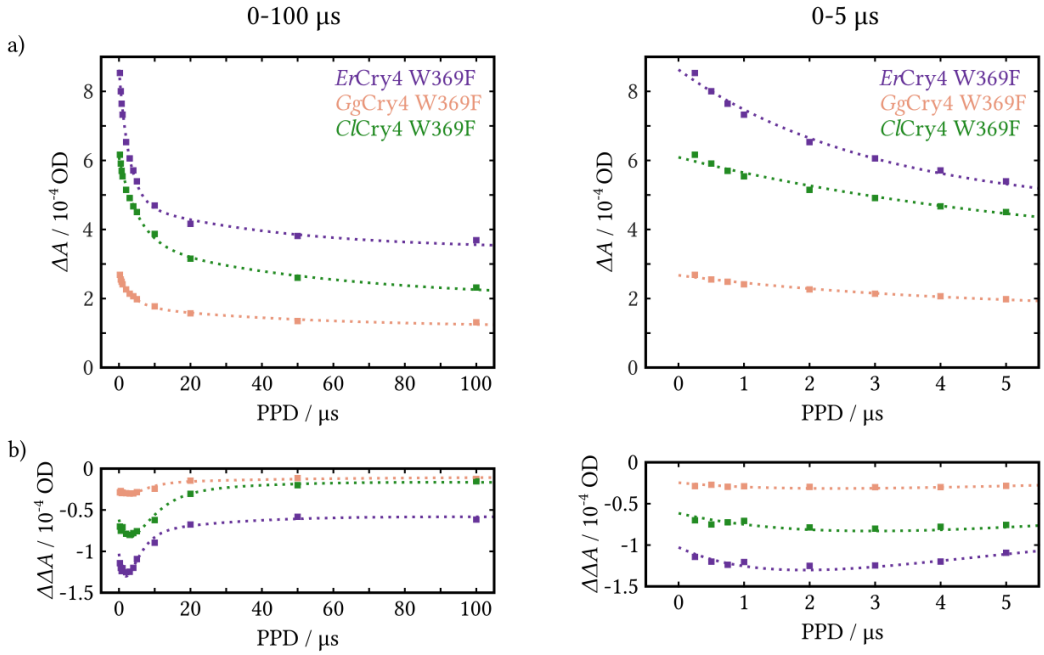


Figure 4.16: Figure showing a comparison of the time-resolved data, both a) the field "off" ΔA and b) $\Delta\Delta A$ values, seen above for *Er*Cry W369F (Fig. 4.10), *Gg*Cry W369F (Fig. 4.12), and *Cl*Cry W369F (Fig. 4.14) on the same scale. Only the first 100 µs are shown due to the near flat traces over the range from 100–1000 µs. The bi-exponential fits over the full region are also shown to guide the eye. Error bars are omitted for clarity and can be seen above in the respective figures.

Fit		W369F - Full Fit		
		Er	*Gg*	*Cl*
Mono + Offset	y_0 / 10^{-3} OD	0.372 ± 0.012	0.127 ± 0.005	0.223 ± 0.012
	A_1 / 10^{-3} OD	0.469 ± 0.021	0.132 ± 0.007	0.369 ± 0.016
	t_1 / µs	4.72 ± 0.55	9.30 ± 1.42	11.6 ± 1.6
	R^2	0.981	0.974	0.981
Bi	A_1 / 10^{-3} OD	0.450 ± 0.018	0.122 ± 0.006	0.341 ± 0.014
	t_1 / µs	4.08 ± 0.41	7.29 ± 1.00	9.25 ± 1.07
	A_2 / 10^{-3} OD	0.399 ± 0.012	0.139 ± 0.005	0.258 ± 0.012
	t_2 / µs	4790 ± 1620	4400 ± 1470	2840 ± 830
	R^2	0.990	0.986	0.991
Bi + Offset	y_0 / 10^{-3} OD	0.353 ± 0.007	0.118 ± 0.003	0.199 ± 0.008
	A_1 / 10^{-3} OD	0.303 ± 0.034	0.0831 ± 0.0090	0.229 ± 0.027
	t_1 / µs	1.74 ± 0.39	3.27 ± 0.65	4.60 ± 0.88
	A_2 / 10^{-3} OD	0.230 ± 0.038	0.0682 ± 0.0093	0.186 ± 0.029
	t_2 / µs	16.2 ± 4.2	41.7 ± 10.5	48.2 ± 12.0
	R^2	0.997	0.996	0.996
	MFE / %	21	14	16

Table 4.11: Table showing the fitting parameters for the fits to ΔA over the whole timescale for the W369F mutant cryptochrome 4 samples from *Erithacus rubecula* (*Er*Cry W369F), *Gallus gallus* (*Gg*Cry W369F), and *Columba livia* (*Cl*Cry W369F). The approximate magnetic field effects are shown for each species.

Looking next at the $\Delta\Delta A$ values, it is clear that there is a greater effect of the magnetic field in the *Er*Cry W369F sample compared to the others, with both *Gg*Cry W369F and *Cl*Cry W369F showing similar long-timescale values, despite the initial two-fold difference in magnitude between the latter two. All show an initial increase in the magnitude of $\Delta\Delta A$ over the first couple of microseconds, although this is far less pronounced than seen in the trace for *Er*Cry WT. Comparison of the first 2 µs shows similar decay constants of approximately 1.5 µs, suggesting that this might be the deprotonation of $TrpH^{\bullet+}$, as seen in the wild type samples. Consideration of the full bi-exponential model for the ΔA traces suggested that there is a greater contribution of the long-lived radical pair 2, which contributed to increasing the magnitude of the decay constants seen in the mono-exponential model.

Fit		**W369F – 100 µs Fit**		
		Er	*Gg*	*Cl*
Mono + Offset	y_0 / 10^{-3} OD	0.395 ± 0.013	0.138 ± 0.005	0.252 ± 0.012
	A_1 / 10^{-3} OD	0.453	0.123 ± 0.006	0.345 ± 0.014
	t_1 / µs	4.14 ± 0.44	7.36 ± 1.00	9.49 ± 1.14
	R^2	0.986	0.980	0.985
Bi	A_1 / 10^{-3} OD	0.416 ± 0.018	0.123 ± 0.006	0.279 ± 0.020
	t_1 / µs	3.26 ± 0.35	7.36 ± 1.06	6.10 ± 0.89
	A_2 / 10^{-3} OD	0.444 ± 0.017	0.138 ± 0.005	0.329 ± 0.020
	t_2 / µs	473 ± 149	∞	264 ± 68
	R^2	0.993	0.980	0.993
Bi + Offset	y_0 / 10^{-3} OD	0.376 ± 0.004	0.132 ± 0.002	0.240 ± 0.005
	A_1 / 10^{-3} OD	0.246 ± 0.018	0.0509 ± 0.0040	0.108 ± 0.011
	t_1 / µs	1.21 ± 0.17	1.17 ± 0.22	0.958 ± 0.225
	A_2 / 10^{-3} OD	0.280 ± 0.019	0.0956 ± 0.0041	0.297 ± 0.009
	t_2 / µs	9.59 ± 1.03	14.4 ± 1.3	14.7 ± 1.1
	R^2	0.999	0.999	0.999
	MFE / %	21	14	16

Table 4.12: Table showing the fitting parameters for the fits to ΔA over the first 100 µs for the W369F mutant cryptochrome 4 samples from *Erithacus rubecula* (*Er*Cry W369F), *Gallus gallus* (*Gg*Cry W369F), and *Columba livia* (*Cl*Cry W369F). The approximate magnetic field effects are shown for each species.

4.4.1 Summary

The results above show the first time-resolved magnetic field effects measured on wild type cryptochrome 4 proteins and point mutants thereof from three avian species: *Erithacus rubecula*, *Gallus gallus* and *Columba livia*. A summary of the fitting parameters to all of the samples measured is shown in Table 4.13.

Considering first the wild type proteins, there is a decrease in the initial intensity of ΔA from migratory to non-migratory ($\Delta A_{\mathrm{Er}} > \Delta A_{\mathrm{Cl}} > \Delta A_{\mathrm{Gg}}$). While the radical concentrations may be higher in *Er*Cry WT and *Cl*Cry WT (evidenced by larger ΔA values), their magnetic field

Fit		Wild Type			W369F - Full Fit			W369F - 100 µs Fit		
		Er	*Gg*	*Cl*	*Er*	*Gg*	*Cl*	*Er*	*Gg*	*Cl*
Mono + Offset	y_0 / %	45.9	54.2	75.3	44.2	49.0	37.7	46.6	52.8	42.2
	A_1 / %	54.1	45.8	24.7	55.8	51.0	62.3	53.4	47.2	57.8
	t_1 / µs	1.52	2.26	3.11	4.72	9.30	11.6	4.14	7.36	9.49
Bi	A_1 / %	47.3	40.9	75.3	53.0	46.9	56.9	48.4	47.2	45.9
	t_1 / µs	0.800	1.34	3.11	4.08	7.29	9.25	3.26	7.36	6.10
	A_2 / %	52.7	59.1	24.7	47.0	53.1	43.1	51.6	52.8	54.1
	t_2 / µs	192	415	∞	4790	4400	2840	473	∞	265
Bi + Offset	y_0 / %	33.1	46.2	67.4	39.9	43.8	32.5	41.6	47.3	37.2
	A_1 / %	43.9	27.5	20.2	34.2	30.9	37.3	27.3	18.3	16.7
	t_1 / µs	0.652	0.550	1.30	1.74	3.27	4.60	1.21	1.17	0.958
	A_2 / %	23.0	26.3	12.4	25.9	25.3	30.3	31.0	34.4	46.1
	t_2 / µs	22.9	6.50	59.4	16.2	41.7	48.2	9.59	14.4	14.7

Table 4.13: Table summarising the fitting data for the six cryptochrome samples measured in this section. The full-time and 100 µs fits for the W369F samples are both shown. To facilitate comparison, the intensity values (A_1, A_2, and y_0) are shown as percentages, rather than their intensities.

effects are approximately equal at 2 % and 1.5 %, respectively. These MFEs are smaller than that seen in *Gg*Cry WT (6 %). The full bi-exponential model (along with work by Xu *et al.*) suggests that there are two processes competing: geminate recombination and formation of the secondary radical pair; the decay constant of the former is approximately 1.5 µs [100]. The competition between these two processes is best matched in *Er*Cry WT, evidenced by the growing in of $\Delta\Delta A$, which was not evident in either of the other two wild type proteins. This marked difference was made even starker by the fact that the $\Delta\Delta A$ value in *Er*Cry WT was still non-zero at the maximum timescale measured, as opposed to the other species which showed sub-microsecond decays. In the bi-exponential model, the long decay constant is proposed to be a combination of delayed recombination of the radical pair and the formation of the secondary radical pair.

In the W369F mutants, the same trend of initial ΔA values was seen ($\Delta A_{\mathrm{Er}} > \Delta A_{\mathrm{Cl}} > \Delta A_{\mathrm{Gg}}$), alongside much larger magnetic field effects. The largest of these field effects was seen in *Er*Cry W369F (21 %), with *Cl*Cry W369F and *Gg*Cry W369F showing similar, but smaller, MFEs of 16 % and 14 %, respectively. Use of the bi-exponential model again suggests that the two processes seen in the wild type proteins are still evident. In the W369F mutants, however, the formation of the secondary radical pair appears to take precedence, leading to the slower decay seen in the mono-exponential model. This is further supported by consideration of the first 2 µs – the approximate timescale over which the magnitude of $\Delta\Delta A$ increases – which shows a decay constant very similar to that seen in the wild type measurements. This decay constant is attributed to the geminate recombination.

There are many similarities between the three W369F species in the $\Delta\Delta A$ traces, with all showing a long-lived and slowly decaying plateau after the initial rise in the magnitude.

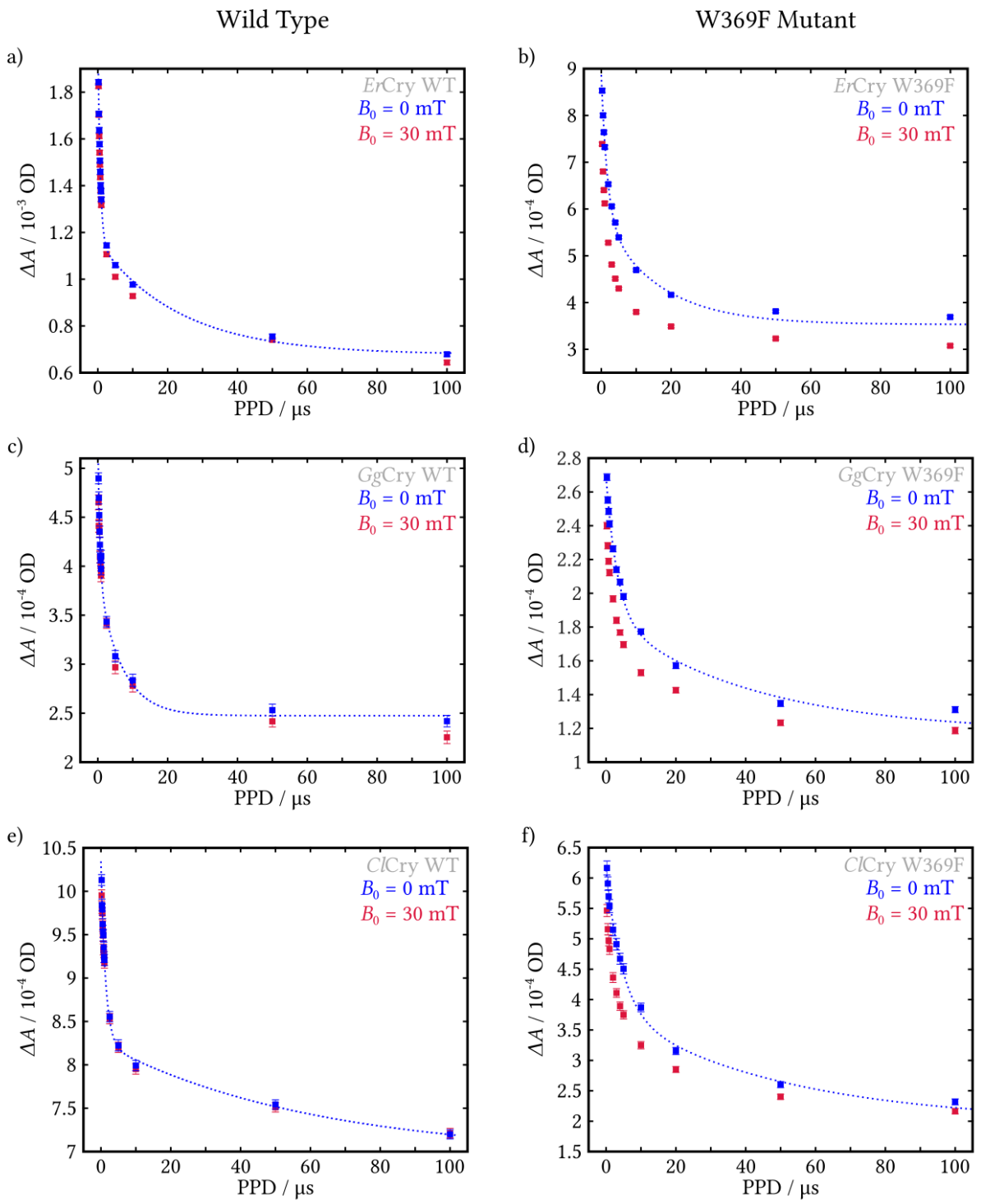


Figure 4.17: Figure showing the time-resolved ΔA traces for a) *Er*Cry WT, b) *Er*Cry W369F, c) *Gg*Cry WT, d) *Gg*Cry W369F, e) *Cl*Cry WT, and f) *Cl*Cry W369F. Both the field "on" (B_0 = 30 mT) (red) and field "off" (blue) traces are shown. The full bi-exponential fits to the field "off" data are shown.

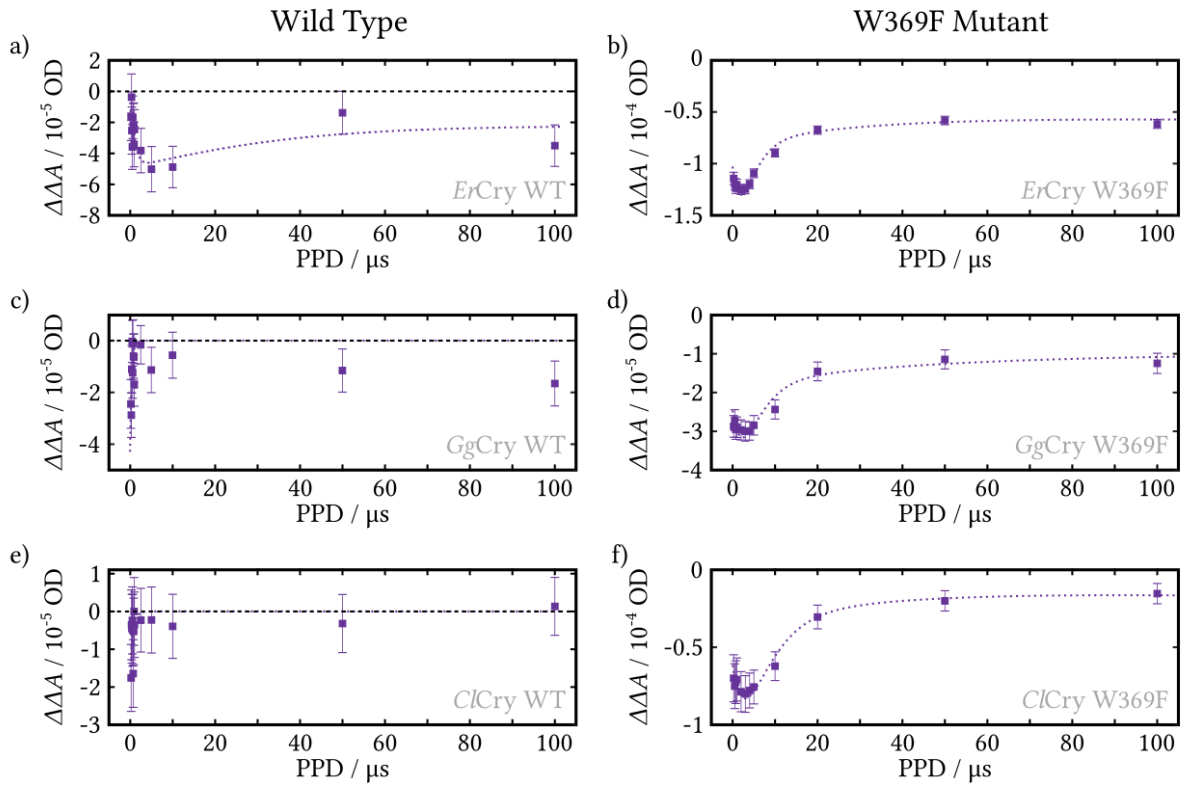


Figure 4.18: Figure showing the time-resolved $\Delta\Delta A$ traces for a) *Er*Cry WT, b) *Er*Cry W369F, c) *Gg*Cry WT, d) *Gg*Cry W369F, e) *Cl*Cry WT, and f) *Cl*Cry W369F. The fits, as described in the text, are shown.

Finally, comparing the wild type samples to the W369F mutants – shown in Fig. 4.17 – there is an approximate doubling of the ΔA from the W369F to their respective wild type samples. The time constants in the wild type proteins are all smaller than those in their respective W369F mutants, suggesting that there is a greater proportion of the geminate recombination evident therein.

The W369F mutants all showed substantial differences in their $\Delta\Delta A$ traces when compared to the wild type samples, with non-zero values over a longer temporal region, clearly evident in Fig. 4.18. This is in contrast to the magnetic field effect only being evident in the *Gg*Cry WT and *Cl*Cry WT samples for less than approximately the first microsecond. Noticeably different from all the other wild type samples was that of the migratory robin, *Er*Cry WT, which showed an initial increase over the first 5 µs before slowly decaying. This difference could point towards to the use of cryptochrome 4 as a magnetosensor in *Erithacus rubecula* as it shows both an effect that is sufficiently long-lived, but also decays to form its initial state to allow for further sensing.

4.5 Time-dependent B-half

Given the long-lived nature of the magnetic field effect in the avian W369F mutants, as well as the W394F mutant in *Dm*Cry, the magnetically altered reaction yield (MARY) of these samples could be monitored as a function of time after radical creation (i.e. photoexcitation). Previously Zollitsch noticed that $B_{1/2}$ – the parameter that marks the width of the Lorentzian shape of the MARY curve[5] – changed as a function of pump-probe delay time in both *Er*Cry W369F and *Dm*Cry W394F, but not in the wild type proteins [108]. There was, however, little interpretation given as to the origin of this phenomenon. Since there was a sequence error in the *Er*Cry W369F sample measured by Zollitsch, it was important to validate those findings by performing time-resolved MARY experiments. Furthermore, the W369F mutants of the non-migratory chicken and pigeon species could be studied and their MARY data investigated as a function of time.

Starting with *Er*Cry W369F, Fig. 4.19 shows the $\Delta\Delta A$ traces obtained as a function of field strength at pump-probe delay times ranging from 250 ns to 1 ms. The traces are shown on the same scale so as allow further comparison of the $\Delta\Delta A$ values with those obtained in the time-resolved experiments. None of the plots shows evidence of a low field effect (see Section 1.4), however this was not particularly explored as part of this work as there was not a concentration on the low-field region. All traces are, therefore, well modelled by a Lorentzian line-shape. This fitting allows for determination of the $B_{1/2}$ parameter, which describes the width of the Lorentzian curve. Consideration of the $\Delta\Delta A$ values at 30 mT as a function of pump-probe delay time yields qualitative agreement with those shown in Fig. 4.10, with an initial increase in the magnitude of $\Delta\Delta A$, before decaying with increasing time. By 1 µs the value of $\Delta\Delta A$ is approximately 30 % its original value. To allow for a more visual comparison of the changes in $B_{1/2}$, the normalised Lorentzian fits are shown in Fig. 4.19 h).

It is clear from this comparison that $B_{1/2}$ increases as a function of time, going from 3.55 ± 0.17 mT at 250 ns to 6.84 ± 0.80 mT at 1 ms. The early timescale value is rather close to the Weller-predicted 3 mT, suggesting that it is mostly hyperfine-driven. It is clear, however, that there are additional relaxation processes at play at later times that broaden the MARY trace. An hypothesis as to the occurrence here is that of singlet-triplet dephasing, following the ideas of Maeda *et al.*, which will be discussed below in Section 4.5.1 [61].

Similar behaviour is observed in *Gg*Cry W369F, shown in Fig. 4.20, with $\Delta\Delta A$ at 30 mT showing an approximately constant magnitude initially, before decaying to a constant value at later pump-probe delay times – again in good qualitative agreement with that seen in the time-resolved measurement (Fig. 4.12). Once again, fitting the traces with Lorentzians centred at the origin yields a clear trend of increasing $B_{1/2}$, ranging from 3.39 ± 0.28 mT at 250 ns to 6.85 ± 1.08 mT at 1 ms. These values are in agreement with those seen in *Er*Cry W369F, with the $B_{1/2}$ at 250 ns once again close to the Weller-predicted value.

[5] As described in Chapter 1.4, the $B_{1/2}$ parameter is the half-width at half-maximum of the Lorentzian in the normal MFE region, as shown in Fig. 1.4.

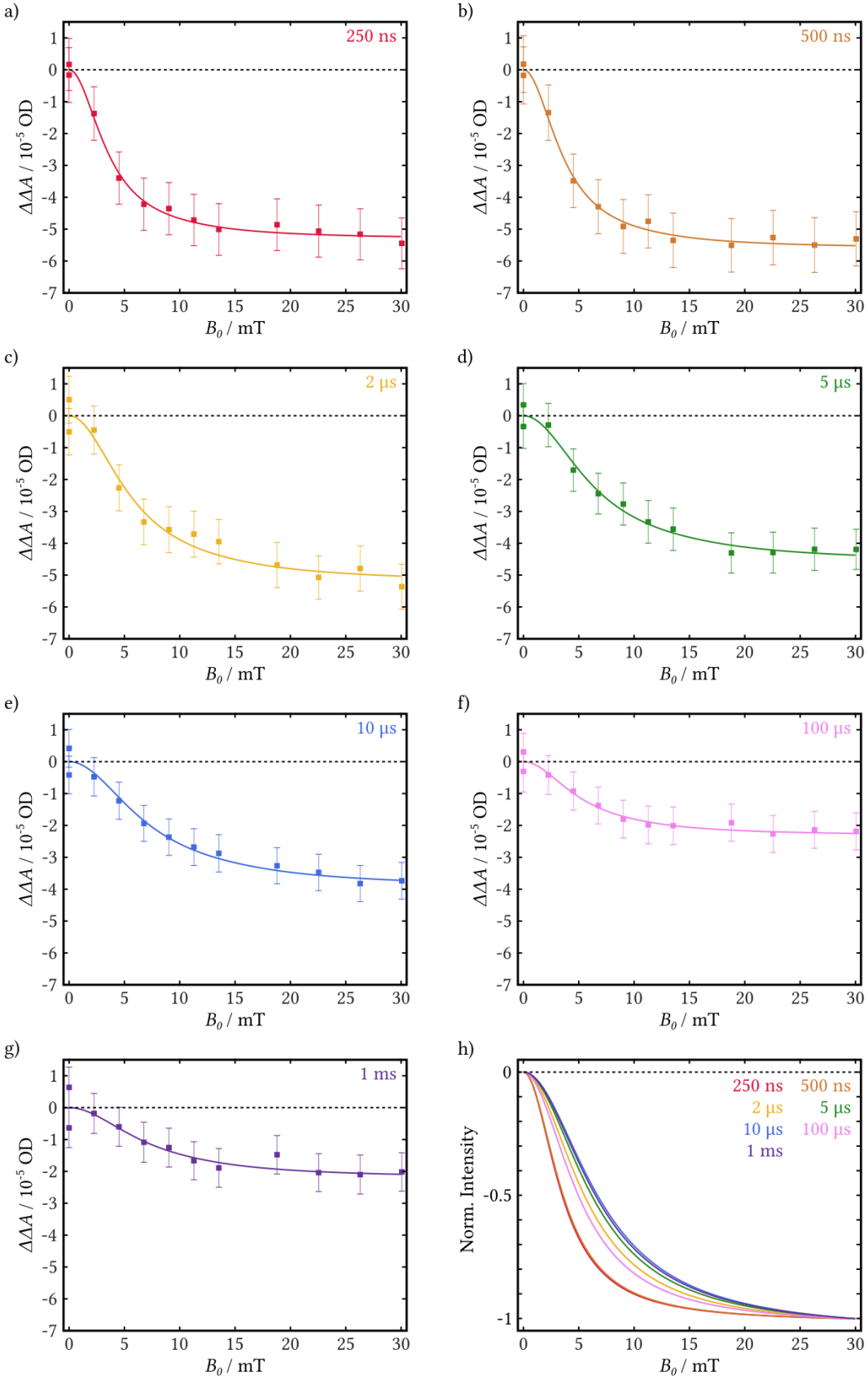


Figure 4.19: a)–g) MARY traces recorded on *Er*Cry W369F at 530 nm at various delay times following photoexcitation at 450 nm (300 µJ). The data are fit to a Lorentzian trace from which the $B_{1/2}$ parameter is obtained. h) The Lorentzian fits from panels a)–g) normalised to their values at 30 mT; colours are as for the other panels. There is a clear increase in the $B_{1/2}$ value with increasing pump-probe delay.

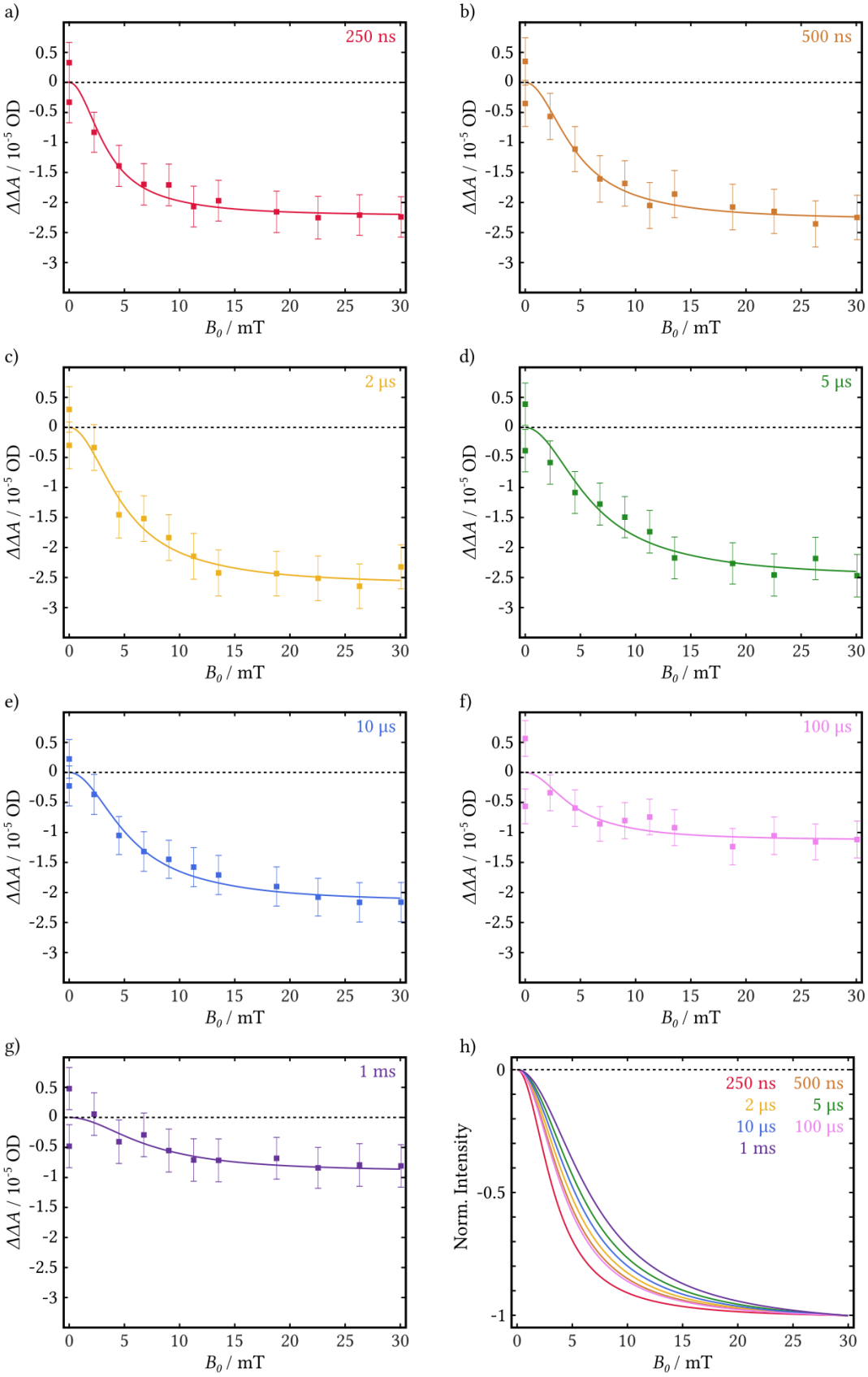


Figure 4.20: a)–g) MARY traces recorded on *Gg*Cry W369F at 530 nm at various delay times following photoexcitation at 450 nm (300 µJ). The data are fit to a Lorentzian trace from which the $B_{1/2}$ parameter is obtained. h) The Lorentzian fits from panels a)–g) normalised to their values at 30 mT; colours are as for the other panels. There is a clear increase in the $B_{1/2}$ value with increasing pump-probe delay.

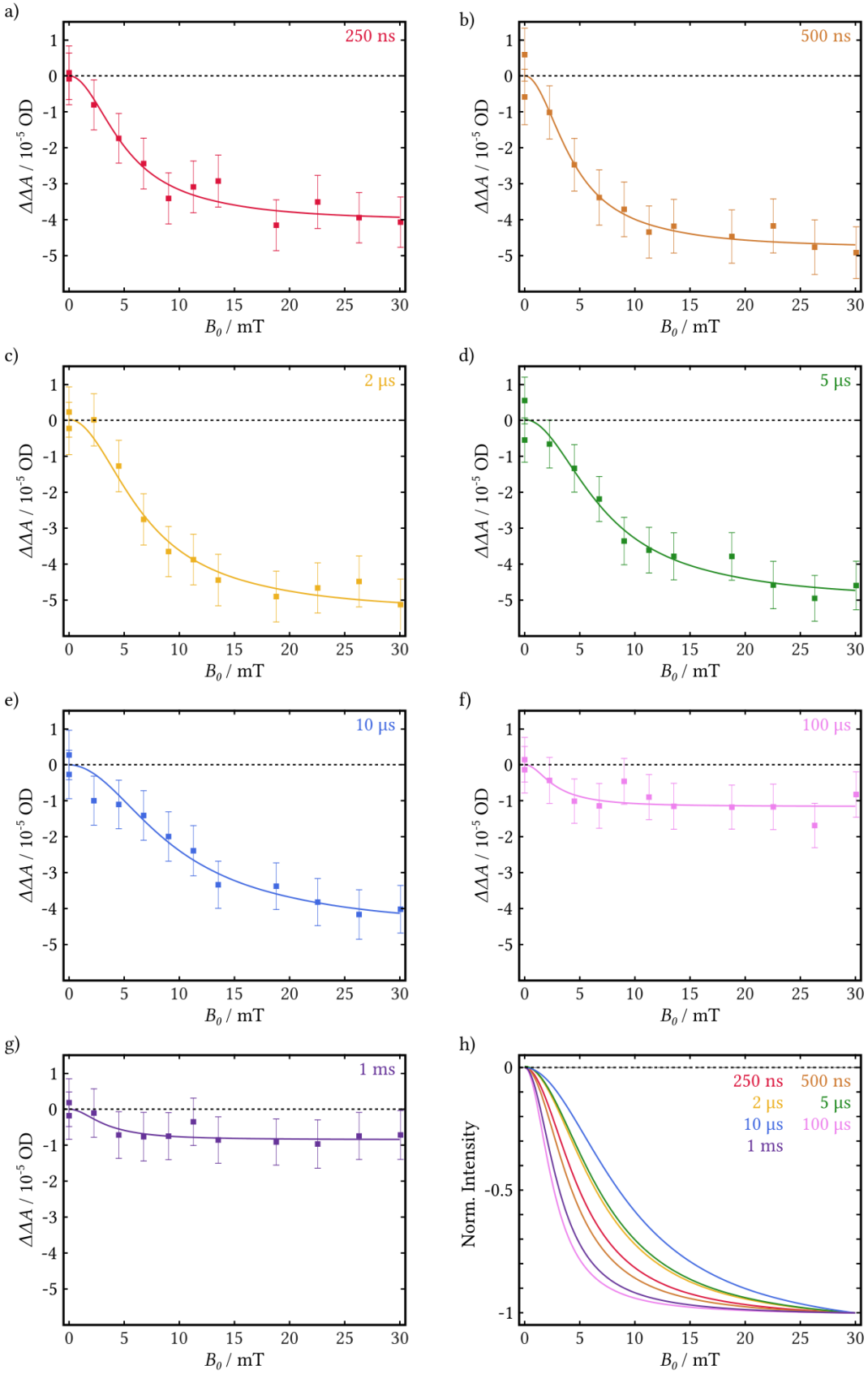


Figure 4.21: a)–g) MARY traces recorded on *Cl*Cry W369F at 530 nm at various delay times following photoexcitation at 450 nm (300 µJ). The data are fit to a Lorentzian trace from which the $B_{1/2}$ parameter is obtained. h) The Lorentzian fits from panels a)–g) normalised to their values at 30 mT; colours are as for the other panels. There is a clear increase in the $B_{1/2}$ value with increasing pump-probe delay.

Finally, the time-resolved MARY experiment was performed on *Cl*Cry W369F, the results of which are shown in Fig. 4.21. As expected and seen in the other W369F mutants, the magnitude of the $\Delta\Delta A$ signal at 30 mT initially increases slightly, before decreasing to the near-constant value seen in the time-resolved measurements (Fig. 4.14). In contrast to both *Er*Cry W369F and *Gg*Cry W369F, the $B_{1/2}$ value is much larger at 250 ns – 5.10 ± 0.62 mT, in comparison to approximately 3.5 mT in the other two measurements. There is still a general increase to 9.33 ± 1.03 mT at 10 µs, although the two larger pump-probe delay times yield $B_{1/2}$ values substantially smaller. This, much like the outlying fits of the 100 µs pump-probe delay $B_{1/2}$ values in *Er*Cry W369F and *Gg*Cry W369F, could be a result of insufficiently large a field, meaning that $\Delta\Delta A$ has not yet saturated, in contrast to the fits shown.

The $B_{1/2}$ values for all the species are shown both in Table 4.14 and represented graphically in Fig. 4.22.

	$B_{1/2}$ / mT		
PPD / µs	*Er*Cry W369F	*Gg*Cry W369F	*Cl*Cry W369F
0.25	3.55 ± 0.17	3.39 ± 0.28	5.10 ± 0.62
0.5	3.64 ± 0.18	4.50 ± 0.33	4.35 ± 0.28
2	5.70 ± 0.50	4.91 ± 0.46	6.75 ± 0.61
5	6.45 ± 0.37	5.97 ± 0.65	7.08 ± 0.53
10	7.05 ± 0.34	5.40 ± 0.44	9.33 ± 1.03
100	5.10 ± 0.33	4.31 ± 0.72	2.68 ± 1.26
1000	6.84 ± 0.80	6.85 ± 1.08	3.18 ± 1.17

Table 4.14: Table showing the fit-determined $B_{1/2}$ values obtained at various pump-probe delay times on *Er*Cry W369F, *Gg*Cry W369F, and *Cl*Cry W369F. Errors show 1 standard deviation, as determined by the fitting software, *Origin*. Fits to the data can be seen for each of the samples mentioned in Fig. 4.19, Fig. 4.20, and Fig. 4.21, respectively. Due to the small signal intensities at 100 µs and 1000 µs, the fits are slightly poorer, potentially leading to the outlying values seen in pink.

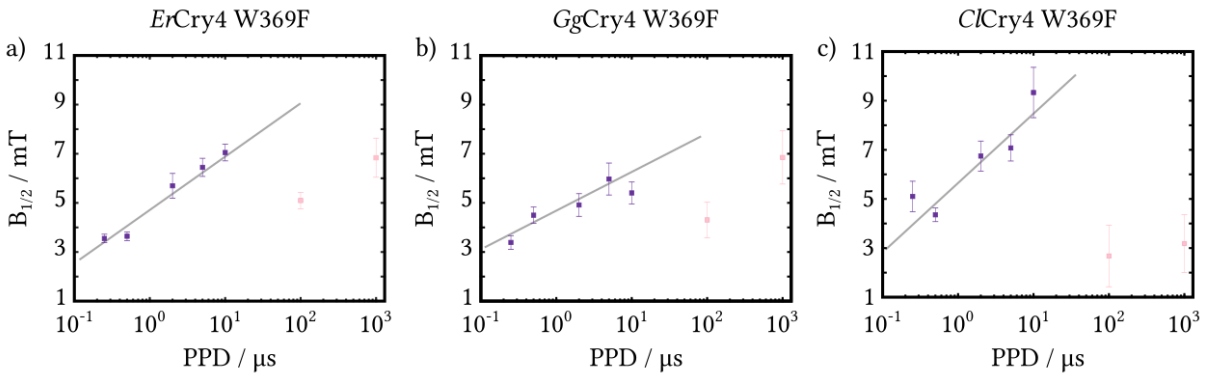


Figure 4.22: Traces showing the $B_{1/2}$ values obtained from time-resolved MARY measurements on a) *Er*Cry W369F, b) *Gg*Cry W369F, and c) *Cl*Cry W369F. The grey dashed lines are provided to guide the eye to the general trend seen. The outliers, most likely due to the small signal intensity, are shown in pink and are not factored into the guiding lines.

4.5.1 Exploring the Time-evolution of the $B_{1/2}$ Value

The time-evolution of the $B_{1/2}$ parameter, especially away from the Weller-predicted value, suggests that there are relaxation mechanisms at play. One such hypothesised mechanism is that of singlet-triplet dephasing, which is also explored in the interpretation by Maeda *et al.* for a system of 1 mM 2-methyl-1,4-naphthoquinone in a micellar solution of 80 mM sodium dodecyl sulphate [61]. This mechanism, proposed by Selby based on the measurements presented above, is chosen as it is the only relaxation mechanism that gives a time-dependent $B_{1/2}$ without dampening the magnetic field effect intensity [61, 143]. This mechanism is also suggested for cryptochrome 1 from thale cress (*Arabidopsis thaliana*, *At*Cry1) and *E. coli* photolyase (*Ec*PL) by Maeda *et al.*, where modulation of the exchange interaction is proposed through a reversible electron transfer between $\mathrm{Trp_B}$ and $\mathrm{Trp_C}$ [60].[6]

In order to better understand the role of singlet-triplet dephasing on the spin dynamics of a radical pair, Selby's "perturbation model" is discussed, going through a similar discussion. While an over-simplification, this model does provide some insight into a possible mechanism in the W369F mutants.

The model is based on a system comprised of two singly degenerate states, S (singlet) and T (triplet), that can be described by the spin Hamiltonian:

$$\hat{\mathbf{H}} = \frac{1}{2}\begin{pmatrix} \langle \mathrm{S}|\hat{H}_{\mathrm{Zee}}|\mathrm{S}\rangle & \langle \mathrm{S}|\hat{H}_{\mathrm{hf}}|\mathrm{T}\rangle \\ \langle \mathrm{T}|\hat{H}_{\mathrm{hf}}|\mathrm{S}\rangle & \langle \mathrm{T}|\hat{H}_{\mathrm{Zee}}|\mathrm{T}\rangle \end{pmatrix} = \frac{1}{2}\begin{pmatrix} \omega & q \\ q & \omega \end{pmatrix}, \tag{4.1}$$

where ω and q represent the Zeeman and hyperfine interactions, respectively. Furthermore, the master equation for the density operator is:

$$\frac{\mathrm{d}\hat{\boldsymbol{\rho}}}{\mathrm{d}t} = -\mathrm{i}\left[\hat{\mathbf{H}}, \hat{\boldsymbol{\rho}}\right] - k_{\mathrm{STD}}\left[\hat{\mathbf{P}}^{\mathrm{S}}\hat{\boldsymbol{\rho}}\hat{\mathbf{P}}^{\mathrm{T}} + \hat{\mathbf{P}}^{\mathrm{T}}\hat{\boldsymbol{\rho}}\hat{\mathbf{P}}^{\mathrm{S}}\right], \tag{4.2}$$

with k_{STD} the singlet-triplet dephasing rate constant and $\hat{P}^{\mathrm{S}}$ and $\hat{P}^{\mathrm{T}}$ the singlet and triplet projection operators, respectively.

The master equation can be rewritten as a Liouvillian:

$$\frac{\mathrm{d}\boldsymbol{\sigma}}{\mathrm{d}t} = -\mathbf{L}\boldsymbol{\sigma} \tag{4.3a}$$

$$= -\left[\mathrm{i}\left(\mathbf{H}\otimes\tilde{\mathbb{1}}_2 - \mathbb{1}_2\otimes\tilde{\mathbf{H}}\right) + k_{\mathrm{STD}}\left(\mathbf{P}^{\mathrm{S}}\otimes\tilde{\mathbf{P}}^{\mathrm{T}} + \mathbf{P}^{\mathrm{T}}\otimes\tilde{\mathbf{P}}^{\mathrm{S}}\right)\right]\boldsymbol{\sigma} \tag{4.3b}$$

$$= \frac{1}{2}\begin{pmatrix} 0 & -\mathrm{i}q & \mathrm{i}q & 0 \\ -\mathrm{i}q & 2(k_{\mathrm{STD}}+\mathrm{i}\omega) & 0 & \mathrm{i}q \\ \mathrm{i}q & 0 & 2(k_{\mathrm{STD}}-\mathrm{i}\omega) & -\mathrm{i}q \\ 0 & \mathrm{i}q & -\mathrm{i}q & 0 \end{pmatrix}\begin{pmatrix} \rho_{\mathrm{SS}} \\ \rho_{\mathrm{ST}} \\ \rho_{\mathrm{TS}} \\ \rho_{\mathrm{TT}} \end{pmatrix}, \tag{4.3c}$$

[6] Both *At*Cry1 and *Ec*PL have only a triad of tryptophans, in contrast to the wild type proteins in this work [90, 134].

where $\mathbb{1}_2$ is the two-dimensional identity matrix, ρ_{ij} is the density of the coherence between states i and j, the tilde represents the matrix transpose,[7] and:

$$\mathbf{P}^{\mathrm{S}} = \begin{pmatrix} 1 & 0 \\ 0 & 0 \end{pmatrix} \quad \text{and} \quad \mathbf{P}^{\mathrm{T}} = \begin{pmatrix} 0 & 0 \\ 0 & 1 \end{pmatrix}. \tag{4.4}$$

Changing the basis, an alternative density vector, $\boldsymbol{\sigma}'$, can be defined as:

$$\boldsymbol{\sigma}' = \begin{pmatrix} \rho_{\mathrm{ST}} + \rho_{\mathrm{TS}} \\ -\mathrm{i}(\rho_{\mathrm{ST}} - \rho_{\mathrm{TS}}) \\ \rho_{\mathrm{SS}} - \rho_{\mathrm{TT}} \\ \rho_{\mathrm{SS}} + \rho_{\mathrm{TT}} \end{pmatrix} = \begin{pmatrix} 0 & 1 & 1 & 0 \\ 0 & -\mathrm{i} & \mathrm{i} & 0 \\ 1 & 0 & 0 & -1 \\ 1 & 0 & 0 & 1 \end{pmatrix} \begin{pmatrix} \rho_{\mathrm{SS}} \\ \rho_{\mathrm{ST}} \\ \rho_{\mathrm{TS}} \\ \rho_{\mathrm{TT}} \end{pmatrix} = \mathbf{A}\boldsymbol{\sigma}, \tag{4.5}$$

enabling the rewriting of the master equation (Eqn 4.3b) as:

$$\frac{\mathrm{d}\boldsymbol{\sigma}'}{\mathrm{d}t} = -\mathbf{A}\mathbf{L}\mathbf{A}^{-1}\boldsymbol{\sigma}' = -\begin{pmatrix} k_{\mathrm{STD}} & -\omega & 0 & 0 \\ \omega & k_{\mathrm{STD}} & -q & 0 \\ 0 & q & 0 & 0 \\ 0 & 0 & 0 & 0 \end{pmatrix} \boldsymbol{\sigma}'. \tag{4.6}$$

Knowing that $\rho_{\mathrm{SS}} + \rho_{\mathrm{TT}} = 1$ allows us to reduce the number of elements in $\boldsymbol{\sigma}'$:

$$\boldsymbol{\sigma}' \longrightarrow \mathbf{p} = \begin{pmatrix} \rho_{\mathrm{ST}} + \rho_{\mathrm{TS}} \\ -\mathrm{i}(\rho_{\mathrm{ST}} - \rho_{\mathrm{TS}}) \\ \rho_{\mathrm{SS}} - \rho_{\mathrm{TT}} \end{pmatrix} \tag{4.7}$$

meaning that the master equation is:

$$\frac{\mathrm{d}\mathbf{p}}{\mathrm{d}t} = -\mathbf{K}\mathbf{p}, \tag{4.8}$$

with solution

$$\mathbf{p}(t) = \exp(-\mathbf{K}t)\,\mathbf{p}(0), \tag{4.9}$$

with:

$$\mathbf{K} = \mathbf{M} + \mathbf{Q} = \begin{pmatrix} k_{\mathrm{STD}} & -\omega & 0 \\ \omega & k_{\mathrm{STD}} & 0 \\ 0 & 0 & 0 \end{pmatrix} + \begin{pmatrix} 0 & 0 & 0 \\ 0 & 0 & -q \\ 0 & q & 0 \end{pmatrix}. \tag{4.10}$$

[7] The tilde is chosen over the more commonly used $\mathbf{M}^{\mathrm{T}}$ notation to avoid confusion with the triplet operators.

Separation of **K** into these two components, the first comprising the Zeeman and singlet-triplet dephasing and the second the hyperfine interaction, allows for the hyperfine component to perturb the system if $q^2 \ll \omega^2 + k_{\mathrm{STD}}^2$, which is the case for the large field strengths used in this work.

Solving first for the eigenvalues of **M** yields:

$$y_1^0 = 0, \quad y_2^0 = k_{\mathrm{STD}} - \mathrm{i}\omega, \quad \text{and} \quad y_3^0 = k_{\mathrm{STD}} + \mathrm{i}\omega, \tag{4.11}$$

with matrix of eigenvectors:

$$\mathbf{V}_0 = \begin{pmatrix} 0 & \frac{-\mathrm{i}}{\sqrt{2}} & \frac{\mathrm{i}}{\sqrt{2}} \\ 0 & \frac{1}{\sqrt{2}} & \frac{1}{\sqrt{2}} \\ 1 & 0 & 0 \end{pmatrix}. \tag{4.12}$$

Treating **Q** as a perturbation, the eigenvalues of **K** to second order in q are [43]:

$$y_i = y_i^0 + \sum_{j \neq i} \frac{Q'_{ji} Q'_{ij}}{y_i^0 - y_j^0}, \tag{4.13}$$

where $\mathbf{Q}' = \mathbf{V}_\mathbf{0}^\dagger \mathbf{Q} \mathbf{V}_\mathbf{0}$, giving:

$$\begin{aligned} y_1 &= k_{\mathrm{STD}} \Omega^2, \\ y_2 &= (k_{\mathrm{STD}} - \mathrm{i}\omega) - \frac{1}{2}\Omega^2 (k_{\mathrm{STD}} + \mathrm{i}\omega), \text{ and} \\ y_3 &= (k_{\mathrm{STD}} + \mathrm{i}\omega) - \frac{1}{2}\Omega^2 (k_{\mathrm{STD}} - \mathrm{i}\omega), \end{aligned} \tag{4.14}$$

with $\Omega^2 = \frac{q^2}{k_{\mathrm{STD}}^2 + \omega^2}$. The eigenvectors of **K** to first order in q are given by:

$$V_i = V_{0i} + \sum_{j \neq i} \left(\frac{Q'_{ji}}{y_i^0 - y_j^0} \right) V_{0j}, \tag{4.15}$$

yielding:

$$\mathbf{V} = \begin{pmatrix} \frac{\omega \Omega^2}{q} & -\frac{\mathrm{i}}{\sqrt{2}} & \frac{\mathrm{i}}{\sqrt{2}} \\ \frac{k_{\mathrm{STD}} \Omega^2}{q} & \frac{1}{\sqrt{2}} & \frac{1}{\sqrt{2}} \\ 1 & \frac{\Omega^2 (k_{\mathrm{STD}} + \mathrm{i}\omega)}{\sqrt{2} q} & \frac{\Omega^2 (k_{\mathrm{STD}} - \mathrm{i}\omega)}{\sqrt{2} q} \end{pmatrix}. \tag{4.16}$$

Using the solution given in Eqn 4.9 under the perturbation:

$$\mathbf{p}(t) \approx \mathbf{V}^{\dagger} \exp(-\mathbf{y}t)\,\mathbf{V}\mathbf{p}(0), \tag{4.17}$$

where $\mathbf{y}$ is the diagonal matrix of the perturbed eigenvalues and:

$$\mathbf{p}(0) = \begin{pmatrix} 0 \\ 0 \\ 1 \end{pmatrix}, \tag{4.18}$$

since the radical pairs in the W369F mutants is formed in a pure singlet state ($\rho_{SS} = 1, \rho_{ST}, \rho_{TS}, \rho_{TT} = 0$).

Considering now the third element of this modified density vector, $p_3(t)$, which is the difference between the singlet and triplet populations yields:

$$p_3(t) = \rho_{SS}(t) - \rho_{TT}(t) \approx \exp\left(-\Omega^2 k_{STD} t\right) + \Omega^2 \cos\left(\omega t + \frac{1}{2}\Omega^2 \omega t\right) \exp\left(-k_{STD} t + \frac{1}{2}\Omega^2 \omega t\right), \tag{4.19}$$

which can be simplified to:

$$\rho_{SS}(t) - \rho_{TT}(t) \approx \exp\left(-\Omega^2 k_{STD} t\right) + \Omega^2 \cos(\omega t) \exp(-k_{STD} t), \tag{4.20}$$

since $\Omega^2 \ll 1$. Using the condition that $\rho_{SS}(t) + \rho_{TT}(t) = 1$, the singlet spin density is given by:

$$\rho_{SS} \approx \frac{1}{2} + \frac{1}{2}\left[\exp\left(-k_{STD}\Omega^2 t\right) + \Omega^2 \cos(\omega t) \exp(-k_{STD} t)\right]. \tag{4.21}$$

The singlet density as a function of time, shown in Fig. 4.23 for $q = 1 \times 10^6\ s^{-1}$ (the perturbation by the hyperfine interaction), $\omega = 6 \times 10^6\ s^{-1}$, and $k_{STD} = 0.2 \times 10^6\ s^{-1}$, such that $\Omega^2 = 0.028$; the singlet density is also plotted (blue) in the absence of singlet-triplet dephasing, *viz.* $k_{STD} = 0$. It is immediately evident that, in the absence of singlet-triplet dephasing, the singlet spin density remains very close to 1. This is unsurprising as ω, which represents the Zeeman interaction, is large in comparison to the hyperfine interaction and, therefore, prevents the interconversion to the triplet state. The model also does not account for recombination to the ground state or formation of the secondary radical pair.

From Fig. 4.23 it is clear that singlet-triplet dephasing dampens the oscillations between the singlet and triplet states with rate constant k_{STD} and relaxes the system towards $\rho_{SS}(t) = \frac{1}{2}$ with a rate constant $k_{STD}\Omega^2$ by removing coherences as soon as they are formed.

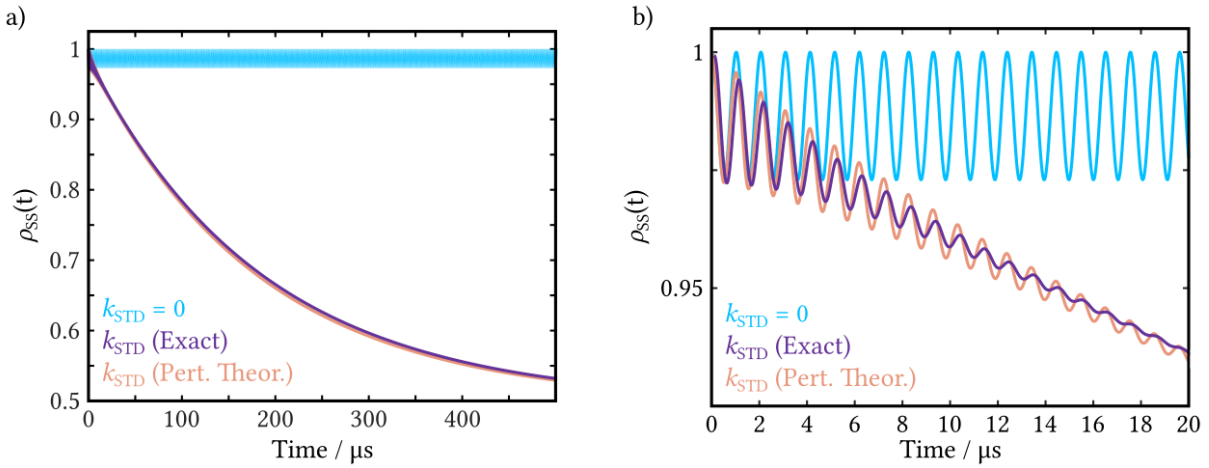


Figure 4.23: Plots showing the singlet populations, $\rho_{SS}(t)$ under the perturbation model in Section 4.5.1 with $q = 1 \times 10^6\,\mathrm{s}^{-1}$ (hyperfine interactions) and $\omega = 6 \times 10^6\,\mathrm{s}^{-1}$ (Zeeman effect). Blue shows the exact solution to Eqn 4.8 in the absence of singlet-triplet dephasing ($k_{STD} = 0$), purple has the exact solution with singlet-triplet dephasing ($k_{STD} = 0.2{\times}10^6\,\mathrm{s}^{-1}$). The pink trace shows the second-order perturbation solution (Eqn 4.19), which is in reasonable agreement with that shown in purple and, therefore, used as an approximation.

Modelling recombination of the radical pairs formed using an exponential model with rate constant k, the singlet yield, Φ_S, is given by [144]:

$$\Phi_S(\omega, t) = k \int_0^t \rho_{SS}(t) \exp(-kt)\,\mathrm{d}t. \tag{4.22}$$

Using the approximation for ρ_{SS} in Eqn 4.21, dropping the rapidly decaying term $(\Omega^2 \cos(\omega t)\exp(-k_{STD}t))$ allows for conversion of the singlet yield to:

$$\Phi_S(\omega, t) = \frac{k}{2} \int_0^t \left[1 + \exp\left(-k_{STD}\Omega^2 t\right)\right] \exp(-kt)\,\mathrm{d}t \tag{4.23a}$$

$$= \frac{1}{2}\left[1 - \mathrm{e}^{-kt} + \left(\frac{k}{k + k_{STD}\Omega^2}\right)\left(1 - \mathrm{e}^{-(k+k_{STD}\Omega^2)t}\right)\right]. \tag{4.23b}$$

Using the parameters above (as used for Fig. 4.23) and $k = 0.01 \times 10^6\,\mathrm{s}^{-1}$, i.e. singlet-triplet dephasing is faster than recombination,[8] one can plot the singlet yield for various times following creation as a function of applied magnetic field, ω, shown in Fig. 4.24 a). The dependence of $B_{1/2}$ on time is made even clearer by subtracting the zero-field value and dividing by $(1-\mathrm{e}^{-kt})$,[9] which can then be normalised to its high-field value. These are shown in Fig. 4.24 b) and c), respectively.

While the values chosen to represent the various parameters in the above model are not precise, they are qualitatively and comparatively in agreement with that seen above in the

[8] Singlet-triplet dephasing would not be evident if it was slower than recombination.

[9] The divisor is chosen as a result of the exponential model which, as Selby states, has the time-dependence of $B_{1/2}$ as: $B_{1/2}(t) = q\sqrt{\frac{k_{STD}}{k}}\left(1-\mathrm{e}^{-kt}\right)$ [143].

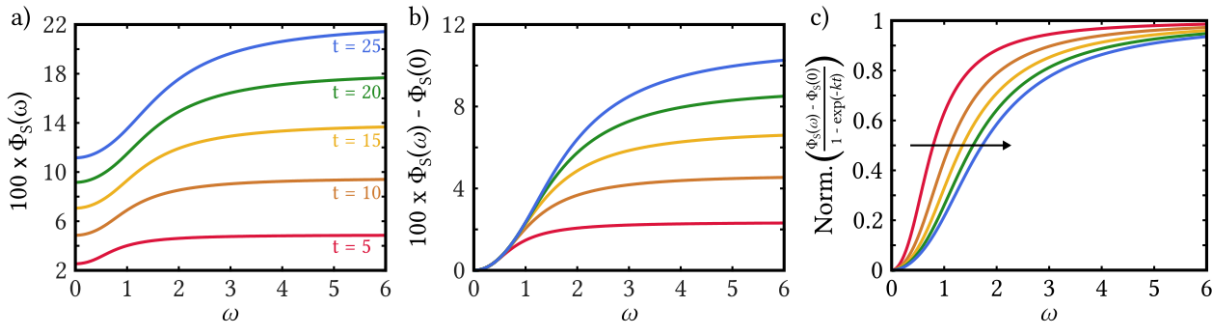


Figure 4.24: Simulations showing the effect of a magnetic field (ω, in frequency units) on the singlet yield, Φ_S, under the exponential model alongside singlet-triplet dephasing. The traces show the increase in the $B_{1/2}$ parameter as a function of time going from t = 5 (red) to t = 25 (blue). a) Singlet yield as a function of magnetic field. b) Same plot as a), but with the zero-field offset subtracted from the singlet yield. c) Plots as in b) divided by their decay and then normalised, showing a clear increase in the $B_{1/2}$ with increasing time.

experiments and proposed by Xu *et al.* [100]. Firstly, the Zeeman effect is much larger than the hyperfine contribution – certainly true at B_0 = 30 mT. The effect of singlet-triplet dephasing is small in comparison to these effects too, as well as being faster than recombination, else it would not be seen on the timescale of the measurements performed. This model, therefore, provides a good proof-of-principle example of how the magnitude of $B_{1/2}$ could increase as a function of pump-probe delay time.

4.6 Further Considerations

In trying to elucidate the physical origins of the magnetic sense, here in cryptochromes, a number of questions arise. The most obvious of these questions is the biological relevance of the measurements undertaken here given that they are, not least, performed *in vitro*. The conditions chosen – pH 8 at 5 °C – should closely match the physiological conditions of avian cells (pH 7.3 and 40–43 °C). This is because the drop in temperature shifts the acid-base equilibrium, particularly that of the histidine side-chains, which can then be reversed by an increase in the pH to more closely match that of physiological pH [145, 146].

Additionally, the use of $K_3Fe(CN)_6$ as a reoxidant may shift the redox conditions. In order to assess this, an experiment at a single pump-probe delay 2 µs was performed on a sample that showed good photostability and a large magnetic field effect – *Er*Cry W369F – in the absence of the ferricyanide reoxidant. Given that $K_3Fe(CN)_6$ is used to speed up the recovery time and, thus, reduce the waiting times in between averages, this experiment was performed over an extended period of time (approx. 12.5 h) with a 5 min wait in between each on-off couplet. This was then compared to a time-resolved experiment that used $K_3Fe(CN)_6$, for which the data from the same pump-probe delay were taken, albeit with a much shorter approximately 1 min

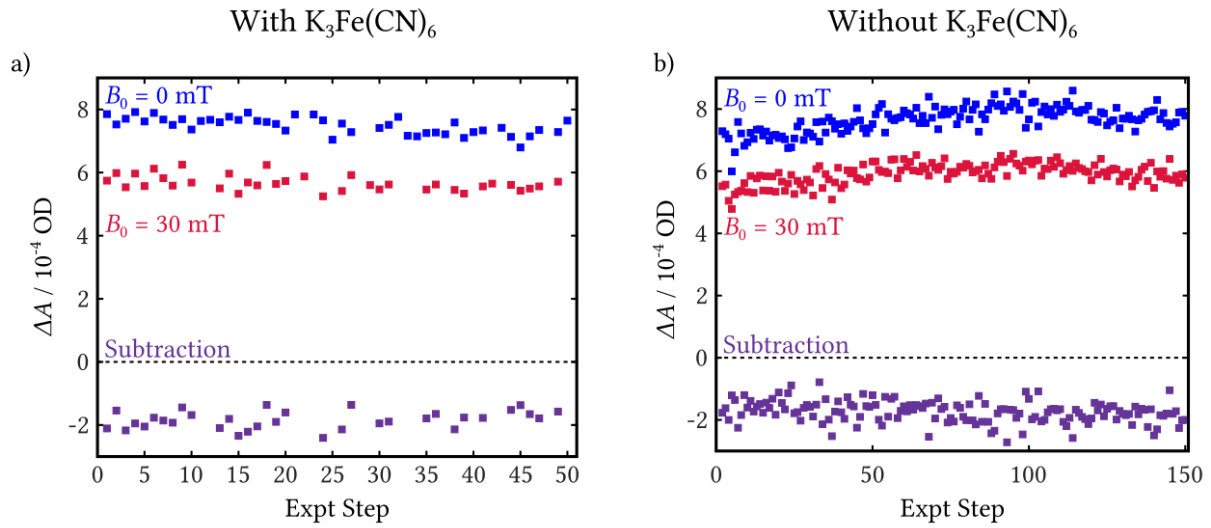


Figure 4.25: Plots showing the impact of $K_3Fe(CN)_6$ on the magnetic field effect of *Er*Cry W369F. ΔA in the presence (red) and absence (blue) of a 30 mT magnetic field recorded at 530 nm 2 µs after photoexcitation (450 nm, 300 µJ). The subtraction, *viz.* $\Delta A_{B=30\,\mathrm{mT}} - \Delta A_{B=0\,\mathrm{mT}}$, is shown in purple. a) Measurement performed on *Er*Cry W369F in buffer solution containing 5 mM $K_3Fe(CN)_6$. The data are taken from a time-resolved measurement. b) Measurement performed on *Er*Cry W369F in buffer solution *without* $K_3Fe(CN)_6$. The on-off couplets are taken at 5 min intervals.

wait between measurements.[10] The data from the experiments with and without $K_3Fe(CN)_6$ are shown in Fig. 4.25 a) and b), respectively.

It is immediately clear that $K_3Fe(CN)_6$ makes no difference to the measurement of the magnetic field effect, which takes values of 24.5 ± 3.7 % with $K_3Fe(CN)_6$ and 22.7 ± 4.5 % without (both one standard deviation). Unfortunately it was not possible to obtain similar measurements on any *Er*Cry WT samples.

Also noticeable in Fig. 4.25 a) is the slight decrease in $\Delta A(B = 0)$ over the course of the experiment, in contrast to the increase in panel b), while not affecting the $\Delta\Delta A$ value. This slowly decreasing ΔA value was also confirmed from the broadband cavity-enhanced absorption spectrometer and was only seen in samples that contained $K_3Fe(CN)_6$, suggesting that it may be an artefact of the reoxidant.[11]

To further investigate this phenomenon, a time-resolved measurement was performed on pure $K_3Fe(CN)_6$ (5 mM) in water with pump-probe delay times ranging from 500 ns to 1 ms. The data from this measurement are shown in Fig. 4.26. In contrast to normal time-resolved measurements, the pump laser was turned off for averages 51–150; the averages with photoexcitation are shaded in blue for clarity.

[10] The delay between shots could vary from 60–90 s as a result of the randomised pump-probe delay times in the time-resolved measurements.
[11] Broadband cavity-enhanced measurements were performed by Patrick Murton.

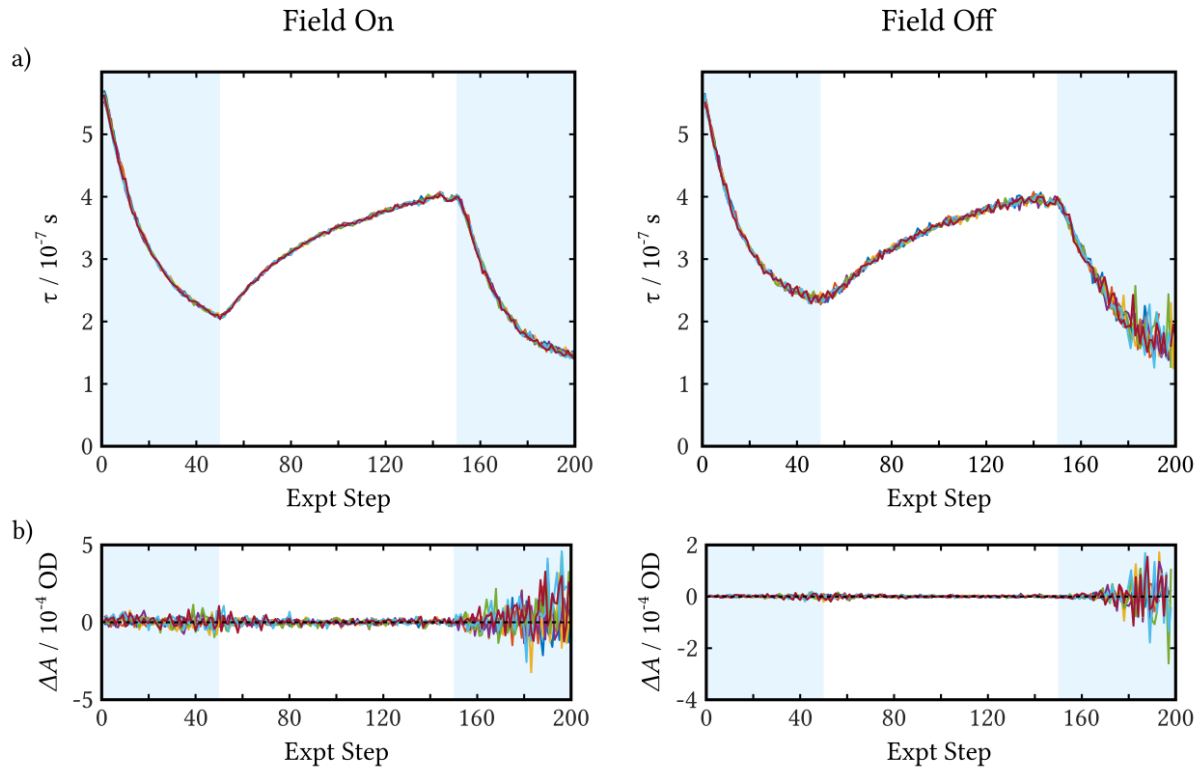


Figure 4.26: Plots showing the specialised time-resolved measurement on 5 mM $K_3Fe(CN)_6$ in water recorded at 530 nm at various delay times following photoexcitation at 450 nm (300 µJ). The pump laser was used for averages 1–50 and 151–200 (shaded blue) and was shuttered for averages 51–150. The left plots show the results in the presence of a 30 mT magnetic field, while the right plots show the results in the absence of an external field. a) Ring-down times over the course of the experiment at various pump-probe delay times. b) ΔA values over the course of the experiment.

From the data it is clear that photoexcitation leads to the formation of a photoproduct that exhibits a photoinduced absorbance at 530 nm as the ring-down time, τ, shows a clear decrease and increase in the presence and absence of photoexcitation, respectively. This increase in ring-down time suggests that the species formed does return back to the ground state, although at a slower rate than it is formed in the experimental protocol described here. In both the presence and absence of a magnetic field, the ΔA value is zero (as evident in Fig. 4.26). This does, however, breathe confidence into the fact that $K_3Fe(CN)_6$ does not influence the cryptochrome measurements shown above, especially due to the wait times used that would allow for the species causing the photoinduced absorbance to return back to $K_3Fe(CN)_6$. One study suggests that the species responsible for the additional absorption is $Fe^{II}(CN)_5(H_2O)$, formed by metal-ligand dissociation (losing a $CN^{\bullet}$ radical) and solvation [147]. Given the strong absorption band of $K_3Fe(CN)_6$ centred at 420 nm, the absorption at 450 nm is certainly non-negligible and is, in fact, close to four orders of magnitude larger than FAD. $K_3Fe(CN)_6$ is, therefore, likely to undergo photochemical processes when excited alongside the cryptochrome samples [148–150].

The final *in vitro* consideration here is the ability of the receptor – in this case cryptochrome – to return back to its initial state after sensing or be replenished so that it can sense again [100]. Given that cryptochromes are bound, the latter is not possible, meaning that the photocycle must allow reoxidation to the fully oxidised state over a short period of time [99]. As shown by Xu *et al.*, excitation of all three of the wild type proteins in the absence of reoxidants and *in vitro* showed recycling times on the order of minutes. Measurements under reducing conditions (5 mM dithiothreitol) showed an increase to approximately 5 h at 25 °C and 1 h at 40 °C – closer to the physiological temperature. While the environment of the cell is uncertain at present, these measurements do suggest that it may be possible for cryptochromes to act as a magnetoreceptor.

The downstream signalling pathway is still debated, but may make use of the C-terminal tail [109–113]. It is important to note that it may not be the cryptochrome component of the signalling pathway that is optimised for magnetoreception, but rather the downstream processes which may include receptor alignment, amplification mechanisms, or enhanced neural processing [31, 100, 151, 152].

Another optimisation technique used by nature may be to incorporate a high yield of the radical pair at large enough distances so as to slow the recombination, but short enough distances to allow singlet-triplet mixing that could then generate magnetic field effects as necessary. One hypothesis proposed by Xu *et al.* is the formation of a composite radical pair, in which there is a rapid equilibrium between the radical pairs formed with the tryptophan component on either Trp_D or Trp_C [100]. Evidence for or against this hypothesis is not provided in this work. As seen above, the magnetic field effect formed through Trp_C (in the W369F mutants) is greater than that seen in the wild type proteins. This could be because W369 is closer to the surface of the protein structure, enabling more efficient deprotonation from a nearby residue (such as C317) or reduction (from nearby Y319, for example) to form a stabilised radical pair that could then act as the signalling state [101]. Within the hypothesis of a rapid equilibrium, the back electron transfer to Trp_C might then increase the magnetic field effect, allowing for a larger initial signal in the signalling cascade.

It is worth saying that the changes in radical concentration as a result of the large fields used are substantially larger than those experienced naturally with the 50 μT geomagnetic field. Unfortunately it is not yet possible to measure Earth-strength magnetic field effects in cryptochromes and, considering also the incredibly small changes in absorption expected from such small magnetic fields, such measurements would lead to increased optical challenges of improving sensitivity to be able to measure these – and that is before considering the challenges of anisotropy, which would also be important to show if cryptochromes do, in fact, act as a compass.

4.7 Conclusion

In this chapter the rebuilt cavity ring-down spectrometer has been used to measure wild type cryptochromes and their W369F mutants from three avian species: the migratory European robin (*Erithacus rubecula*); the non-migratory, but magnetic field-using pigeon (*Columba livia*); and the non-migratory and non-magnetically inclined chicken (*Gallus gallus*). Time-resolved measurements performed on the wild type proteins yielded a long-lived (>10 µs) magnetic field effect in *Er*Cry WT, in stark contrast to the sub-microsecond effect in both *Cl*Cry WT and *Gg*Cry WT. Time-resolved measurements performed on the W369F mutants showed approximately half the concentration of radical species of their wild type proteins, but yielded stronger and, in all cases, long-lived magnetic field effects (>1 ms). The magnetic field effect seen in *Er*Cry WT was markedly different from all the other samples measured, suggesting that there may be some evolutionary change that allows it to better act as a magnetosensor.

With their large magnetic field effects and photostability, time-resolved MARY experiments were run on the three W369F mutants. In all three cases the $B_{1/2}$ value increased with increasing pump-probe delay time. Singlet-triplet dephasing was suggested as the cause for this increasing $B_{1/2}$ with a "perturbation model", introduced by Selby as a result of the measurements in this work, used to demonstrate the effect.

Finally, the role of the measurements presented here in elucidating the physical origins of the avian magnetic sense were discussed, including the role of $K_3Fe(CN)_6$ and the presence of a photoinduced absorbance, most likely as a result of $Fe(CN)_5(H_2O)$.

To conclude, this chapter shows the first magnetic field effect measurements comparing cryptochromes from migratory and non-migratory species using cavity ring-down spectroscopy, as well as the effect of a point mutation in the electron transfer chain. The (wild type) migratory species showed a markedly different magnetic field effect, which supports the hypothesis that cryptochrome 4 may be involved in the magnetosensing process in migratory birds.

Chapter 5

Conclusions and Outlook

5.1 Conclusions

Chapter 1 introduced the area of research, commencing with a discussion of the role of magnetoreception in biology. The two main hypotheses currently used to explain the use of magnetic fields in avian navigation – the magnetite and cryptochrome hypotheses – were outlined. It was furthermore demonstrated that the latter hypothesis is generally considered the front-runner in this debate following a number of crucial spectroscopic and zoological observations. Concentrating on the cryptochrome hypothesis for the remainder of the thesis, the main concepts required within the field of spin chemistry were introduced. Here the radical pair mechanism, which is at the heart of all radical pair reactions, took centre stage. As animals possess a magnetic compass that is sensitive to both the strength and *direction* of applied magnetic fields, the importance of anisotropic magnetic field effects was also given closer inspection.

Chapter 2 focussed on optical spectroscopy and optical cavities were introduced. The principle of cavity ring-down spectroscopy was discussed and the analysis procedure for such measurements shown, particularly converting ring-down traces to changes in absorbance and the desired magnetic field effect, which was evident in $\Delta\Delta A$. The experimental techniques possible on the cavity ring-down spectrometer were introduced before the rebuilt apparatus was shown. This was followed by a pseudocode-led discussion of the recoding of the instrument, which is much improved from previous iterations – especially in that it no longer requires constant user supervision during measurements. Finally, the role of the cavity ring-down experiment in understanding the magnetic field effects in biological systems was explored, comparing and contrasting it to the other techniques employed to understand such phenomena. This highlighted the important role that CRDS has in understanding magnetic field effects.

Testing of the rebuilt spectrometer was performed using a well-studied model system – flavin mononucleotide (FMN) and hen egg-white lysozyme (HEWL) – the results of which were

presented in Chapter 3. The photochemistry of the FMN/HEWL system was introduced before time-resolved, magnetically altered reaction yield (MARY), and time- and wavelength-resolved experiments performed and the results compared to those seen previously, particularly by Dr D. Sheppard [127]. The results were in good agreement with those previously reported. The sensitivity and stability of the spectrometer made it possible to monitor the effect of storage conditions of the laboratory's "calibration sample" (used by all spectroscopists in the group) on its optical properties. Storage of HEWL at 4 °C, as sometimes employed by the group, led to a slight bathochromic shift in the time- and wavelength-resolved measurements and an initial rise in the radical concentrations (measured at 530 nm), in stark contrast to previous measurements. With the addition of a photodetector to measure the pump laser power, experiments were undertaken to assess whether a correction could be made for the differences seen as a result of fluctuation in photoexcitation power. Results suggested that there are factors other than the pump laser power that contribute more significantly to the fluctuation in the ring-down time, τ, and that it was, therefore, not necessary to consider the pump power for the measurements on more biologically relevant samples.

Having shown that the rebuilt cavity ring-down spectrometer was working successfully, an investigation into cryptochrome 4 – the hypothesised magnetoreceptor in avian species – was undertaken, presented in Chapter 4. An introduction to the system was given, including a phylogenetic analysis and sequence comparison of the species and proteins of interest, respectively, before the protocols for expression and preparation of the samples were discussed. Measurements were first performed on the wild type proteins, the results of which showed a marked difference between the migratory *Erithacus rubecula* and the other two species. The magnetic field effect in the sample from the robin was long-lived – substantially longer than the 1 µs hypothesised to be needed for use as a magnetosensor – and was seen to grow in on the timescale of the experiments performed. This is in contrast to the other species which only showed decays, both within 1 µs. Time-resolved measurements were also performed on the W369F mutants of cryptochrome 4, in which the final tryptophan in the electron transfer cascade was replaced with phenylalanine, this latter residue being unable to perform the same function. The mutants of all three species showed substantially larger magnetic field effects than their respective wild type proteins, with all of these effects being evident at times longer than a millisecond.

Further measurements were performed on the W369F mutants, looking at the temporal evolution of the $B_{1/2}$ parameter, which characterises the width of the MARY curves. In the mutants of all three species, $B_{1/2}$ increased as a function of pump-probe delay time, suggesting that there are additional relaxation mechanisms at play. Theory proposed as a result of the work in this thesis suggests that singlet-triplet dephasing may be the cause of the broadening of the Lorentzian line-shape of the MARY traces. This theory was further explored using a perturbation model with theoretical results showing similarities to those obtained experimentally.

A few experimental considerations were further explored, most notably the role of the reoxidant used in measurements – $K_3Fe(CN)_6$. Two further measurements were performed to assess this, the first being of a cryptochrome sample (*Er*Cry W369F) being measured in the absence of the reoxidant and compared to a measurement in the presence thereof, and the second being a time-resolved experiment of pure $K_3Fe(CN)_6$ in H_2O. In the former, there was no difference between the two measurements, suggesting that Fe(III) only acts to speed up reoxidation without affecting the results of the experiment. In the pure-$K_3Fe(CN)_6$ measurement, a clear photoinduced absorbance was detected. The contributing species, however, did not exhibit a magnetic field effect, reaffirming that Fe(III) simply acts as a reoxidant. Finally, a brief discussion of the validity of the *in vitro* measurements performed in this work were explored in the context of understanding animal magnetoreception. Although many things are unknown about such processes, the considerations taken into account in this work aim to most closely resemble that seen *in vivo* and these measurements, therefore, allow more to be gleaned in the further elucidation of the physical origins of the animal magnetic sense.

5.2 Future Work and Outlook

While this work has uncovered many new facets in the study of animal magnetoreception, it only scrapes the surface of the wealth of information required to fully understand the biological processes that underpin such a magnetic sense. Performing measurements on further specifically chosen mutants may reveal greater insight into the roles of residues that may be involved in the processes surrounding magnetoreception. Such mutants could include those that alter the ability to protonate the final tryptophan or flavin cofactor and those that compare the evolutionary role of certain point mutations that differ between migratory and non-migratory species.

Along a similar line is the comparison of additional species that link evolutionarily with those considered in this work. Such work is already underway with those mentioned in Chapter 4 who are developing expression protocols for cryptochrome 4 from zebra finches (*Taeniopygia guttata*) and blackcaps (*Sylvia atricapilla*), both of which sit along the same branch of the European robin. Measurements on such species could confirm that the findings in this work are indeed true of all migratory passeriformes.

While shown in this work to have no effect on the measurements reported here, initial measurements by fluorescence suggest that $K_3Fe(CN)_6$ may influence the *emission* properties of the proteins. It also appears to have some effects in the sample preparation protocols by promoting oligomerisation. It is therefore important to look closely at other potential oxidants that can perform the same function without causing any large-scale alterations to the proteins at any stage of the process of expressions and measurement.

Finally, further adjustments to the CRD spectrometer that were not possible within the timescale of this work could be made to make it even more effective. The use of a pulsed supercontinuum source alongside a spectrograph would allow for more data to be recorded – and that much more quickly. It would also provide the opportunity to better understand the various species that are involved in the photoprocesses explored above. Additionally, the use of a shorter cavity may make sense as this would allow measurement at pump-probe delay times shorter than 250 ns – much more relevant to the timescales on which it appears such magnetic field effects seem to take effect.

Of course the ultimate measurements would want to show these proteins as compass-like with a clear directional dependence. There is promising work being done with confocal microscopy, as evidenced by Déjean *et al.*, in which anisotropic magnetic field effects were evident in hen egg-white lysozyme crystals with FMN as a cofactor [68]. Should cryptochrome proteins be crystallised, such a technique would be invaluable to showing such magnetic anisotropy, further strengthening the ever-growing evidence for cryptochrome-based magnetoreception.

References

[1] H. Hagen. Beobachtung eines Pfeilstorches in Ost-Afrika. *Ornithol. Mitt.*, 27:111, 1975.

[2] C. Marti. Aristoteles und die Zugvögel – was er schrieb und was nicht. *Ornithol. Beobachter*, 113:309, 2016.

[3] R. Wiltschko and W. Wiltschko. *Magnetic Orientation in Animals*. Springer, Berlin, Heidelberg, 1st edition, 1995. ISBN 978-3-642-79749-1.

[4] R. Wiltschko, T. Ritz, K. Stapput, P. Thalau, and W. Wiltschko. Two different types of light-dependent responses to magnetic fields in birds. *Curr. Biol.*, 15:1518, 2005.

[5] S. Johnsen and K. J. Lohmann. The physics and neurobiology of magnetoreception. *Nat. Rev. Neurosci.*, 6:703, 2005.

[6] K. J. Lohmann, C. M. F. Lohmann, and N. F. Putman. Magnetic maps in animals: Nature's GPS. *J. Exp. Biol.*, 210:3697, 2007.

[7] H. Mouritsen. Navigation in birds and other animals. *Image Vis. Comput.*, 19:713, 2001.

[8] B. J. Frost and H. Mouritsen. The neural mechanisms of long distance animal navigation. *Curr. Opin. Neurobiol.*, 16:481, 2006.

[9] H. Mouritsen. Long-distance navigation and magnetoreception in migratory animals. *Nature*, 558:50, 2018.

[10] P. Berthold. A comprehensive theory for the evolution, control and adaptability of avian migration. *Ostrich*, 70:1, 1999.

[11] K. J. Lohmann, N. F. Putman, and C. M. F. Lohmann. The magnetic map of hatchling loggerhead sea turtles. *Curr. Opin. Neurobiol.*, 22:336, 2012.

[12] H. Mouritsen and O. Mouritsen. A mathematical expectation model for bird navigation based on the clock-and-compass strategy. *J. Theor. Biol.*, 207:283, 2000.

[13] A. J. Helbig. Genetic basis, mode of inheritance and evolutionary changes of migratory directions in palearctic warblers (Aves: Sylviidae). *J. Exp. Biol.*, 199:49, 1996.

[14] A. Gagliardo. Forty years of olfactory navigation in birds. *J. Exp. Biol.*, 216:2165, 2013.

[15] T. Guilford and D. Biro. Route following and the pigeon's familiar area map. *J. Exp. Biol.*, 217:169, 2014.

[16] R. C. Beason and J. E. Nichols. Magnetic orientation and magnetically sensitive material in a transequatorial migratory bird. *Nature*, 309:151, 1984.

[17] R. C. Beason, N. Dussourd, and M. E. Deutschlander. Behavioural evidence for the use of magnetic material in magnetoreception by a migratory bird. *J. Exp. Biol.*, 198:141, 1995.

[18] C. E. Diebel, R. Proksch, C. R. Green, P. Neilson, and M. M. Walker. Magnetite defines a vertebrate magnetoreceptor. *Nature*, 406:299, 2000.

[19] J. L. Kirschvink and J. L. Gould. Biogenic magnetite as a basis for magnetic field detection in animals. *BioSystems*, 13:181, 1981.

[20] U. Munro, J. A. Munro, J. B. Phillips, R. Wiltschko, and W. Wiltschko. Evidence for a magnetite-based navigational 'map' in birds. *Sci. Nat.*, 84:26, 1997.

[21] M. M. Walker, C. E. Diebel, C. V. Haugh, P. M. Pankhurst, J. C. Montgomery, and C. R. Green. Structure and function of the vertebrate magnetic sense. *Nature*, 390:371, 1997.

[22] G. Fleissner, E. Holtkamp-Rötzler, M. Hanzlik, M. Winklhofer, G. Fleissner, N. Petersen, and W. Wiltschko. Ultrastructural analysis of a putative magnetoreceptor in the beak of homing pigeons. *J. Comp. Neurol.*, 458:350, 2003.

[23] K. Schulten, C. E. Swenberg, and A. Weller. A Biomagnetic Sensory Mechanism Based on Magnetic Field Modulated Coherent Electron Spin Motion. *Z. Phys. Chem.*, 111:1, 1978.

[24] T. Ritz, S. Adem, and K. Schulten. A Model for Photoreceptor-Based Magnetoreception in Birds. *Biophys. J.*, 78:707, 2000.

[25] C. T. Rodgers and P. J. Hore. Chemical magnetoreception in birds: The radical pair mechanism. *Proc. Natl Acad. Sci. U.S.A.*, 106:353, 2009.

[26] R. Wiltschko and W. Wiltschko. Sensing magnetic directions in birds: radical pair processes involving cryptochrome. *Biosensors*, 4:221, 2014.

[27] P. J. Hore and H. Mouritsen. The Radical-pair Mechanism of Magnetoreception. *Annu. Rev. Biophys.*, 45:299, 2016.

[28] John B Phillips and S Chris Borland. Behavioural evidence for use of a light-dependent magnetoreception mechanism by a vertebrate. *Nature*, 359:142, 1992.

[29] W. Wiltschko and R. Wiltschko. Light-dependent magnetoreception in birds: The behaviour of European robins, *Erithacus rubecula*, under monochromatic light of various wavelengths and intensities. *J. Exp. Biol.*, 204:3295, 2001.

[30] R. Wiltschko, K. Stapput, P. Thalau, and W. Wiltschko. Directional orientation of birds by the magnetic field under different light conditions. *J. R. Soc. Interface*, 7:S163, 2010.

[31] M. Zapka, D. Heyers, C. M. Hein, S. Engels, N. L. Schneider, J. Hans, S. Weiler, D. Dreyer, D. Kishkinev, J. M. Wild, and H. Mouritsen. Visual but not trigeminal mediation of magnetic compass information in a migratory bird. *Nature*, 461:1274, 2009.

[32] T. Ritz, P. Thalau, J. B. Phillips, R. Wiltschko, and W. Wiltschko. Resonance effects indicate a radical-pair mechanism for avian magnetic compass. *Nature*, 429:177, 2004.

[33] K. B. Henbest, P. Kukura, C. T. Rodgers, P. J. Hore, and C. R. Timmel. Radio frequency magnetic field effects on a radical recombination reaction: a diagnostic test for the radical pair mechanism. *J. Am. Chem. Soc.*, 126:8102, 2004.

[34] P. Thalau, T. Ritz, K. Stapput, R. Wiltschko, and W. Wiltschko. Magnetic compass orientation of migratory birds in the presence of a 1.315 MHz oscillating field. *Sci. Nat.*, 92: 86, 2005.

[35] D. Nohr, S. Franz, R. Rodriguez, B. Paulus, L. O. Essen, S. Weber, and E. Schleicher. Extended Electron-Transfer in Animal Cryptochromes Mediated by a Tetrad of Aromatic Amino Acids. *Biophys. J.*, 111:301, 2016.

[36] K. Maeda, K. B. Henbest, F. Cintolesi, I. Kuprov, C. T. Rodgers, P. A. Liddell, D. Gust, C. R. Timmel, and P. J. Hore. Chemical compass model of avian magnetoreception. *Nature*, 453:387, 2008.

[37] C. Kerpal, S. Richert, J. G. Storey, S. Pillai, P. A. Liddell, D. Gust, S. R. Mackenzie, P. J. Hore, and C. R. Timmel. Chemical compass behaviour at microtesla magnetic fields strengthens the radical pair hypothesis of avian magnetoreception. *Nat. Commun.*, 10: 3707, 2019.

[38] G. E. Uhlenbeck and S. Goudsmit. Ersetzung der Hypothese vom unmechanischen Zwang durch eine Forderung bezüglich des inneren Verhaltens jedes einzelnen Elektrons. *Sci. Nat.*, 13:953, 1925.

[39] W. Gerlach and O. Stern. Der experimentelle Nachweis der Richtungsquantelung im Magnetfeld. *Z. Phys.*, 9:349, 1922.

[40] P. A. M. Dirac. The Quantum Theory of the Electron. *Proc. R. Soc. Lond. A*, 117:610, 1928.

[41] P. A. M. Dirac. The Quantum Theory of the Electron - Part II. *Proc. R. Soc. Lond. A*, 117: 351, 1928.

[42] P. W. Atkins, J. de Paula, and J. Keeler. *Physical Chemistry*. Oxford University Press, UK, 11th edition, 2017. ISBN 978-0-19876986-6.

[43] P. W. Atkins and R. S. Friedman. *Molecular Quantum Mechanics*. Oxford University Press, UK, 5th edition, 2010. ISBN 978-0-199-54142-3.

[44] N. J. B. Green. *Quantum Mechanics 1: Foundations*. Oxford University Press, UK, 1997. ISBN 978-0-198-55761-6.

[45] N. J. B. Green. *Quantum Mechanics 2: The Toolkit*. Oxford University Press, UK, 1998. ISBN 978-0-198-50227-2.

[46] G. L. Closs. A Mechanism Explaining Nuclear Spin Polarizations in Radical Combination Reactions. *J. Am. Chem. Soc.*, 91:4552, 1969.

[47] R. Kaptein and J. L. Oosterhoff. Chemically Induced Dynamic Nuclear Polarization II. *Chem. Phys. Lett.*, 4:195, 1969.

[48] K. Schulten and I. R. Epstein. Recombination of radical pairs in high magnetic fields: a path integral-Monte Carlo treatment. *J. Chem. Phys.*, 71:309, 1979.

[49] U. E. Steiner and T. Ulrich. *Magnetic Field Effects in Chemical Kinetics and Related Phenomena*, volume 89. 1989.

[50] K. A. McLauchlan and U. E. Steiner. The spin-correlated radical pair as a reaction intermediate. *Mol. Phys.*, 73:241, 1991.

[51] P. A. M. Dirac. Quantum mechanics of many-electron systems. *Proc. R. Soc. Lond. A*, 123:714, 1929.

[52] C. T. Rodgers. Magnetic field effects in chemical systems. *Pure Appl. Chem.*, 81:19, 2009.

[53] F. J. J. De Kanter, J. A. Den Hollander, A. H. Huizer, and R. Kaptein. Biradical CIDNP and the dynamics of polymethylene chains. *Mol. Phys.*, 34:857, 1977.

[54] H. M. McConnell. Indirect Hyperfine Interactions in the Paramagnetic Resonance Spectra of Aromatic Free Radicals. *J. Chem. Phys.*, 24:764, 1956.

[55] R. C. Johnson, R. E. Merrifield, P. Avakian, and R. B. Flippen. Effects of magnetic fields on the mutual annihilation of triplet excitons in molecular crystals. *Phys. Rev. Lett.*, 19: 285, 1967.

[56] R. E. Merrifield. Theory of magnetic field effects on the mutual annihilation of triplet excitons. *J. Chem. Phys.*, 48:4318, 1968.

[57] A. M. Lewis, T. P. Fay, D. E. Manolopoulos, C. Kerpal, S. Richert, and C. R. Timmel. On the low magnetic field effect in radical pair reactions. *J. Chem. Phys.*, 149:34103, 2018.

[58] B. Brocklehurst and K. A. McLauchlan. Free radical mechanism for the effects of environmental electromagnetic fields on biological systems. *Int. J. Radiat. Biol.*, 69:3, 1996.

[59] A. Weller, F. Nolting, and H. Staerk. A quantitative interpretation of the magnetic field effect on hyperfine-coupling-induced triplet formation from radical ion pairs. *Chem. Phys. Lett.*, 96:24, 1983.

[60] K. Maeda, A. J. Robinson, K. B. Henbest, H. J. Hogben, T. Biskup, M. Ahmad, E. Schleicher, S. Weber, C. R. Timmel, and P. J. Hore. Magnetically sensitive light-induced reactions in cryptochrome are consistent with its proposed role as a magnetoreceptor. *Proc. Natl Acad. Sci. U.S.A.*, 109:4774, 2012.

[61] K. Maeda, T. Miura, and T. Arai. A practical simulation and a novel insight to the magnetic field effect on a radical pair in a micelle. *Mol. Phys.*, 104:1779, 2006.

[62] R. C. Johnson and R. E. Merrifield. Effects of Magnetic Fields on the Mutual Annihilation of Triplet Excitons in Anthrcene Crystals. *Phys. Rev. B*, 1:896, 1970.

[63] L. Yarmus, J. Rosenthal, and M. Chopp. EPR of triplet excitions in tetracene crystals: spin polarization and the role of singlet exciton fission. *Chem. Phys. Lett.*, 16:477, 1972.

[64] H. Sternlicht and H. M. McConnell. Paramagnetic Excitons in Molecular Crystals. *J. Chem. Phys.*, 35:1793, 1961.

[65] R. B. Frankel and R. P. Blakemore. Magnetite and magnetotaxis in microorganisms. *Bioelectromagnetics*, 10:223, 1989.

[66] R. A. Holland. Differential effects of magnetic pulses on the orientation of naturally migrating birds. *J. R. Soc. Interface*, 7:1617, 2010.

[67] R. Wiltschko and W. Wiltschko. Pigeon homing: Effect of various wavelengths of light during displacement. *Sci. Nat.*, 85:164, 1998.

[68] V. Déjean, M. Konowalczyk, J. Gravell, M. J. Golesworthy, C. Gunn, N. Pompe, O. Foster Vander Elst, K. J. Tan, M. Oxborrow, D. G. A. L. Aarts, S. R. Mackenzie, and C. R. Timmel. Detection of magnetic field effects by confocal microscopy. *Chem. Sci.*, 11:7772, 2020.

[69] W. Wiltschko and R. Wiltschko. Magnetic compass of European robins. *Science*, 176:62, 1972.

[70] J. L. Kirschvink, M. M. Walker, and C. E. Diebel. Magnetite-based magnetoreception. *Curr. Opin. Neurobiol.*, 11:462, 2001.

[71] I. A. Solov'yov and W. Greiner. Theoretical analysis of an iron mineral-based magnetoreceptor model in birds. *Biophys. J.*, 93:1493, 2007.

[72] M. M. Walker, T. E. Dennis, and J. L. Kirschvink. The magnetic sense and its use in long-distance navigation by animals. *Curr. Opin. Neurobiol.*, 12:735, 2002.

[73] M. Winklhofer and J. L. Kirschvink. A quantitative assessment of torque-transducer models for magnetoreception. *J. R. Soc. Interface*, 7:S273, 2010.

[74] D. A. Bazylinski and R. B. Frankel. Magnetosome formation in prokaryotes. *Nat. Rev. Microbiol.*, 2:217, 2004.

[75] R. Blakemore. Magnetotactic bacteria. *Science*, 190:377, 1975.

[76] H. Mouritsen. *The Magnetic Senses (from "Neurosciences - From Molecule to Behaviour: A University Textbook").* Springer Spektrum, Berlin, Heidelberg, 1st edition, 2013. ISBN 978-3-642-10769-6.

[77] G. Falkenberg, G. Fleissner, K. Schuchardt, M. Kuehbacher, P. Thalau, H. Mouritsen, D. Heyers, G. Wellenreuther, and G. Fleissner. Avian magnetoreception: Elaborate iron mineral containing dendrites in the upper beak seem to be a common feature of birds. *PLoS ONE*, 5:e9231, 2010.

[78] C. D. Treiber, M. Salzer, M. Breuss, L. Ushakova, M. Lauwers, N. Edelman, and D. A. Keays. High resolution anatomical mapping confirms the absence of a magnetic sense system in the rostral upper beak of pigeons. *Commun. Integr. Biol.*, 6:4, 2013.

[79] C. D. Treiber, M. C. Salzer, J. Riegler, N. Edelman, C. Sugar, M. Breuss, P. Pichler, H. Cadiou, M. Saunders, M. Lythgoe, J. Shaw, and D. A. Keays. Clusters of iron-rich cells in the upper beak of pigeons are macrophages not magnetosensitive neurons. *Nature*, 484: 367, 2012.

[80] C. V. Mora, M. Davison, J. Martin Wild, and M. M. Walker. Magnetoreception and its trigeminal mediation in the homing pigeon. *Nature*, 432:508, 2004.

[81] D. Heyers, M. Zapka, M. Hoffmeister, J. M. Wild, and H. Mouritsen. Magnetic field changes activate the trigeminal brainstem complex in a migratory bird. *Proc. Natl Acad. Sci. U.S.A.*, 107:9394, 2010.

[82] N. Lefeldt, D. Heyers, N. L. Schneider, S. Engels, D. Elbers, and H. Mouritsen. Magnetic field-driven induction of ZENK in the trigeminal system of pigeons (*Columba livia*). *J. R. Soc. Interface*, 11:20140777, 2014.

[83] R. A. Holland. True navigation in birds: from quantum physics to global migration. *J. Zool.*, 293:1, 2014.

[84] C. X. Wang, I. A. Hilburn, D. A. Wu, Y. Mizuhara, C. P. Cousté, J. N. H. Abrahams, S. E. Bernstein, A. Matani, S. Shimojo, and J. L. Kirschvink. Transduction of the Geomagnetic Field as Evidenced from alpha-Band Activity in the Human Brain. *eNeuro*, 6: ENEURO.0483–18.2019, 2019.

[85] N. Özturk. Phylogenetic and Functional Classification of the Photolyase/Cryptochrome Family. *Photochem. Photobiol.*, 93:104, 2017.

[86] N. Öztürk, S. H. Song, S. Özgür, C. P. Selby, L. Morrison, C. Partch, D. Zhong, and A. Sancar. Structure and function of animal cryptochromes. *Cold Spring Harbor Symp. Quant. Biol.*, 72:119, 2007.

[87] I. Chaves, R. Pokorny, M. Byrdin, N. Hoang, T. Ritz, K. Brettel, L. O. Essen, G. T. J. Van Der Horst, A. Batschauer, and M. Ahmad. The cryptochromes: Blue light photoreceptors in plants and animals. *Annu. Rev. Plant Biol.*, 62:335, 2011.

[88] M. Liedvogel and H. Mouritsen. Cryptochromes - A potential magnetoreceptor: What do we know and what do we want to know? *J. R. Soc. Interface*, 7:S147, 2010.

[89] A. Sancar. Cryptochrome: The second photoactive pigment in the eye and its role in circadian photoreception. *Annu. Rev. Biochem.*, 69:31, 2000.

[90] C. L. Partch and A. Sancar. Photochemistry and Photobiology of Cryptochrome Blue-light Photopigments: The Search for a Photocycle. *Photochem. Photobiol.*, 81:1291, 2005.

[91] C. L. Partch, M. W. Clarkson, S. Özgür, A. L. Lee, and A. Sancar. Role of structural plasticity in signal transduction by the cryptochrome blue-light photoreceptor. *Biochemistry*, 44:3795, 2005.

[92] T. Kottke, A. Batschauer, M. Ahmad, and J. Heberle. Blue-light-induced changes in *arabidopsis* cryptochrome 1 probed by FTIR difference spectroscopy. *Biochemistry*, 45: 2472, 2006.

[93] C. Lin and D. Shalitin. Cryptochrome Structure and Signal Transduction. *Annu. Rev. Plant Biol.*, 54:469, 2003.

[94] S. Franz, E. Ignatz, S. Wenzel, H. Zielosko, E. P. G. Ngurah Putu, M. Maestre-Reyna, M. D. Tsai, J. Yamamoto, M. Mittag, and L. O. Essen. Structure of the bifunctional cryptochrome aCRY from *Chlamydomonas reinhardtii*. *Nucleic Acids Res.*, 46:8010, 2018.

[95] R. Brudler, K. Hitomi, H. Daiyasu, H. Toh, K. I. Kucho, M. Ishiura, M. Kanehisa, V. A. Roberts, T. Todo, J. A. Tainer, and E. D. Getzoff. Identification of a new cryptochrome class: Structure, function, and evolution. *Mol. Cell*, 11:59, 2003.

[96] K. Hitomi, K. Okamoto, H. Daiyasu, H. Miyashita, S. Iwai, H. Toh, M. Ishiura, and T. Todo. Bacterial cryptochrome and photolyase: Characterization of two photolyase-like genes of *Synechocystis* sp. PCC6803. *Nucleic Acids Res.*, 28:2353, 2000.

[97] N. Öztürk, Y. T. Kao, C. P. Selby, I. H. K., C. L. Partch, D. Zhong, and A. Sancar. Purification and characterization of a type III photolyase from *Caulobacter crescentus*. *Biochemistry*, 47:10255, 2008.

[98] C. Levy, B. D. Zoltowski, A. R. Jones, A. T. Vaidya, D. Top, J. Widom, M. W. Young, N. S. Scrutton, B. R. Crane, and D. Leys. Updated structure of Drosophila cryptochrome. *Nature*, 495:7441, 2013.

[99] A. Günther, A. Einwich, E. Sjulstok, R. Feederle, P. Bolte, K. W. Koch, I. A. Solov'yov, and H. Mouritsen. Double-Cone Localization and Seasonal Expression Pattern Suggest a Role in Magnetoreception for European Robin Cryptochrome 4. *Curr. Biol.*, 28:211, 2018.

[100] J. Xu, L. E. Jarocha, T. Zollitsch, M. Konowalczyk, K. B. Henbest, S. Richert, M. J. Golesworthy, J. Schmidt, V. Déjean, D. J. C. Sowood, M. Bassetto, J. Luo, J. R. Walton, J. Fleming, Y. Wei, T. L. Pitcher, G. Moise, M. Herrmann, H. Yin, H. Wu, R. Bartölke, S. J. Käsehagen, S. Horst, G. Dautaj, P. D. F. Murton, A. S. Gehrckens, Y. Chelliah, J. S. Takahashi, K.-W. Koch, S. Weber, I. A. Solov'yov, C. Xie, S. R. Mackenzie, C. R. Timmel, H. Mouritsen, and P. J. Hore. Magnetic sensitivity of cryptochrome 4 from a migratory songbird. *Nature*, 594:535, 2021.

[101] B. Giovani, M. Byrdin, M. Ahmad, and K. Brettel. Light-induced electron transfer in a cryptochrome blue-light photoreceptor. *Nat. Struct. Biol.*, 10:489, 2003.

[102] C. Aubert, M. H. Vos, P. Mathis, A. P. M. Eker, and K. Brettel. Intraprotein radical transfer during photoactivation of DNA photolyase. *Nature*, 405:586, 2000.

[103] T. Biskup, E. Schleicher, A. Okafuji, G. Link, K. Hitomi, E. D. Getzoff, and S. Weber. Direct Observation of a Photoinduced Radical-Pair Intermediate in a Cryptochrome DASH Blue-Light Photoreceptor. *Angew. Chem. Int. Ed.*, 48:404, 2009.

[104] P. Müller, J. Yamamoto, R. Martin, S. Iwai, and K. Brettel. Discovery and functional analysis of a 4th electron-transferring tryptophan conserved exclusively in animal cryptochromes and (6-4) photolyases. *Chem. Commun.*, 51:15502, 2015.

[105] D. Nohr, B. Paulus, R. Rodriguez, A. Okafuji, R. Bittl, E. Schleicher, and S. Weber. Determination of Radical–Radical Distances in Light-Active Proteins and Their Implication for Biological Magnetoreception. *Angew. Chem. Int. Ed.*, 56:8550, 2017.

[106] F. Cailliez, P. Müller, T. Firmino, P. Pernot, and A. De La Lande. Energetics of Photoinduced Charge Migration within the Tryptophan Tetrad of an Animal (6-4) Photolyase. *J. Am. Chem. Soc.*, 138:1904, 2016.

[107] B. D. Zoltowski, Y. Chelliah, A. Wickramaratne, L. Jarocha, N. Karki, W. Xu, H. Mouritsen, P. J. Hore, R. E. Hibbs, C. B. Green, and J. S. Takahashi. Chemical and structural analysis of a photoactive vertebrate cryptochrome from pigeon. *Proc. Natl Acad. Sci. U.S.A.*, 116:19449, 2019.

[108] T. M. Zollitsch. *Investigation of Magnetic Field Effects on Protein Photochemistry using Cavity Enhanced Spectroscopy*. PhD thesis, University of Oxford, 2018.

[109] R. Watari, C. Yamaguchi, W. Zemba, Y. Kubo, K. Okano, and T. Okano. Light-dependent structural change of chicken retinal cryptochrome4. *J. Biol. Chem.*, 287:42634, 2012.

[110] N. Özturk, C. P. Selby, Y. Annayev, D. Zhong, and A. Sancar. Reaction mechanism of *Drosophila* cryptochrome. *Proc. Natl Acad. Sci. U.S.A.*, 108:516, 2011.

[111] N. Peschel, K. F. Chen, G. Szabo, and R. Stanewsky. Light-Dependent Interactions between the *Drosophila* Circadian Clock Factors Cryptochrome, Jetlag, and Timeless. *Curr. Biol.*, 19:241, 2009.

[112] S. Dissel, V. Codd, R. Fedic, K. J. Garner, R. Costa, C. P. Kyriacou, and E. Rosato. A constitutively active cryptochrome in *Drosophila melanogaster*. *Nat. Neur.*, 7:834, 2004.

[113] E. Rosato, V. Codd, A. Mazzotta, G.and Piccin, M. Zordan, R. Costa, and C. P. Kyriacou. Light-dependent interaction between *Drosophila* CRY and the clock protein PER mediated by the carboxy terminus of CRY. *Curr. Biol.*, 11:909, 2001.

[114] A. T. Vaidya, D. Top, C. C. Manahan, J. M. Tokuda, S. Zhang, L. Pollack, M. W. Young, and B. R. Crane. Flavin reduction activates *Drosophila* cryptochrome. *Proc. Natl Acad. Sci. U.S.A.*, 110:20455, 2013.

[115] J. H. Lambert. *Photometria sive de mensura et gradibus luminis, colorum et umbrae*. Detleffson, C. P., Augsburg, 1st edition, 1760.

[116] P. Bouguer. *Essai d'Optique, sur la Gradation de la Lumiere*. Claude Jombert, Paris, 1st edition, 1729.

[117] A. Beer. Bestimmung der Absorption des rothen Lichts in farbigen Flüssigkeiten. *Ann. Phys.*, 86:78, 1852.

[118] J. U. White. Long Optical Paths of Large Aperture. *J. Opt. Soc. Am.*, 32:285, 1942.

[119] J. U. White. Very Long Optical Paths in Air. *J. Opt. Soc. Am.*, 66:411, 1976.

[120] D. R. Herriott and H. J. Schulte. Folded Optical Delay Lines. *Appl. Opt.*, 4:883, 1965.

[121] A. E. Siegman. Lasers, 1986.

[122] A. Yariv. *Quantum Electronics*. Wiley, 3rd edition, 1989. ISBN 978-0-471-60997-1.

[123] K. Maeda, S. R. T. Neil, K. B. Henbest, S. Weber, E. Schleicher, P. J. Hore, S. R. MacKenzie, and C. R. Timmel. Following radical pair reactions in solution: A step change in sensitivity using cavity ring-down detection. *J. Am. Chem. Soc.*, 133:17807, 2011.

[124] M. Sugahara, T. Nakane, T. Masuda, M. Suzuki, S. Inoue, C. Song, R. Tanaka, T. Nakatsu, E. Mizohata, F. Yumoto, K. Tono, Y. Joti, T. Kameshima, T. Hatsui, M. Yabashi, O. Nureki, K. Numata, E. Nango, and S. Iwata. Hydroxyethyl cellulose matrix applied to serial crystallography. *Sci. Rep.*, 7:703, 2017.

[125] K. Maeda, A. J. Robinson, K. B. Henbest, E. J. Dell, and C. R. Timmel. Protein surface interactions probed by magnetic field effects on chemical reactions. *J. Am. Chem. Soc.*, 132:1466, 2010.

[126] M. Sakai and H. Takahashi. One-electron photoreduction of flavin mononucleotide: Time-resolved resonance Raman and absorption study. *J. Mol. Struct.*, 379:9, 1996.

[127] D. M. W. Sheppard. *Cavity-enhanced Detection of Biologically Relevant Magnetic Field Effects.* PhD thesis, University of Oxford, 2016.

[128] R. J. Stanley and H. Jang. Electronic structure measurements of oxidized flavins and flavin complexes using Stark-effect spectroscopy. *J. Phys. Chem. A*, 103:8976, 1999.

[129] E. Evans. *Making Physics Work for Biology: Using Spin Chemistry to Understand Protein Mechanism and Structure.* PhD thesis, University of Oxford, 2016.

[130] F. Müller, M. Brüstlein, P. Hemmerich, V. Massey, and W. H. Walker. Light-Absorption Studies on Neutral Flavin Radicals. *Eur. J. Biochem.*, 25:573, 1972.

[131] T. Miura, K. Maeda, and T. Arai. Effect of Coulomb interaction on the dynamics of the radical pair in the system of flavin mononucleotide and hen egg-white lysozyme (HEWL) studied by a magnetic field effect. *J. Phys. Chem. B*, 107:6474, 2003.

[132] D. Ityaksov. *Cavity Ring-down Optical Extinction Measurements of Atmospheric Molecules.* PhD thesis, Vrije Universiteit Amsterdam, 2009.

[133] D. M. W. Sheppard, J. Li, K. B. Henbest, S. R.T. Neil, K. Maeda, J. Storey, E. Schleicher, T. Biskup, R. Rodriguez, S. Weber, P. J. Hore, C. R. Timmel, and S. R. MacKenzie. Millitesla magnetic field effects on the photocycle of an animal cryptochrome. *Sci. Rep.*, 7:42228, 2017.

[134] A. Sancar. Structure and Function of DNA Photolyase and Cryptochrome Blue-Light Photoreceptors. *Chem. Rev.*, 103:2203, 2003.

[135] E. D. Jarvis, S. Mirarab, A. J. Aberer, B. Li, P. Houde, C. Li, S. Y. Ho, B. C. Faircloth, B. Nabholz, J. T. Howard, A. Suh, C. C. Weber, R. R. da Fonseca, J. Li, F. Zhang, H. Li, L. Zhou, N. Narula, L. Liu, G. Ganapathy, B. Boussau, M. S. Bayzid, V. Zavidovych, S. Subramanian, T. Gabaldòn, S. Capella-Gutièrrez, J. Huerta-Cepas, B. Rekepalli, K. Munch, M. Schierup, B. Lindow, W. C. Warren, D. Ray, R. E. Green, M. W. Bruford, X. Zhan, A. Dixon, S. Li, N. Li, Y. Huang, E. P. Derryberry, M. F. Bertelsen, F. H. Sheldon, R. T. Brumfield, C. V. Mello, P. V. Lovell, M. Wirthlin, M. P. Schneider, F. Prosdocimi, J. A. Samaniego, A. M. Vargas Velazquez, A. Alfaro-Núñez, P. F. Campos, B. Petersen, T. Sicheritz-Ponten, A. Pas, T. Bailey, P. Scofield, M. Bunce, D. M. Lambert, Q. Zhou, P. Perelman, A. C. Driskell, B. Shapiro, Z. Xiong, Y. Zeng, S. Liu, Z. Li, B. Liu, K. Wu, J. Xiao, X. Yinqi, Q. Zheng, Y. Zhang, H. Yang, J. Wang, L. Smeds, F. E. Rheindt, M. Braun,

J. Fjeldsa,. Whole-genome analyses resolve early branches in the tree of life of modern birds. *Science*, 346:1320, 2014.

[136] C. Nießner, S. Denzau, K. Stapput, M. Ahmad, L. Peichl, W. Wiltschko, and R. Wiltschko. Magnetoreception: Activated cryptochrome 1a concurs with magnetic orientation in birds. *J. R. Soc. Interface*, 10:20130638, 2013.

[137] T. Hochstoeger, T. A. Said, D. Maestre, F.n Walter, A. Vilceanu, M. Pedron, T. D. Cushion, W. Snider, S. Nimpf, G. C. Nordmann, L. Landler, N. Edelman, L. Kruppa, G. Dürnberger, K. Mechtler, S. Schuechner, E. Ogris, E. P. Malkemper, S. Weber, E. Schleicher, and D. A. Keays. The biophysical, molecular, and anatomical landscape of pigeon CRY4: A candidate light-based quantal magnetosensor. *Sci. Adv.*, 6:eabb9110, 2020.

[138] F. Madeira, Y. M. Park, J. Lee, N. Buso, T. Gur, N. Madhusoodanan, P. Basutkar, A. R. N. Tivey, S. C. Potter, R. D. Finn, and R. Lopez. The EMBL-EBI search and sequence analysis tools APIs in 2019. *Nucleic Acids Res.*, 47:W636, 2019.

[139] S. Qin, H. Yin, C. Yang, Y. Dou, Z. Liu, P. Zhang, H. Yu, Y. Huang, J. Feng, J. Hao, J. Hao, L. Deng, X. Yan, X. Dong, Z. Zhao, T. Jiang, H. W. Wang, S. J. Luo, and C. Xie. A magnetic protein biocompass. *Nat. Mater.*, 15:217, 2016.

[140] B. Liu, H. Liu, D. Zhong, and C. Lin. Searching for a photocycle of the cryptochrome photoreceptors. *Curr. Opin. Plant Biol.*, 13:578, 2010.

[141] S. Solar, N. Getoff, P. S. Surdhar, D. A. Armstrong, and A. Singh. Oxidation of tryptophan and N-methylindole by N3•, Br2•-, and (SCN)2•- radicals in light- and heavy-water solutions: A pulse radiolysis study. *J. Phys. Chem.*, 95:3639, 1991.

[142] J. E. Miller, C. Grădinaru, B. R. Crane, A. J. Di Bilio, W. A. Wehbi, S. Un, J. R. Winkler, and H. B. Gray. Spectroscopy and Reactivity of a Photogenerated Tryptophan Radical in a Structurally Defined Protein Environment. *J. Am. Chem. Soc.*, 125:14220, 2003.

[143] D. Selby. *Simulation of Time-dependent Magnetic Field Effects on Radical Pair Reactions in Cryptochromes.* Master's thesis, University of Oxford, 2021.

[144] C. R. Timmel, U. Till, B. Brocklehurst, K. A. McLauchlan, and P. J. Hore. Effects of weak magnetic fields on free radical recombination reactions. *Mol. Phys.*, 95:71, 1998.

[145] R. B. Reeves. The Interaction of Body Temperature and Acid-Base Balance in Ectothermic Vertebrates. *Annu. Rev. Physiol.*, 39:559, 1977.

[146] A. Roos and W. F. Boron. Intracellular pH. *Physiol. Rev.*, 61:296, 1981.

[147] J. Ojeda, C. A. Arrell, L. Longetti, M. Chergui, and J. Helbing. Charge-transfer and impulsive electronic-to-vibrational energy conversion in ferricyanide: Ultrafast photoelectron and transient infrared studies. *Phys. Chem. Chem. Phys.*, 19:17052, 2017.

[148] W. Zhang, M. Ji, Z. Sun, and K. J. Gaffney. Dynamics of solvent-mediated electron localization in electronically excited hexacyanoferrate(III). *J. Am. Chem. Soc.*, 134:2581, 2012.

[149] N. Engel, S. I. Bokarev, A. Moguilevski, A. A. Raheem, R. Al-Obaidi, T. Möhle, G. Grell, K. R. Siefermann, B. Abel, S. G. Aziz, O. Kühn, M. Borgwardt, I. Y. Kiyan, and E. F. Aziz. Light-induced relaxation dynamics of the ferricyanide ion revisited by ultrafast XUV photoelectron spectroscopy. *Phys. Chem. Chem. Phys.*, 19:14248, 2017.

[150] M. Reinhard, G. Auböck, N. A. Besley, I. P. Clark, G. M. Greetham, M. W. D. Hanson-Heine, R. Horvath, T. S. Murphy, T. J. Penfold, M. Towrie, M. W. George, and M. Chergui. Photoaquation Mechanism of Hexacyanoferrate(II) Ions: Ultrafast 2D UV and Transient Visible and IR Spectroscopies. *J. Am. Chem. Soc.*, 139:7335, 2017.

[151] H. Wu, A. Scholten, A. Einwich, H. Mouritsen, and K. W. Koch. Protein-protein interaction of the putative magnetoreceptor cryptochrome 4 expressed in the avian retina. *Sci. Rep.*, 10:7364, 2020.

[152] O. Efimova and P. J. Hore. Role of exchange and dipolar interactions in the radical pair model of the avian magnetic compass. *Biophys. J.*, 94:1565, 2008.